Pattern-less Electromagnetic Wave Manipulation by Active Control of Tunable Metamaterials

Feng-Ju Hsieh

A dissertation

submitted in partial fulfillment of the

requirements for the degree of

Doctor of Philosophy

University of Washington

2012

Reading Committee:

Wei-Chih Wang, Chair

Albert S Kobayashi

Blake Hannaford

Joseph Garbini

Martin Afromowitz

Program Authorized to Offer Degree:

Mechanical Engineering

ABSTRACT

Terahertz technologies have been attracting attention over the past few years due to their unique applications in bio-chemical sensing, bio-imaging, spectroscopy, security, and communications. Traditionally, the systems used in these applications steer electromagnetic (EM) waves in free space, resulting in bulky systems with a maximum spatial resolution defined by the Abbe diffraction limit. This paper studies active and tunable devices for EM wave steering and confinement with subwavelength beam sizes as a means to minimize the system size and increase the spatial resolution beyond the Abbe limit. These devices are employed in two major applications, a multifunctional waveguide and a gradient flat lens. However, finalizing the design requires that the constitutive parameters and material properties of metamaterials (MMs) be determined and characterized.

First, investigations were conducted to retrieve the material constitutive parameters of the proposed active metamaterials, such as effective permittivity and permeability. Classical methods for determining these properties are not robust; in this study, improved methods for single-layered and multi-layered MMs are proposed to fully retrieve effective material properties and constitutive parameters of the MMs at all frequencies of the interest, including the values in the resonant band.

Second, new kinds of active tunable MM structures were invented, based on a passive gradient dielectric substrate and partially disconnected electrodes. This creates a system capable of actively reconfiguring a beam profile by tuning the material properties of individual unit cells as desired. This active gradient MMs technology has great potential in several fields, such as optical communications, quantum computing, and as an in-situ reconfigurable mask for photolithography.

Finally, a novel subwavelength waveguide and a multifunctional flat lens based on the proposed active tunable MMs are investigated. This novel active waveguide design would lead to vastly superior wave couplers, splitters, and phase compensators, able to alter beam profiles, steer beams, act as optical multiplexers, switches, tunable filters and selectable polarizers, etc. The proposed methods and invented active tunable MMs can be adopted in systems operating at different frequencies, from microwaves to optics.

ACKNOWLEDGEMENTS

I would like to recognize my advisor, Professor Wei-Chih Wang, and express my deepest gratitude and respect to him for his mentoring in my Ph.D. program. Few students have the opportunity to explore so many different and interesting research projects and areas, including robotics controls, Fourier Transform spectrometry, optical coherence tomography, the optical fiber glove sensor, optical waveguide design, and electromagnetics. I am so glad to be able to build and expand my scope of knowledge from all of those involvements in the lab. He also offered me the great experience to be an instructor of ENGR100 class for years during my studies in the school so that I could sharpen my teaching skill and be inspired to create interesting projects for my students.

I would also like to give my sincere appreciation to the committee members, for their time and precious advice in this research. I gratefully acknowledge my previous advisor, Professor Jacob Rosen, and the Director of the BioRobotics Lab, Professor Blake Hannaford, for enriching my knowledge in biomechanics and surgical robotic control.

Even though some of my friends and labmates are humble and would prefer that I not remark how significant they are to me, I would still like to acknowledge and thank them for all the discussions, inspirations, and delightful times we shared.

Finally, this thesis is dedicated to my parents and family for their unconditional love, understanding and encouragement. Without their support, there is no way I could achieve this important milestone in my life.

TABLE OF CONTENTS

LIST OF FIGURES

LIST OF TABLES

Chapter 1. INTRODUCTION OF METAMATERIALS

Until recently, the lack of naturally existing materials responding to the incident waves at Terahertz frequencies created an unexplored band of the electromagnetic spectrum, called the "THz Gap" [1]. Over the past two decades, Terahertz technology has garnered increasing attention due to its unique applications [2-12] relating to bio-chemical sensing [6, 8], spectroscopy [5, 7, 8, 10-12], bio-imaging [3, 6, 9, 13, 14], security detection [2], and communications [15]. These applications rely on several different THz technologies, such as THz sources, detectors, beam splitters, polarizers, and lenses [5, 16-18]. Traditionally, those applications are implemented by steering electromagnetic (EM) waves in free space, resulting in bulky and diffraction-limited systems [5]. Another inherent constraint in free space propagation is the Abbe diffraction limit, corresponding to the travelling wave in the medium and numerical aperture of a system, is roughly half of the wavelength, and defines the maximum spatial resolution of the system. In order to create compact THz systems, devices that can confine and steer EM waves at dimensions much smaller than one wavelength are necessary. Thanks to the development of metamaterials (MMs) [19-21], the requirements for these exotic phenomena can be fulfilled in THz band.

The prefix "meta-" implies "beyond", and the terminology "metamaterial" hints that the artificially engineered material, typically synthesized by periodic arrays of noble metallic patterns inside or on a dielectric or semi-conducting substrate, possesses the exotic phenomena beyond all the naturally existing materials [22], such as in single negative (SNG) or double negative (DNG) permittivity (ε) and permeability (μ) in a certain frequency range, as shown in Figure 1.1. Most natural dielectric materials possessing double positive (DPS) permittivity and permeability fall in the first quadrant in Figure 1.1. Noble metals such as silver and gold behaving as plasmas in the infrared and optical frequency band can be classified in the second quadrant and have negative ε (ENG). For gyrotropic materials such as ferrites and some artificial material such as split ring resonators (SRR) at certain frequencies can be classified into the fourth quadrant and

have negative μ (MNG). It is worth mentioning that the waves can only propagate in the medium classified in the first and third quadrant.

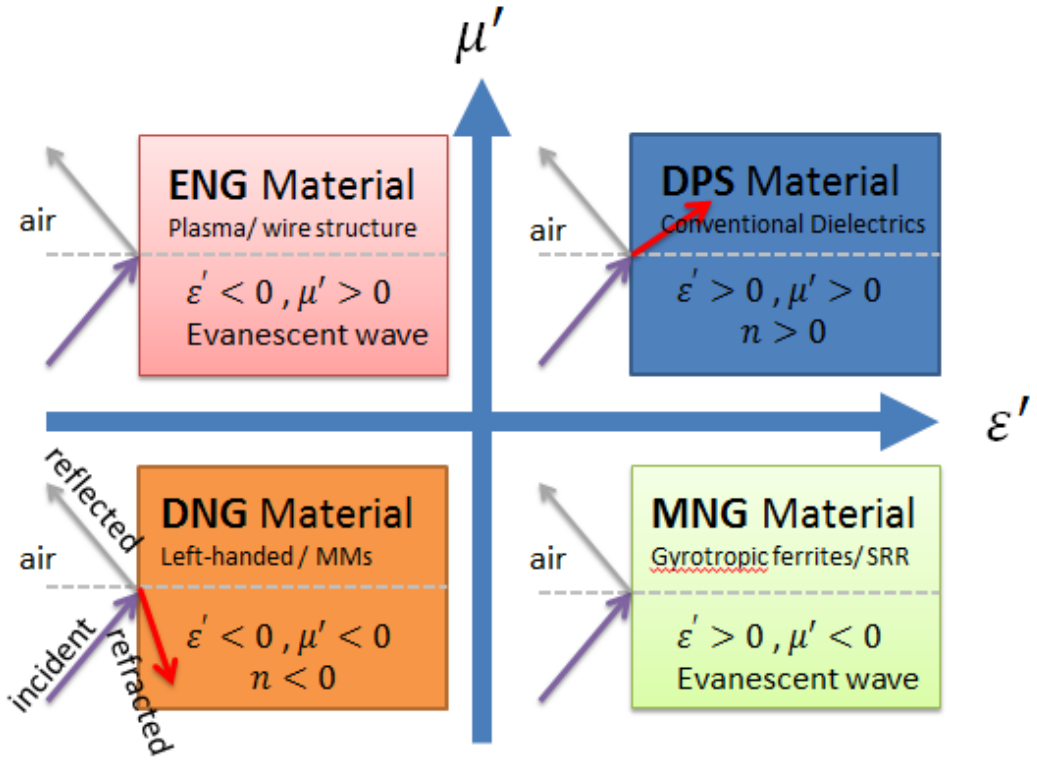

Figure 1.1. Materials classified by the real parts of the permittivity and the permeability.

1.1 History of Metamaterials

Throughout human history, scientists and craftsmen worked to engineer and create complex materials for specific purposes. However, the possibility of a material to simultaneously possess negative permittivity and permeability was not until realized until Veselago published a theoretical study in 1967 on what he termed 'left-handed material' (LHM) [21]. His work theoretically showed that the Poynting vector of a plane wave travelling in such a material is antiparallel to the direction of the phase velocity. Such a

material has yet to be found in any naturally occurring medium, though Veselago speculated the existence of gyrotropic substances possessing both plasma and magnetic properties.

In 1996, Pendry [23] theoretically proposed (then demonstrated in 1998) that periodical arrays of thin metallic wires with periodicity much less than the incident wavelength can behave like a plasma medium, as shown in Figure 1.2 (a). Therefore, negative permittivity exists at certain frequencies lower than its corresponding electric plasma frequency.

In 1999, Pendry [24] first theoretically introduced and considered loops, helices, spirals, omega-shaped, and split ring structures (shown in Figure 1.2 (b)), as magnetically resonant patterns leading to negative magnetic permeability. He also indicated that the effective magnetic permeability can be described by Lorentz dispersion models.

Based on Pendry's discoveries, the first experiment demonstrating a negative refractive index was conducted by D.R. Smith in 2000, using a prism composed of thin wires and SRRs in microwave frequency band[20]. Since then, interest in the field has grown, pushing metamaterials to work in frequency bands ranging from acoustics to optics.

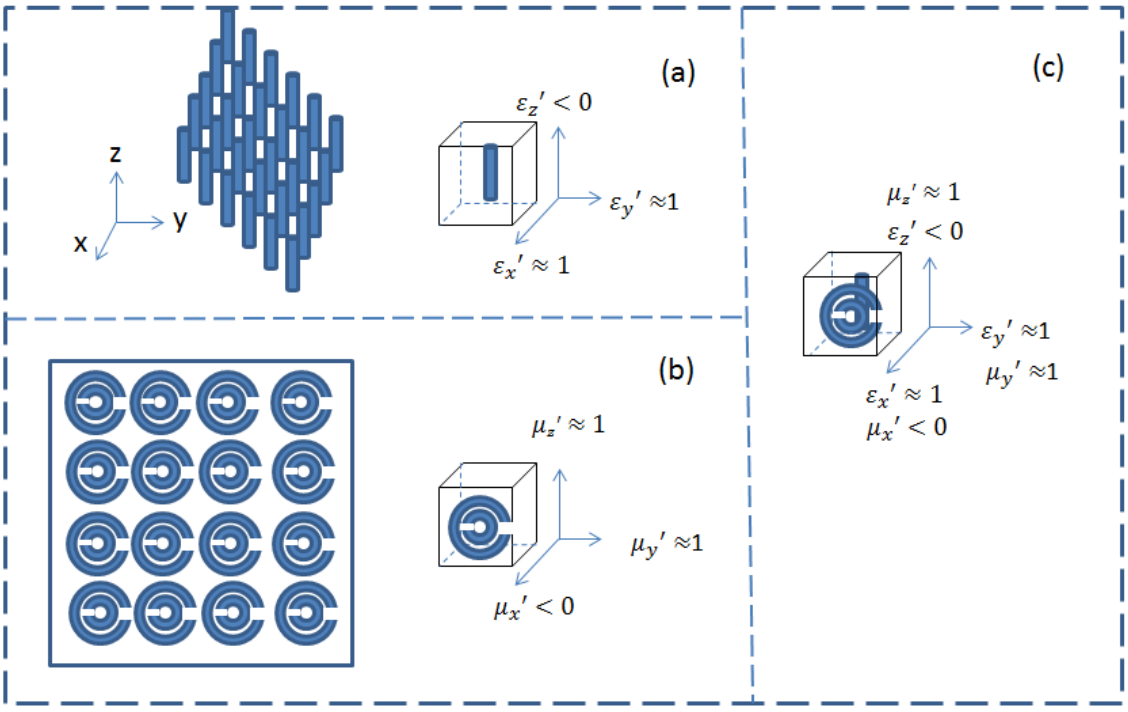

Figure 1.2. (a) Periodic array of thin metallic wires, (b) array of split ring resonators (SRRs), (c) double negative metamaterial(DNG MM) comprised by thin wires and SRRs are illustrated to show the negative values occurring for particular wave polarizations.

1.2 Epsilon-Negative (ENG) Metamaterials

As shown in Figure 1.2 (a), a periodic array of thin metallic rods can only generate negative permittivity for the incident wave with E field polarized parallel to the rod elongation direction. The frequency-dispersive Drude model can be adopted to describe the effective electric permittivity of the rods:

$$\varepsilon_{rz} = \varepsilon_{rz}' - \mathrm{j}\varepsilon_{rz}'' = 1 - \frac{{f_{ep}}^2}{f^2 - \mathrm{j}\,\gamma_e f/2\pi} \tag{1.1}$$

where f_{ep} is the electric plasma frequency, γ_e is the electric damping factor, with $\varepsilon_{rx}' \approx 1, \varepsilon_{ry}' \approx 1$.

It can be seen in (1.1) that if the material is operated at the frequencies lower than its electric plasma frequency, the negative real part of the permittivity can be obtained. Otherwise, the material will just behave like naturally existing materials, with only positive real parts of the permittivity.

1.3 MU-NEGATIVE (MNG) METAMATERIALS

Considering a single SRR as a small, capacitively loaded loop antenna operating slightly above the resonant frequency, the scattered magnetic field in the near-field will be out of phase with the incident field and result in a lower magnetic field than that of the incident field, i.e., a negative magnetic susceptibility that may cause negative permeability. The frequency-dispersive Lorentz model has the form given by

$$\mu_{rx} = \mu_{rx}' - \mathrm{j}\mu_{rx}'' = 1 - \frac{{f_{mp}}^2 - {f_{mo}}^2}{f^2 - {f_{mo}}^2 - \mathrm{j}\,\gamma_m f/2\pi} \tag{1.2}$$

where f_{mp} is the magnetic plasma frequency, f_{mo} is the magnetic resonant frequency and γ_m is the magnetic damping factor.

It can be observed that that if the material is operated at the frequencies higher than its magnetic plasma frequency or lower than its magnetic resonant frequency, the real part of the permittivity will be positive as the naturally existing materials. Only when operated in the frequency band between its magnetic plasma frequency and magnetic resonant frequency will it have negative real parts of the permeability.

In addition, the SRR structure [25] can be analogous to a series-parallel lumped-element circuit, as shown in Figure 1.3. The angular frequency of the magnetic resonance in radians can be described by the geometry parameters of the SRR structure as

$$\omega_{mo} = \frac{1}{\sqrt{LC}} = \frac{1}{l}\frac{c}{\varepsilon_c}\sqrt{\frac{d}{w}}. \tag{1.3}$$

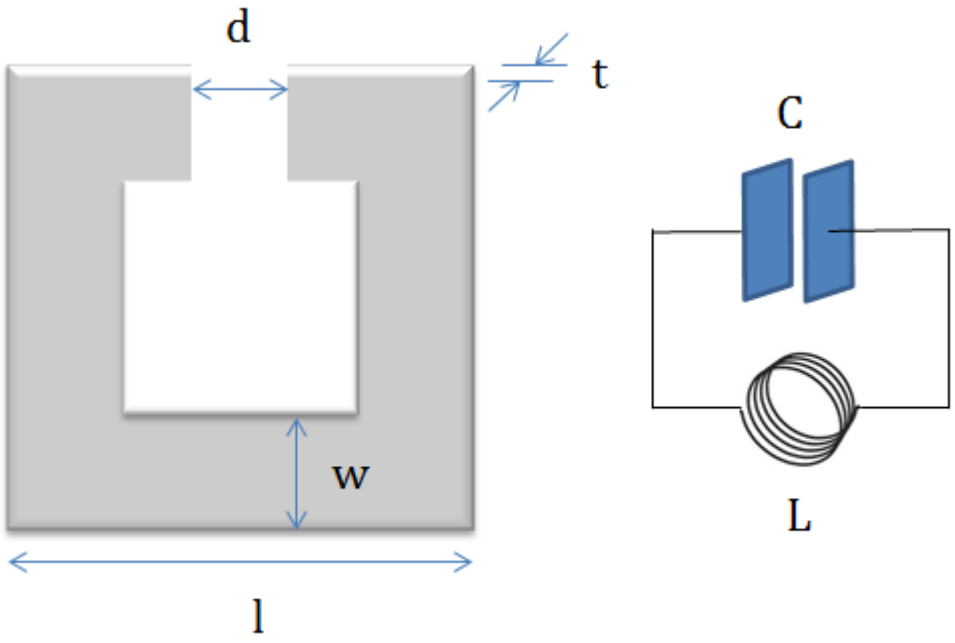

Figure 1.3. A single SRR structure and its equivalent lump circuit elements are depicted.

1.4 SRR-ROD TYPE DOUBLE NEGATIVE (DNG) METAMATERIALS

A typical SRR-rod metamaterial slab in THz band is simulated, and material properties such as electric permittivity, magnetic permeability, and refractive index are calculated and shown in Figure 1.4. The electric plasma frequency f_{ep} can be found in Figure 1.4 (a) at which $\varepsilon_{rz}' = 0$, so is the magnetic plasma frequency f_{mp} can be found in Figure 1.4 (b) at which $\mu_{rx}' = 0$. The green band is defined by f_{mp} and f_{ep}, where $n' \approx 0$. The yellow band is defined by magnetic resonant frequency f_{mo} and plasma frequency f_{mp}, where ε_{rz}' and μ_{rx}' are both negative. For strong resonating SRR-Rod metamaterials, the curve with gradually decreasing slope as shown in the orange band will exhibit asymptotic behavior with sharp decreasing slope.

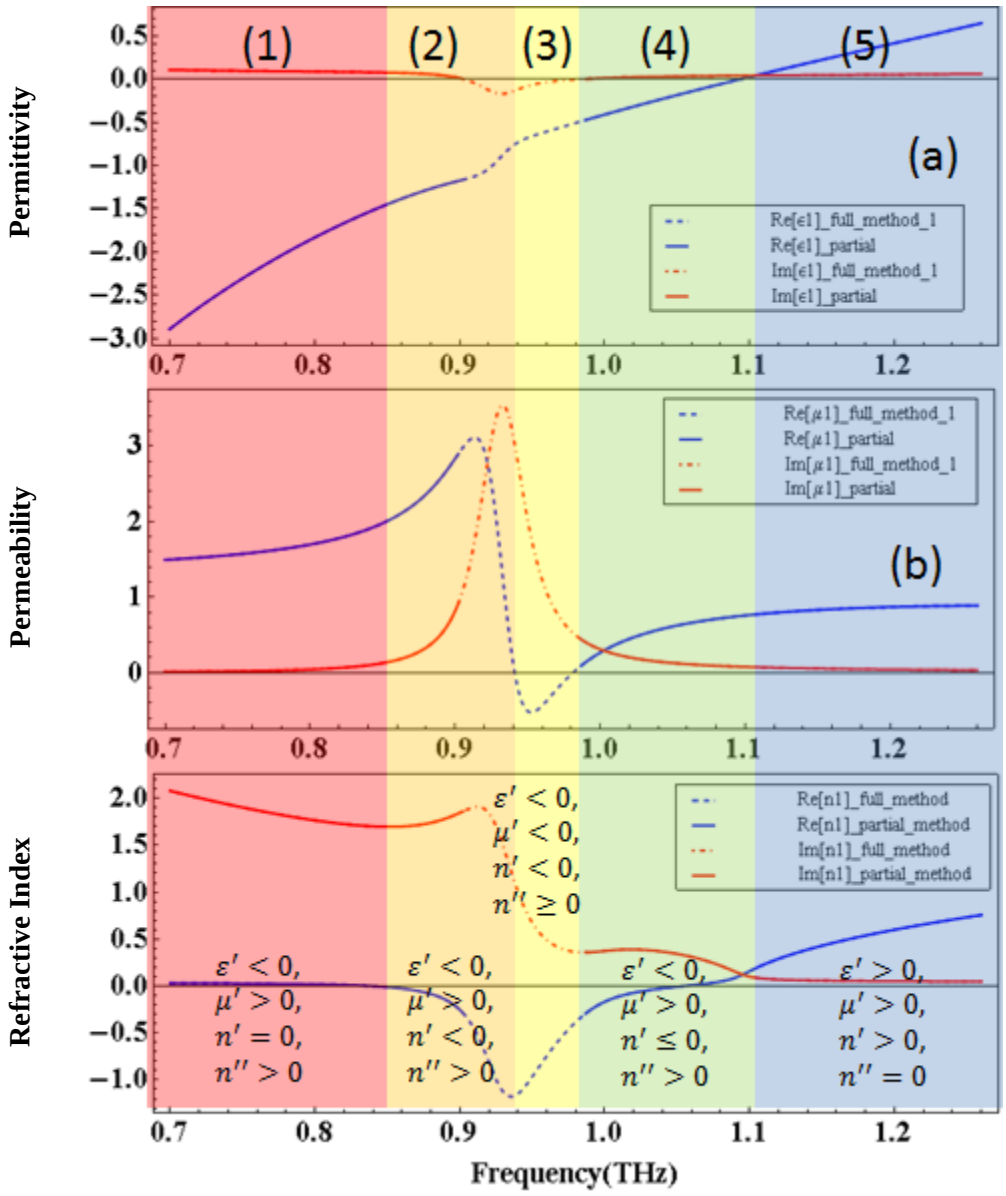

Figure 1.4. (a) Electrical permittivity, (b) magnetic permeability, and (c) refractive index of a typical SRR-Rod MMs in THz band show different signs of material properties and constitutive parameters at different frequency bands.

1.5 Applications of Metamaterials

Metamaterials have been utilized in microwave devices, such as antennas [26-29], wave couplers [30, 31], splitters [32, 33], and high impedance ground planes [34]. For example, the gain of a monopole antenna can be increased while remaining omnidirectional by covering it with a fractal metamaterial sheet. Another example is to use MMs to design backward leaky wave antenna [26, 35, 36]. Among all the applications, the two most 'futuristic' applications, are the super lens [21, 29, 37-39] and invisibility cloak [40].

The concept of the invisibility cloak is as follows: If a plane incident wave is impinging obliquely on a flat PEC (perfect electrical conductor) surface, the reflected wave should remain as a plane wave. If the wave impinges on a hump, then the reflected wave will not remain as a plane wave, and there will be a shadow zone. If the metamaterial cloak is placed on top of the hump, the reflected wave can still behave like a plane wave.

1.6 Proposed Pattern-less Electromagnetic Wave Manipulation by Active Control of Metamaterials

Traditionally, guiding and steering EM waves in the microwave frequency range use many kinds of waveguides [41, 42] and transmission lines [36, 42], some examples being coaxial cables, rectangular or circular metallic waveguides, striplines, and microstrip lines. They are categorized by the geometry designs or the polarizations and modes of the guided waves [43].

Coaxial cables and striplines are usually used to guide transverse electromagnetic (TEM) waves; however, due to high loss and bulky characteristics, they are not useful in high frequency operation. Rectangular and circular metallic waveguides can transmit high

power TE (transverse electric) or TM (transverse magnetic) waves, but not TEM waves. Therefore, this type of waveguide is always dispersive. In addition, since the waves are propagating in the hollow parts of the waveguides, the diffraction limit constrains the sizes of geometry designs.

Microstrip Lines are commonly seen in many microwave devices due to the compact sizes and easy integration with other devices. In addition, microstrip lines can transmit quasi-TEM waves, thus, are not as dispersive as rectangular or circular metallic waveguides. Dielectric rib waveguides [44] are usually used to guide TE or TM waves in THz and optical frequency bands, and can confine most of the waves within or around the rib, a medium with higher dielectric constant. However, this type of waveguide will have very high loss at curving or discontinuous parts. Optical fibers made of different dielectrics are also used in transmission of millimeter waves and lights in TM-like LP01 mode [45]. Unfortunately, bend losses and dispersion also exist in the optical fibers. Recently, a new hybrid design [46] applied the hollow concept of circular waveguides on dielectric rib waveguide, was proposed to guide the in THz. This type of waveguides has lower loss than dielectric rib waveguide since there are less lossy dielectric materials existing in the wave travelling path. Another hybrid design [47] uses the ground metal plate and high dielectric constant rib to confine EM waves.

However, the aforementioned devices can only transmit certain mode of waves in one fixed path once the geometries are defined. To prevent frequency dispersions and power losses, the best choice is a hollow-shaped waveguide that can transmit TEM waves. Therefore, in the proposed research, a new design utilizing hollow-shaped MMs that can transmit TEM waves in subwavelength dimensions and reroute the transmission path will be studied.

Lenses are the most common means of steering optical range waves. Traditionally, the convex or concave lens is made from a homogenous medium with a constant refractive index, inheriting optical aberration problems, as reported by Ernst Abbe in 1893. Gradient index (GRIN) lens is made of a material with gradual variations of the refractive

index, and thusly does not inherit the optical aberration problems of flat surfaces. In [48], a tunable GRIN lens is reported for the variable focusing of light using a microfluidic chamber to mix two fluids different refractive indices to create gradient refractive index effect on the lens. Theoretical study of using liquid crystal (LC) arrays in a GRIN lens is also reported in [49] in order to create active GRIN lenses with liquid crystal. Since the refractive index of polymer dispersed liquid crystal (PDLC) is related to the LC droplet sizes, a GRIN lens can be made from gradient PDLC for light control [50, 51]. However, the spatial resolutions of aforementioned GRIN lenses are still under the constraint of the diffraction limits due to the positive refractive index. Therefore, the research proposes a flat lens that can defeat the diffraction limit and optical aberrations.

The objective of this research is to create compact, multifunctional, and reconfigurable devices, such as a patternless waveguide that can confine THz TEM waves with subwavelength spatial resolution and guide the waves into different routes depending on the configurations of surrounding active metamaterials, and a multifunctional flat lens optical bench that can collimate the waves in THz, steer the beam direction, change the locations of the focal points and even do subwavelength focusing.

1.7 SUMMARY

This chapter introduced the background, motivation, objective and proposed approaches of this research. In Chapter 2, improved retrieval methods are proposed to extract the constitutive material properties of single-layered and multi-layered metamaterials based on the existing methods. The tuning mechanisms of active metamaterials (AMM) will be studied and proposed in Chapter 3. Two novel approaches to manipulate EM waves in subwavelength dimensions are offered and preliminary simulation results are discussed in Chapter 4. Finally, the conclusions and proposed future work will be given in Chapter 5.

Chapter 2. RETRIEVAL METHODS OF MATERIAL PROPERTIES AND CONSTITUTIVE PARAMETERS

To obtain the best simulation results for the proposed waveguide and gradient metamaterial design, the constitutive parameters and material properties of fundamental constitutive unit cells of metamaterials need to be determined and characterized. Several methods have been reported in [52-54], with the highly valuable method [54] proposed by D.R. Smith is based on the inversion of the scattering parameters calculated or measured from a plane wave normally incident on a slab of metamaterial to obtain material impedance and refractive index. In some instances, such as misestimating the thickness of the slab or very small values in magnitude of the scattering parameters, the method in [54] may fail with discontinuous material properties. In order to solve this issue, Kong *et al.* [52] proposed a much more robust method based on the modifications of the method in [54] while sacrificing and remaining an undetermined result in the resonant band, which is crucial for operating MMs in this frequency band for negative permittivity (ε) or permeability (μ) effects. Another key issue is to determine the effective boundary of MMs since the strong resonance occurring around the MMs makes distinguishing the material boundaries very difficult. Therefore, extra investigations are necessary in order to determine the exact solutions of material properties in the resonant frequency band.

In this chapter, the improved methods along with the patch algorithms were proposed in order to preserve the robustness of retrieval methods while keeping the ability to retrieve all effective material properties, such as refractive indices, impedances, and material constitutive parameters, such as the permittivity and the permeability, of metamaterials over the frequencies of the interest.

The first method modified from Kong's retrieval method allows effective constitutive parameters over all frequencies including the anti-resonant band, where imaginary parts of ε or μ are negative, to be solved. The second method is based on the genetic algorithm

and optimization of properly defined goal functions to retrieve parameters of Drude and Lorentz dispersion models. Equations of effective refractive index and impedance at any reference planes are derived. SRR-rod based metamaterials operating in Terahertz frequencies are designed and examined with the proposed methods. The retrieved material properties and constitutive parameters are used to regenerate S-parameters, and the regenerated S-parameters are compared with original simulated results by CST microwave studio software in order to see the accuracies of retrieved results by the proposed methods.

2.1 INTRODUCTION

Artificial electromagnetic media built of either periodically ordered or random scattered unit cells that possess negative real parts of the electric permittivity and magnetic permeability at certain frequencies are called double negative metamaterials (DNG MMs) [19, 55]. DNG MMs have attracted extensive attention of researchers in optics, applied electromagnetism, photonics, and material sciences during the past few years due to their unique applications, such as invisible cloaking, super lenses and reductions in antenna geometry [56-59]. In order to retrieve constitutive parameters of MMs as a homogeneous medium, a typical unit cell of MMs needs to satisfy the assumption of effective medium theory that the lattice size is much smaller than the operating wavelengths inside the medium. Several methods [54, 58, 60, 61] based on this assumption have been reported. Among them, the most widely used approach is to calculate the effective refractive index (n) and impedance (z) by inverting the reflection (S11) and transmission (S21) coefficients of the scattering parameters (S-parameters) from measurements or simulations, and derive the effective constitute parameters ε and μ from n and z. However, there are known issues of this process that may make the extraction fail, such as when either the magnitude of S11 or S21 is small or when the effective slab boundaries are not well estimated. Although these issues have been somewhat addressed in [52], the proposed modifications will help clarify the determination of effective

boundaries of MMs and simplify the process for choosing the correct refractive index from the multiple branches due to the inverse of logarithm or arccosine operator.

In addition, there is no refractive index retrieved in the resonance band defined in [52], at which no branch satisfies the requirements of lossy and passive medium. As a result, no constitutive parameters can be determined in the resonance band. In other words, transmission and reflection coefficients cannot be reconstructed from n and z. However, there should be a value of ε and μ at any frequency to describe material properties, where transmission and reflection coefficients can also be derived or measured. In this paper, two full extraction methods are proposed to retrieve constitutive parameters over the frequencies of the interest, including the resonant band. The first method allows the retrieval of constitutive parameters with negative imaginary parts of ε or μ. The second method is based on the passive material dispersive Drude and Lorentz models, allowing the retrieval of constitutive parameters with positive imaginary parts of ε and μ. The retrieval of the parameters in the Drude and Lorentz dispersion models is accomplished through genetic algorithms (GA) and the optimization method with well-defined goal functions and proper initial searching ranges for some variables.

2.2 THEORY FOR RETRIEVAL METHODS

The measured or simulated S-parameters of a homogeneous slab surrounded by air with the reference planes set at the slab boundaries in the wave travelling direction for a normal incident plane wave can be derived by the transfer matrix (ABCD matrix) method [62] and written as functions of effective material properties, such as refractive index n and normalized impedance z. Assuming that a slab with thickness d surrounded by air has a normalized impedance of $z = Z/z_0$ and wavenumber $k = k_0 n$, where z_0 and k_0 are the impedance and wavenumber of air, respectively, the ABCD matrix of the slab, which is related to the material properties and geometry of the media, can be represented as

$$\begin{bmatrix} A_m & B_m \\ C_m & D_m \end{bmatrix} = \begin{bmatrix} \cos(kd) & jz\sin(kd) \\ \frac{j\sin(kd)}{z} & \cos(kd) \end{bmatrix}. \tag{2.1}$$

The slab surrounded by air can be regarded as a two-port network device with source impedance z_S and load impedance z_L equal to z_0. The S-parameters of the slab measured at the slab boundaries can be converted from the ABCD matrix of the slab using [63, 64] as

$$\begin{bmatrix} S_{11} & S_{12} \\ S_{21} & S_{22} \end{bmatrix} = \begin{bmatrix} \frac{A\,z_L+B-C\,z_S z_L-D\,z_S}{A\,z_L+B+C\,z_S z_L+D\,z_S} & \frac{2\sqrt{z_S z_L}(A\,D-B\,C)}{A\,z_L+B+C\,z_S z_L+D\,z_S} \\ \frac{2\sqrt{z_S z_L}}{A\,z_L+B+C\,z_S z_L+D\,z_S} & \frac{-Az_L+B-C\,z_S z_L+D\,z_S}{A\,z_L+B+C\,z_S z_L+D\,z_S} \end{bmatrix}. \tag{2.2}$$

The S-parameters in terms of refractive index n, normalized impedance z and slab thickness d can be obtained by rewriting the results of (2.2) into exponential forms as follows, considering multiple reflections of waves between different interfaces in agreement with Nicolson-Ross-Weir (NRW) method [60],

$$S_{11} = \frac{\Gamma\left(1-e^{-2jk_0nd}\right)}{1-\Gamma^2 e^{-2jk_0nd}} \tag{2.3}$$

$$S_{21} = \frac{e^{-jk_0nd}\left(1-\Gamma^2\right)}{1-\Gamma^2 e^{-2jk_0nd}} \tag{2.4}$$

where $\Gamma = \frac{Z-Z_0}{Z+Z_0} = \frac{z-1}{z+1}$ is the reflection coefficient at the boundary between free space and the medium with infinite thickness and the normalized impedance z.

From [63, 64], the S-parameters of the slab measured at the slab boundaries can be inverted to represent ABCD matrix of the slab in another form by

$$\begin{bmatrix} A_s & B_s \\ C_s & D_s \end{bmatrix} = \begin{bmatrix} \sqrt{\frac{z_S}{z_L}}\frac{(1+S_{11})(1-S_{22})+S_{21}S_{12}}{2S_{21}} & \frac{\sqrt{z_S z_L}[(1+S_{11})(1+S_{22})-S_{21}S_{12}]}{2S_{21}} \\ \frac{1}{\sqrt{z_S z_L}}\frac{(1-S_{11})(1-S_{22})-S_{21}S_{12}}{2S_{21}} & \sqrt{\frac{z_L}{z_S}}\frac{(1-S_{11})(1+S_{22})+S_{21}S_{12}}{2S_{21}} \end{bmatrix}. \tag{2.5}$$

By examining the element A in the ABCD matrix and setting $A_m = A_s$ in (2.1) and (2.5), the refractive index n can be determined by

$$n = \frac{\pm 1}{k_0 d}\left(\cos^{-1}\frac{1-{S_{11}}^2+{S_{21}}^2}{2\,S_{21}} + 2\,\pi\,m\right) \tag{2.6}$$

where m is an integer representing the branch index of n due to arccosine operation.
The normalized impedance z of the slab can be obtained by dividing B over C in ABCD matrix and equate $B_m/C_m = B_s/C_s$ in (2.1) and (2.5) as follows,

$$z = \pm\sqrt{\frac{(1+S_{11})^2-{S_{21}}^2}{(1-S_{11})^2-{S_{21}}^2}}\,. \tag{2.7}$$

Since the medium of the slab is considered as a passive and lossy material, the refractive index n and the impedance z of the slab have to satisfy the following requirements as shown in DR Smith's method,

$$n'' \geq 0 \tag{2.8}$$

$$z' \geq 0 \tag{2.9}$$

where $(.)'$ and $(.)''$ represent the real part and the imaginary part operators, respectively. The ambiguity of the signs of the refractive index n and the impedance z can then be determined by (2.8) and (2.9).

2.2.1 *Simulation Models*

The model is based the split ring resonator (SRR) rod design shown in [19]. The size of the DNG unit cell is reduced for THz operation (Figure 2.1). The dimensions of the unit cell are the lattice size $a = 50\ \mu m$, ring spacing $b = 5\ \mu m$, outer SRR height $h = 30\ \mu m$, strip width $w = 2.5\ \mu m$, and gap width $g = 5\ \mu m$ for the SRR-Rod model-1, and $2.5\ \mu m$ for SRR-Rod model-2. The dielectric material with $2.5\ \mu m$ thickness between copper

SRR and copper rod, are characterized by $\varepsilon_r = 3.84$ and $\tan\delta = 0.018$. The slab thickness L_m is determined by the numbers of unit cell in the $\hat{z}$ direction.

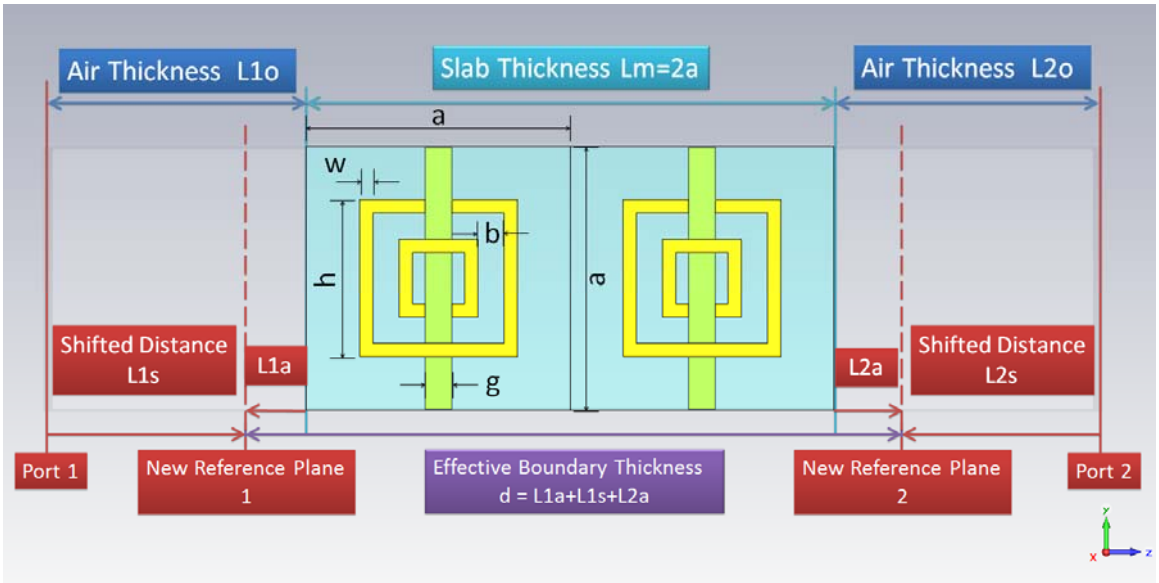

Figure 2.1. Geometry of a two-cell SRR-Rod metamaterial slab with effective boundaries at new reference planes. For a single cell slab, the slab thickness L_m is a. For the two-cell slab (two unit cells stacked in the $\hat{z}$ direction), the slab thickness $L_m = 2a$.

Assume a plane incident wave with the electric field polarized in the $\hat{y}$ direction is propagating in the $\hat{z}$ direction. The periodicities of the DNG unit cell in the $\hat{x}$ and $\hat{y}$ directions are implemented using Floquet boundary conditions. S-parameters of the metamaterial slab with one or two cells in the wave propagation direction can be simulated using a frequency domain solver with the Floquet ports set originally $L1_0 = L2_0 = 75\ \mu m$ away from the slab/air interfaces in the $\hat{z}$ direction.

2.2.2 *Effective Material Boundaries for Metamaterials*

For a homogenous slab of passive material with well-defined boundaries, the constitutive parameters n and z can be retrieved from the S-parameters and the slab thickness by (2.6) and (2.7) with the requirements of passive materials, (2.8) and (2.9). However, for a strong resonant metamaterial, the location of the effective boundaries between the slab

and air need to be determined. When a plane wave propagates through a metamaterial, the wave will not act like a plane wave inside and around the metamaterial because of the nonuniform scattering fields produced by the induced current on the metal. However, when a plane wave is incident normal to a homogenous slab from free space, the wavefront will remain planar and perpendicular to the propagating direction through different homogenous media. Therefore, it is not a good idea to determine the boundaries of a homogenous slab in free space by searching for the locations at which the wave behaves as a plane wave.

Another method to determine the effective boundaries of a homogeneous slab utilizes the slab's impedance, independent of its thickness. By inspecting the impedance difference of two different slabs with different numbers of unit cells stacked in the direction of wave propagation, the effective boundaries of the slabs can be defined at the locations where the impedance difference of two slabs with different thickness is minimized, as shown in Figure 2.1.

The original goal function of the optimization model defined in [52] is set up to find the locations of new reference planes around two slabs such that the impedance mismatch between the slabs at their effective boundaries is minimized:

$$\min \sum_{f_i=1}^{N_f} \frac{|z_1(f_i,\bar{x}) - z_2(f_i,\bar{x})|}{\max\{|z_1(f_i,\bar{x})|, |z_2(f_i,\bar{x})|\}} \tag{2.10}$$

where N_f is the total number of samples of frequencies of interest and $z_j(f_i,\bar{x})$ is the impedance of slab j measured at frequency f_i with effective boundaries set at new reference planes $\bar{x} = (L1_s, L2_s)$. Positive signs of $(L1_s, L2_s)$ denote that the new reference planes are shifted outward from the slab while negative signs of $(L1_s, L2_s)$ denote that the new reference planes are shifted inward toward the slab from the original locations $(L1_0, L2_0)$.

Here, two new goal functions of the optimization model are defined to find the effective boundaries where the impedance mismatch at the investigated frequencies is minimized and equally weighted in the magnitude and phase terms or the real and imaginary parts of the impedance:

$$\min \sum_{f_i=1}^{N_f} \frac{||z_1(f_i,\bar{x})|-|z_2(f_i,\bar{x})||}{\max\{|z_1(f_i,\bar{x})|,|z_2(f_i,\bar{x})|\}} + \frac{||\angle z_1(f_i,\bar{x})|-|\angle z_2(f_i,\bar{x})||}{\max\{|\angle z_1(f_i,\bar{x})|,|\angle z_2(f_i,\bar{x})|\}} \tag{2.11}$$

$$\min \sum_{f_i=1}^{N_f} \frac{|z_1{}'(f_i,\bar{x})-z_2{}'(f_i,\bar{x})|}{\max\{|z_1{}'(f_i,\bar{x})|,|z_2{}'(f_i,\bar{x})|\}} + \frac{|z_1{}''(f_i,\bar{x})-z_2{}''(f_i,\bar{x})|}{\max\{|z_1{}''(f_i,\bar{x})|,|z_2{}''(f_i,\bar{x})|\}} \tag{2.12}$$

Three goal functions are selected to generate the density plots of mismatched impedance within the searching range of $(L1_s, L2_s)$ set from $-80\ \mu m$ to $80\ \mu m$, as shown in Figure 2.2 (a-c). The darker zone represents smaller value of mismatch of the impedances. In Figure 2.2 (d-f), there are at least three local minimums along the diagonal line ($L1_s = L2_s$) on 2D density plots and two local minimums along the anti-diagonal line ($L1_s = -L2_s$) . The locations of the global minimum of the original goal function are at $(L1_s, L2_s)$. They are either equal to $(-40\ \mu m, 40\ \mu m)$ or $(40\mu m, -40\mu m)$ while the locations of the global minimum of the other two goal functions are both at $L1_s = L2_s = -73\ \mu m$. The original definition of the goal function does not give the equal weight on the magnitude and phase of the impedance, $z'$and z''. As a result, the impedances of the two slabs at locations retrieved by the original goal function do not have similar real and imaginary parts of the impedance at the frequencies of interest.

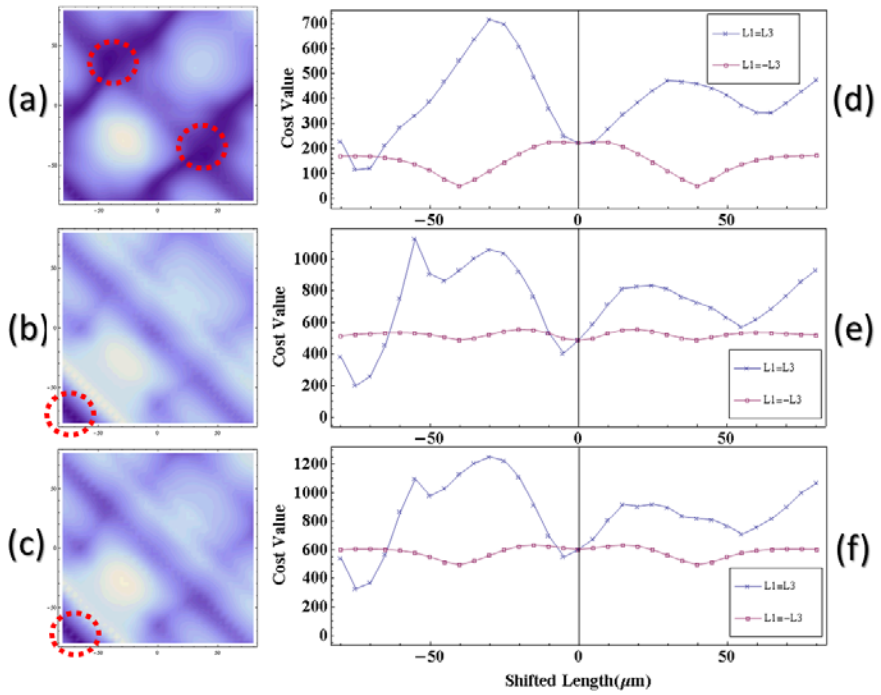

Figure 2.2. (a) 2D density graph of the goal function defined in [52] with x,y axes denoting searching range of L1s and L2s, respectively. (b) and (c) are 2D density graphs of the proposed goal functions defined in eq. (2.11) and (2.12). (d), (e) and (f) are 1D graphs along diagonal and anti-diagonal directions of 2D density graphs of (a), (b), and (c), respectively.

It is worth noting that the retrieved effective boundaries occurred where the two slabs of unequal thickness obtain the same impedance, i.e., the effective impedance at the retrieved boundaries is somehow independent of the slab thickness. However, as shown in Figure 2.3, the wave observed at the retrieved effective boundaries does not behave like a plane wave when viewed in 3D simulation software (CST AG, Germany) because the wave is still being affected by the strong resonant structure of the DNG unit cell.

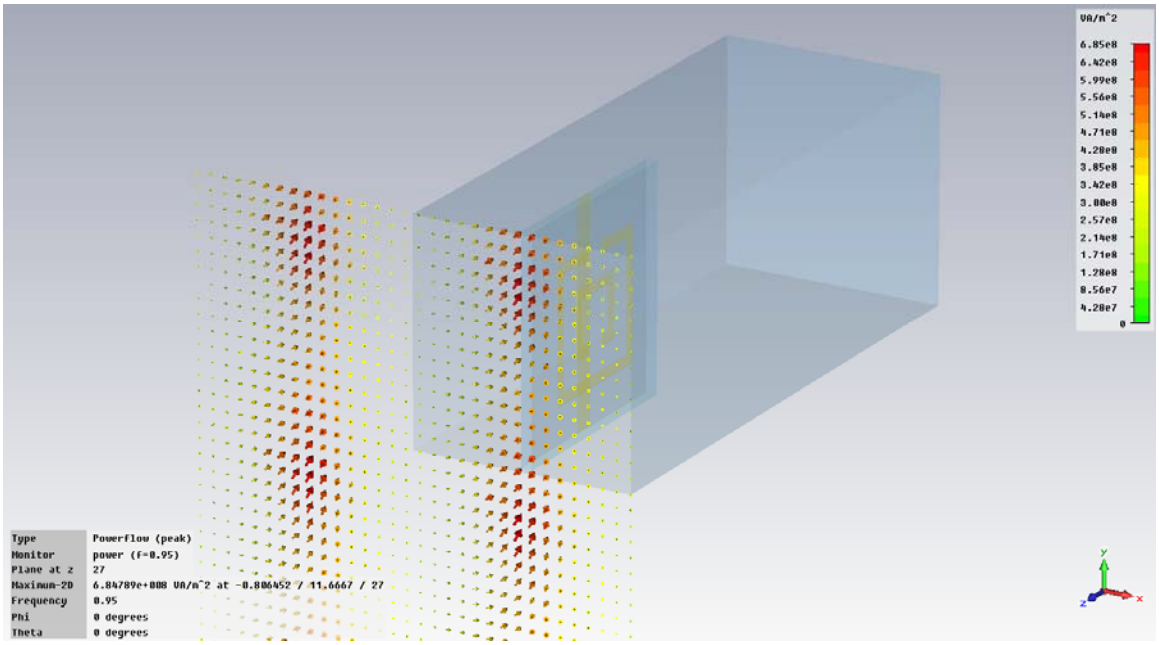

Figure 2.3. 3D Power flow of incident EM wave at $L1_s = L2_s = -73\ \mu m$

To figure out the exact location of a plane wave closest to the metamaterial slab, the reference planes are shifted and the corresponding effective refractive indices are calculated, as depicted in Figure 2.4. The plane wave will occur at the boundaries, $L1_s = L2_s = -35\ \mu m$, where the effective refractive index $n' = 1$. The uniformly distributed Poynting vectors at the boundaries indicating the uniformly distributed power flow of a plane wave are shown in Figure 2.5.

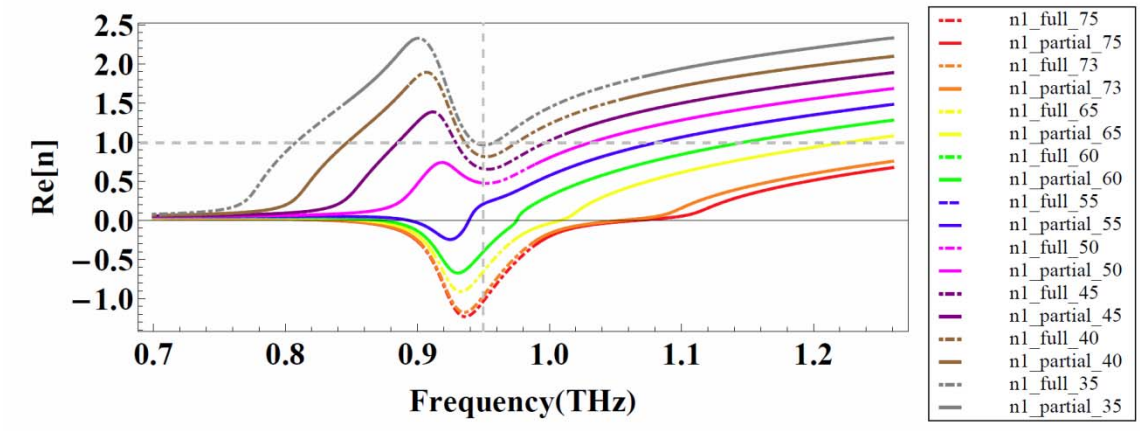

Figure 2.4. The real part of effective refractive index n' at different reference planes

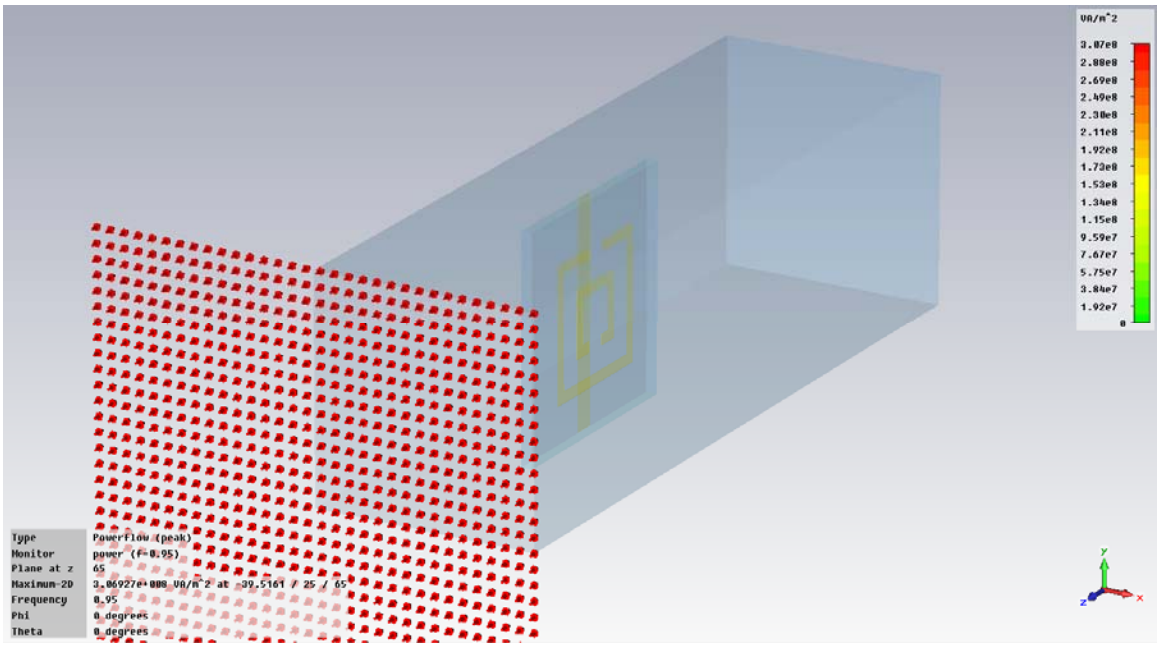

Figure 2.5. 3D Power flow of incident EM wave at $L1_s = L2_s = -35\ \mu m$

2.2.3 *Equations of Effective Impedance and Refractive Index at Any Reference Plane*

To calculate the goal functions defined in (2.10), (2.11) and (2.12), the effective impedance equation at any reference plane in air has to be derived. Considering a L_m thick slab of a metamaterial surrounded by air with effective boundaries located at $(L1_a, L2_a) = (L1_o + L1_s, L2_o + L2_s)$ away from the slab/air interfaces in the $\hat{z}$ direction respectively, the effective ABCD matrix can be represented by cascading ABCD matrices of the air, MM and air slab:

$$ABCD_e = ABCD_{L1_a} \cdot ABCD_{L_m} \cdot ABCD_{L2_a} \tag{2.13}$$

where $ABCD_{L1_a}$ and $ABCD_{L2_a}$ are the ABCD matrices, obtained from (2.1), of the air slabs with respective thicknesses $L1_a$ and $L2_a$. $ABCD_{L_m}$ is the ABCD matrix of the MM slab represented in terms of S-parameters measured originally at the slab/air interfaces by (2.5).

Since the overall slab containing air and the metamaterial has total thickness $d = L1_a + L_m + L2_a$ and can be described by effective constitutive parameters, such as normalized effective impedance z_e and refractive index n_e, the effective ABCD matrix can also be written by (2.1) as

$$\begin{bmatrix} A_{em} & B_{em} \\ C_{em} & D_{em} \end{bmatrix} = \begin{bmatrix} \cos(k_e d) & jz_e \sin(k_e d) \\ \frac{j \sin(k_e d)}{z_e} & \cos(k_e d) \end{bmatrix} \tag{2.14}$$

where $k_e = k_0 n_e$ is the effective wavenumber of the overall slab.

The normalized effective impedance z_e can be obtained by comparing B/C terms in the effective ABCD matrices in (2.13) and (2.14)

$$z_e = \pm j \sqrt{\frac{-j({S_{11}}^2 - {S_{21}}^2 - 1)\mathrm{S(L)} + ({S_{11}}^2 - {S_{21}}^2 + 1)\mathrm{C1(L)} + 2S_{11}\mathrm{C2(L)}}{j({S_{11}}^2 - {S_{21}}^2 - 1)\mathrm{S(L)} + (-{S_{11}}^2 + {S_{21}}^2 - 1)\mathrm{C1(L)} + 2S_{11}\mathrm{C2(L)}}} \tag{2.15}$$

where $S(L) = \sin(k_0(L1_a + L2_a))$, $C1(L) = \cos(k_0(L1_a + L2_a))$, and $C2(L) = \cos(k_0(L1_a - L2_a))$.

The effective refractive index n_e can be determined by examining the A element in the ABCD matrices in (2.13) and (2.14) as

$$n_e = \frac{\pm 1}{k_0 d}\left(\cos^{-1}\frac{F(S)}{2\,S21} + 2\,\pi\,m\right) \tag{2.16}$$

where $F(S) = -j\big(\sin\big(k_0(L1_a + L2_a)\big)(-S_{11}S_{22} + S_{12}S_{21} - 1) + (S_{11} + S_{22})\sin\big(k_0(L1_a - L2_a)\big)\big) + \cos\big(k_0(L1_a + L2_a)\big)(-S_{11}S_{22} + S_{12}S_{21} + 1) + (S_{11} - S_{22})\cos\big(k_0(L1_a - L2_a)\big)$.

The effective S-parameters measured at new reference planes can be retrieved from effective ABCD matrices in (2.13) and (2.2):

$$\begin{bmatrix} S11_e & S12_e \\ S21_e & S22_e \end{bmatrix} = \begin{bmatrix} S_{11}\, e^{-jk_0 2\, L1_a} & S_{12} e^{-jk_0 (\, L1_a + L2_a)} \\ S_{21} e^{-jk_0 (\, L1_a + L2_a)} & S_{22}\, e^{-jk_0 2\, L2_a} \end{bmatrix}. \tag{2.17}$$

In (2.17), additional phase delay has been added in the reflected waves, $S11_e$ and $S22_e$, due to the additional distance waves have to travel in the air, i.e., twice the added air thickness ($2\, L1_a, 2\, L2_a$). For transmitted waves, the additional distance the waves have to travel is $L1_a + L2_a$.

2.2.4 *Determination of Effective z and n'' from S-parameters*

As indicated in [52, 59], the sign ambiguity of the impedance in (2.7) and (2.15) can be determined by applying the passive and lossy material conditions in (2.8) and (2.9). For this, the n'' derived from (2.3) and (2.4) can also be written in exponential form [52]:

$$n'' = \frac{-(\ln e^{-jk_0 n\, d})'}{k_0 d}. \tag{2.18}$$

And from (2.3) and (2.4), $e^{-jk_0 nd}$ can be written in terms of S-parameters and the impedance z as [52]:

$$e^{-j\, k_0 n\, d} = \frac{S_{21}}{1 - S_{11}\frac{z-1}{z+1}}. \tag{2.19}$$

From (2.8), (2.18) and (2.19), the equivalent condition of passive and lossy media for n'' can be obtained as

$$\left| e^{-jk_0 nd} \right| = \left| \frac{S_{21}}{1 - S_{11}\frac{z-1}{z+1}} \right| \leq 1\,. \tag{2.20}$$

By using conditions in (2.20) and (2.9), the sign ambiguity of the impedance calculated from S-parameters as seen in (2.7) and (2.15) can be uniquely determined, and n'' can also be obtained uniquely from (2.18).

2.2.5 *Partial Retrieval Method of n' from Multiple Branches*

The ambiguity of n' exists in the signs and the branch index m (seen in (2.6) and (2.16)) because of the arccosine function, and can be determined by $\varepsilon'' \geq 0$ and $\mu'' \geq 0$ along with the mathematical continuity of the parameters [54]. Since $\mu = n\,z$ and $\varepsilon = n/z$, the requirements of positive ε'' and μ''can be combined into one condition [52] as

$$|n'z''| \leq n''z' \ . \tag{2.21}$$

By applying (2.21) to n' at all frequencies of the interest, a table of m candidates at each frequency that satisfies the condition in (2.21) can be created first. It is likely that at some frequencies, there will be multiple m candidates due to small values of z''or n'' , or there will be no m candidate due to large number of conductive metal rods with strong EM couplings that cause negative ε''or μ''. Most often, there will be only one m candidate at each frequency, which can be used as an initial seed in the determination of the branch.

The mathematical continuity of the parameter n' can be applied by examining Taylor series expansion of e^{-jk_0nd} at frequency f_i and f_{i+1}. Instead of solving the binomial equation proposed in [52] and doing the value comparisons twice to determine the right branch index m at frequency f_{i+1} by the known value of m at frequency f_i, a goal function is defined to find the m value from the table of m candidates at frequency f_{i+1} that minimize the difference of e^{-jk_0nd} at f_i and f_{i+1} as

$$\min_{m_j(f_{i+1})} e^{-jk_0nd}(f_i)\left(1+\Delta+\frac{\Delta^2}{2}\right) - e^{-jk_0nd}(f_{i+1}) \tag{2.22}$$

where $e^{-jk_0nd}(f_i)$ denotes the value of e^{-jk_0nd} at frequency f_i and can be obtained from (2.19), $k_0(f_i)$ denotes the wave number in free space at frequency f_i, $n\big(m_j(f_{i+1}), f_{i+1}\big)$ denotes the refractive index of the branch m_j at frequency f_{i+1},
and $\Delta = -jk_0(f_{i+1})n\big(m_j(f_{i+1}), f_{i+1}\big)d - (-jk_0(f_i)n(m(f_i), f_i)d)$.

By applying the optimization model described in (2.22) on the table of m candidates created by (2.21), the right branch of n' from m candidates can be determined and the refractive index can be partially retrieved at the investigated frequencies since there might be no m candidates at some frequencies, such as the resonant band defined in [52] or anti-resonant zone defined in [65].

2.2.6 *Full Retrieval Method of n'*

In order to retrieve n' at frequencies where there is no m candidate that satisfies the condition in (2.21), a full retrieval method was proposed to retrieve n' based on the partially retrieved n' from the procedures in Section 2.2.1-2.2.5. Partially retrieved values of n'at the investigated frequencies were used as known seeds in the forward extraction algorithm.

The algorithm is modified from (2.22) by searching the m value from all integers instead of from the table of m candidates that minimize the difference of e^{-jk_0nd} at f_i and f_{i+1}. Instead of the condition defined in (2.21), the physical rules applied in this algorithm are (2.8) and (2.9), the same as those used in D.R. Smith's method. As this algorithm scans through all investigated frequencies, the n' can be fully retrieved. Furthermore, since the effective refractive index n and the effective impedance z are fully retrieved for all frequencies, μ and ε can also be fully obtained, as shown in Figure 2.6. The solid lines denote the values retrieved by the partial retrieval method and the dashed lines denote the values retrieved by the full retrieval method. Notice that the values of ε'' in the dashed line are negative. This is why there are no m candidates at this frequency band, while the values of μ'' in the solid and dashed lines are both positive. The procedures of the partial and full retrieval methods are illustrated in Figure 2.7.

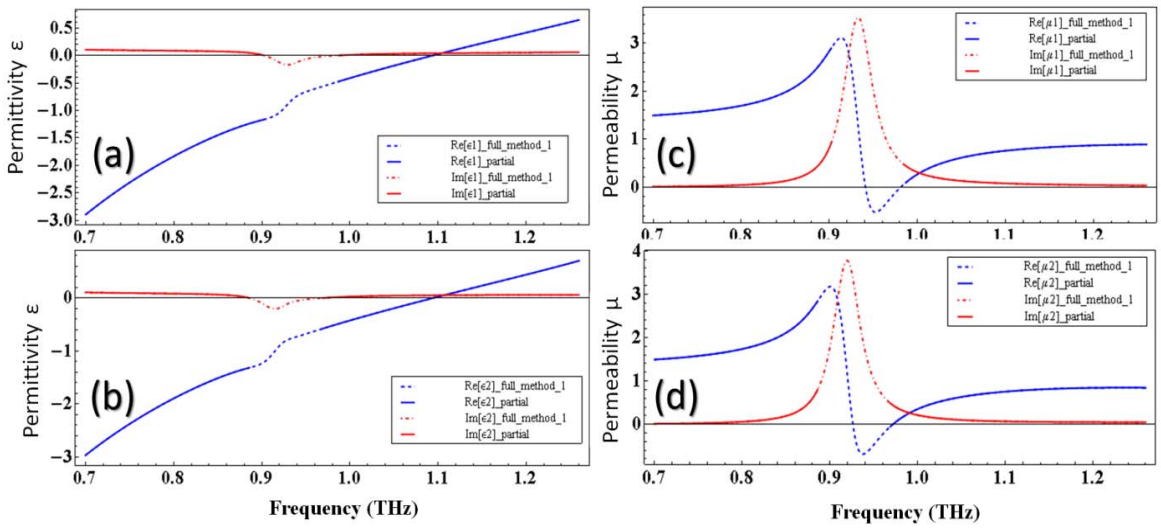

Figure 2.6. Retrieved permittivity and permeability of single cell and two cell metamaterial slabs are shown in (a), (c) and (b), (d), respectively.

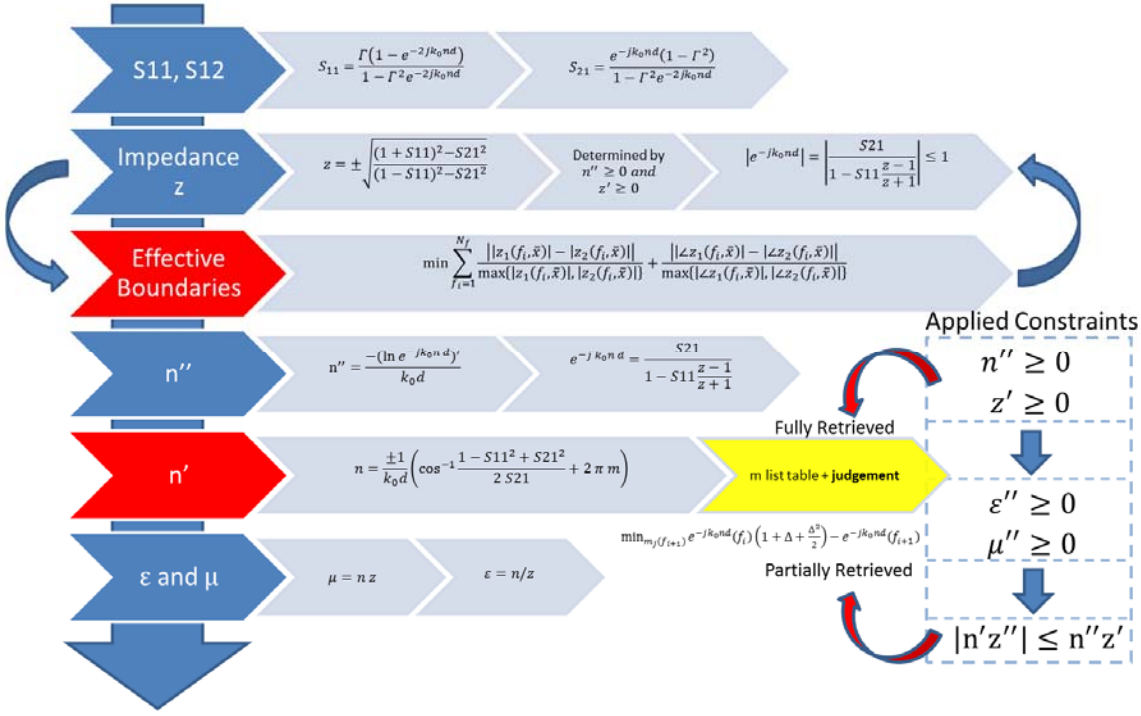

Figure 2.7. Flow chart of the proposed (partial and full) retrieval methods

2.3 RETRIEVAL METHOD BASED ON DISPERSION MODELS

Since the first full retrieval method proposed in this research will extract negative ε'' or μ'' at some frequencies and it is still arguable whether parameters can be extracted near the resonant band where ε'' or μ'' is negative or the anti-resonant band where ε'' and μ'' have different signs [61, 66, 67], the second full retrieval method was proposed to extract μ and ε with all positive ε'' and μ'' based on parameterized dispersive Drude and Lorentz models defined in (2.23)-(2.25) and partially retrieved impedance z and refractive index n of the slab shown in Figure 2.1 by the procedures proposed in Section 2.2.

2.3.1 *Drude and Lorentz Models*

Because the effective impedances z and refractive indices n of the single and two cell MMs slabs at the effective boundaries are similar, the effective homogenous slab can be modeled with the effective dielectric dispersion $\varepsilon_{eff}(\omega)$ described by the Drude model in (2.23) or by the Lorentz model in (2.24), with the effective magnetic dispersion $\mu_{eff}(\omega)$ described by Lorentz model in (2.25) to represent the original DNG MMs slab.

$$\varepsilon_{eff}(\omega) = \varepsilon_{\infty} - \frac{{\omega_p}^2}{\omega(\omega - j\omega_c)} \tag{2.23}$$

where ε_{∞} is the permittivity at the high frequency limit, ω_p is the radial plasma frequency, and ω_c is the collision frequency.

$$\varepsilon_{eff}(\omega) = \varepsilon_{\infty} + \frac{(\varepsilon_s - \varepsilon_{\infty}){\omega_0}^2}{{\omega_0}^2 + j\omega\delta - \omega^2} \tag{2.24}$$

where ε_s and ε_{∞} are the permittivity at the low and high frequency limit, respectively, ω_0 is the resonance frequency, and δ is the damping frequency.

$$\mu_{eff}(\omega) = \mu_{\infty} + \frac{(\mu_s - \mu_{\infty})\omega_0{}^2}{\omega_0{}^2 + j\omega\delta - \omega^2} \tag{2.25}$$

where μ_s and μ_{∞} are the permeability at the low and high frequency limit, respectively, ω_0 is the resonance frequency, and δ is the damping frequency.

The reference data ε_{ref} and μ_{ref} for the optimization models can be obtained from the retrieved impedance z and refractive index n in Chapter 2 by

$$\varepsilon_{ref}(\omega) = n_{retrieved}(\omega)/z_{retrieved}(\omega) \tag{2.26}$$

$$\mu_{ref}(\omega) = n_{retrieved}(\omega) \times z_{retrieved}(\omega)\ . \tag{2.27}$$

2.3.2 *Optimization Methods*

Goal functions for finding the parameters of dielectric permittivity and magnetic permeability dispersion model are defined as follows:

$$\begin{aligned} \min G_{\varepsilon} &= \min \sum_{f_i} Abs\left(\left|\varepsilon_{eff}(\omega_i)\right| - \left|\varepsilon_{ref}(\omega_i)\right|\right) \\ &+ \min \sum_{f_i} Abs\left(\angle\varepsilon_{eff}(\omega_i) - \angle\varepsilon_{ref}(\omega_i)\right) \end{aligned} \tag{2.28}$$

$$\begin{aligned} \min G_{\mu} &= \min \sum_{f_i} Abs\left(\left|\mu_{eff}(\omega_i)\right| - \left|\mu_{ref}(\omega_i)\right|\right) \\ &+ \min \sum_{f_i} Abs\left(\angle\mu_{eff}(\omega_i) - \angle\mu_{ref}(\omega_i)\right) \end{aligned} \tag{2.29}$$

To speed up the optimization calculation and prevent the solution of optimal parameters from falling into the goal function's local minimum, proper constraints (e.g. $\delta > 0$) and initial search ranges for certain parameters (e.g. ε_s, ε_{∞}, ω_0, μ_s and μ_{∞}) are necessary.

For example, the initial search range for μ_∞ can be set from $0.8\,\mu_{ref}(\omega_\infty)$ to $1.2\,\mu_{ref}(\omega_\infty)$. If there is a resonant band at the investigated frequencies, the initial search range for ω_0 can be set to the resonant band. There are several algorithms that can be adopted to perform optimization of the goal functions, such as Differential Evolution, a genetic algorithm (GA) that is robust but somewhat slower than other algorithms due to a large set of data points required during iterations [68].

Using (2.26) and (2.27), ε and μ can be calculated directly from n and z. However, to evaluate n_{eff} and z_{eff} from ε_{eff} and μ_{eff}, the equations (2.26) and (2.27) cannot just be inverted to calculate n_{eff} and z_{eff} by $\sqrt{\mu_{eff}\varepsilon_{eff}}$ and $\sqrt{\mu_{eff}/\varepsilon_{eff}}$, respectively. The proper formulae take into consideration the right phase terms of operands as follows:

$$z_{eff} = \left(|\mu_{eff}| / |\varepsilon_{eff}|\right)^{1/2} e^{j\frac{\angle\mu_{eff} - \angle\varepsilon_{eff}}{2}}, \tag{2.30}$$

$$n_{eff} = \left(|\mu_{eff}| \cdot |\varepsilon_{eff}|\right)^{1/2} e^{j\frac{\angle\mu_{eff} + \angle\varepsilon_{eff}}{2}}. \tag{2.31}$$

The retrieved optimal parameters of Drude and Lorentz models for the single cell SRR-Rod models 1 and 2 illustrated in Figure 2.1 with effective boundaries set at $L1_s = L2_s = -73\ \mu m$ are given in Table 2.1. The only difference between model 1 and model 2 is the width of the straight conductive rod. The effective permittivity ε_{eff} and permeability μ_{eff}, obtained by the second full retrieval method proposed in this dissertation, are respectively plotted in Figure 2.8 and Figure 2.9, and compared with other aforementioned retrieval methods.

Table 2.1 Retrieved Drude/Lorentz Parameters of two models of Single-layered SRR-Rod MMs

Parameters	SRR-Rod Model 1	SRR-Rod Model 2[a]
μ_∞	1.144	1.111
μ_s	1.294	1.254
δ	0.245 THz	0.223 THz
ω_0	5.862 THz	5.942 THz
ε_∞	2.104	1.962
ω_p	9.955 THz	9.035 THz
ω_c	0.107 THz	0.149 THz

a. Rod width of SRR-Rod Model2 is only half of Model1's

From Figure 2.8 and Figure 2.9, it can be seen that a DNG behavior occurs in the frequency band 0.94-0.99 THz, and the ε_{eff} retrieved by the first full retrieval method has negative ε_{eff}'' at the resonant frequency band, as plotted in the red dashed line in Figure 2.8, while the ε_{eff} retrieved by the second full retrieval method based on Drude and Lorentz models at all frequencies of interest has $\varepsilon_{eff}'' \geq 0$. In addition, the ε_{eff} obtained by all proposed methods agree with each other very well at all frequencies, except for the resonant frequency band.

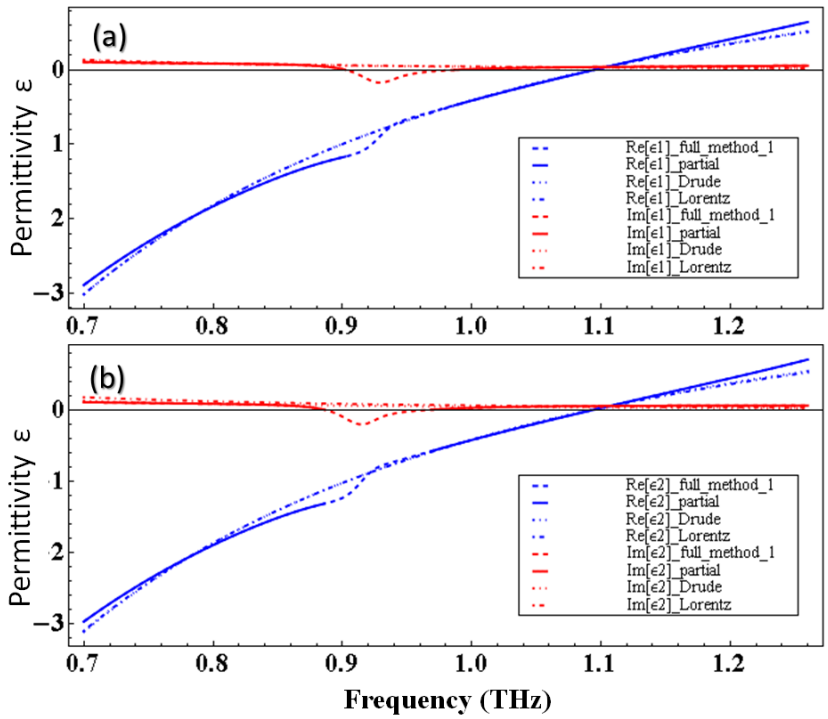

Figure 2.8. Effective permittivity ε_{eff} of the (a) single and (b) two-cell MMs slabs retrieved by different methods.

In Figure 2.9, it can be seen that μ_{eff}'' is positive at all frequencies of interest. The values of μ_{eff} obtained by all the proposed methods are in excellent agreement at all frequencies (including the resonant frequency band), because there is only the negative ε_{eff}'' occurring at the resonant frequency band and yielding discrepancy of ε_{eff} retrieved by the first and second full retrieval methods, with no negative μ_{eff}'' creating a similar effect as ε_{eff}''.

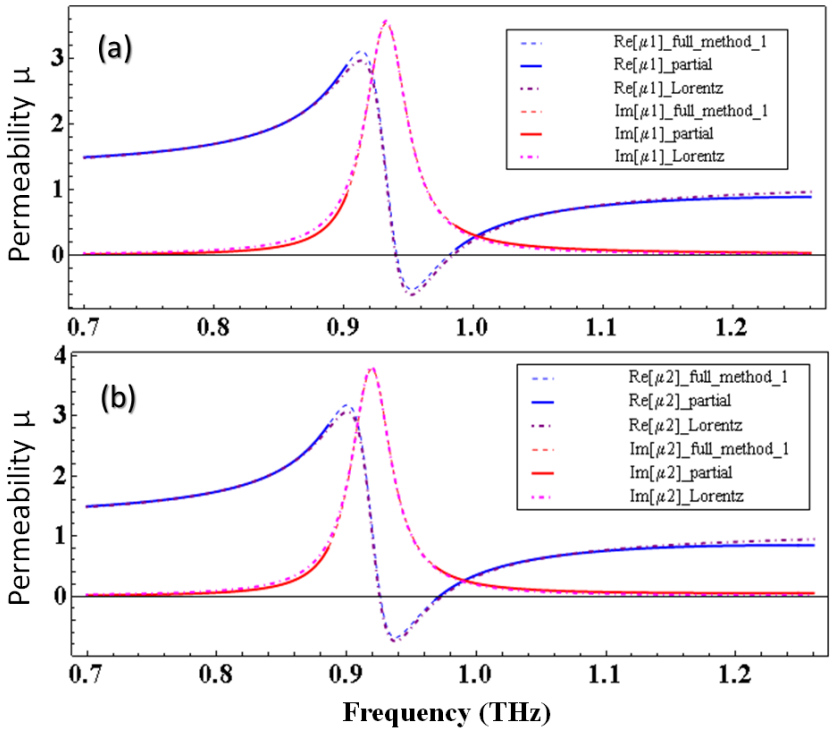

Figure 2.9. Effective permeability μ_{eff} of the (a) single and (b) two-cell MMs slabs retrieved by different methods.

The effective refractive index n_{eff} and impedance z_{eff} retrieved by (2.30) and (2.31) and μ_{eff} and ε_{eff} from dispersion models are plotted in Figure 2.10 and Figure 2.11, respectively, along with the other proposed methods. Blue lines represent the real components and red lines represent the imaginary components. Solid lines represent the values retrieved by the partial retrieval method, and dashed lines represent the values obtained by the full retrieval methods.

It can be observed that negative refractive index occurs not only at the frequencies where ε_{eff}' and μ_{eff}' are both negative, and the n_{eff} retrieved by the different methods agree closely at most frequencies, as does z_{eff}. A noticeable discrepancy between the first full retrieval method and the second full retrieval method occurs at the resonant frequency zone because the second method eliminates the negative ε_{eff}'' in this frequency range.

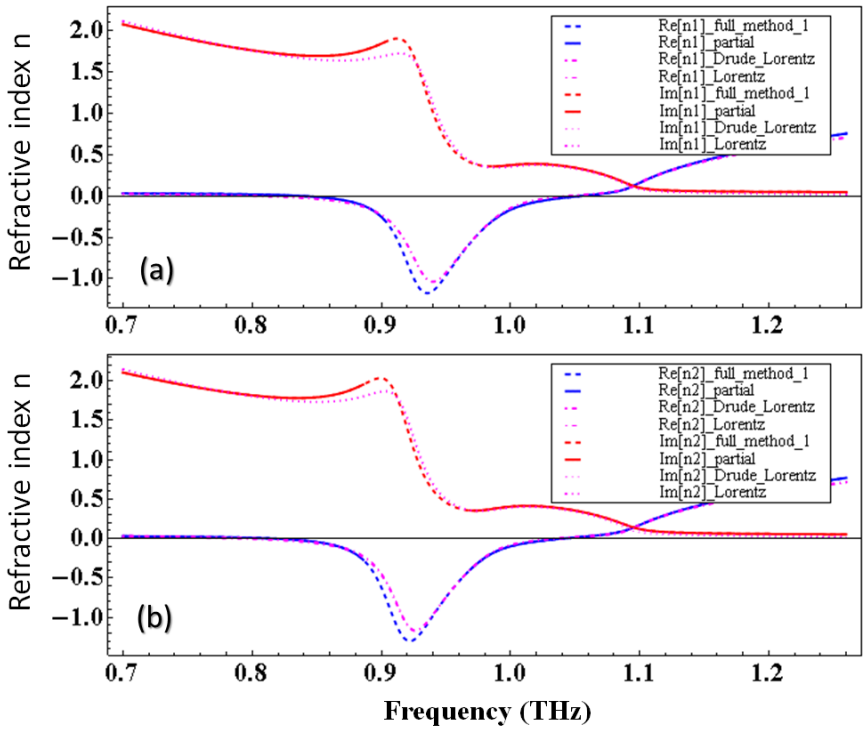

Figure 2.10. Effective refractive indices n_{eff} of the single (a) and two-cell (b) MM slabs retrieved by different methods.

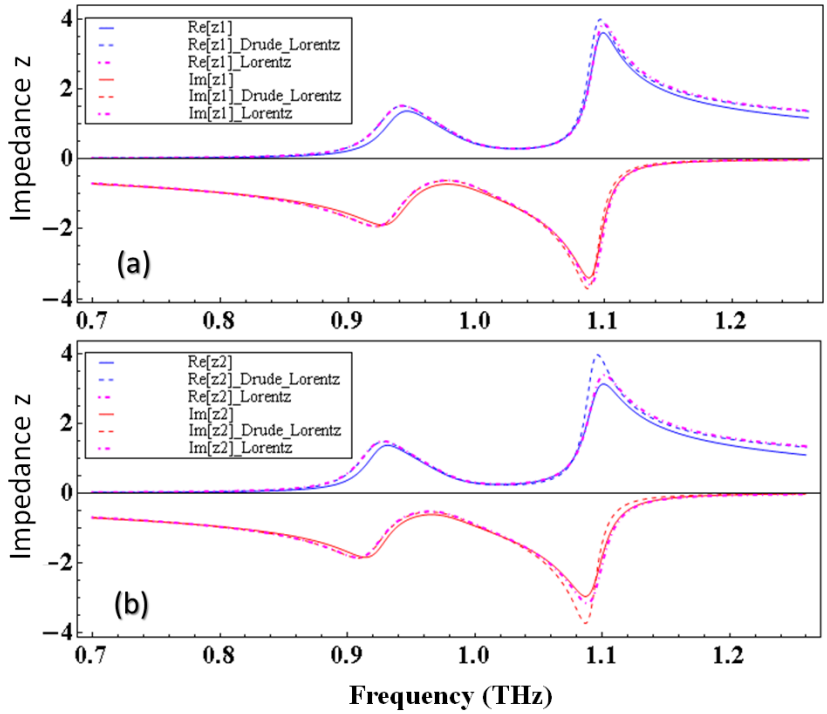

Figure 2.11. Effective impedances z_{eff} of the (a) single cell and (b) two-cell MMs slab retrieved by different methods.

2.3.3 *Equations to Retrieve S-parameters from ε and μ*

The retrieved S-parameters can be calculated using (2.3) and (2.4) with constitutive parameters n_{eff} and z_{eff} retrieved by the aforementioned methods and effective boundary thickness $d = L1_a + L_m + L2_a$, determined in Section II B. Notice that the reference planes of the retrieved S-parameters are set at the effective boundaries. In order to compare the retrieved S-parameters with one obtained by the 3D simulation measured at original reference planes (set at port 1 and port 2, as shown in Figure 2.1), we need to use (2.17) with $(L1_a, L2_a)$ equal to positive $(L1_s, L2_s)$ to shift the reference planes of the retrieved S-parameters outward to the same locations as used in the simulation. From the results shown in Figure 2.12, it can be observed that the S-parameters retrieved by the partial and the first full retrieval method in Section 2.2 agree exactly with original S-parameters at all frequencies while the S-parameters retrieved by the second method agree very well at most of frequencies, but are slightly shifted at resonant frequency band. In other words, the first full retrieval method can extract the exact values for the material properties and constitutive parameters that can be used in (2.30), (2.31), (2.3) and (2.4) to get the same values of original S-parameters, while the second method cannot. The difference between these two methods is the ability to retrieve negative imaginary components of permittivity or permeability, with the results of the comparison to the simulation demonstrating the first full retrieval method works and has greater accuracy than the second method.

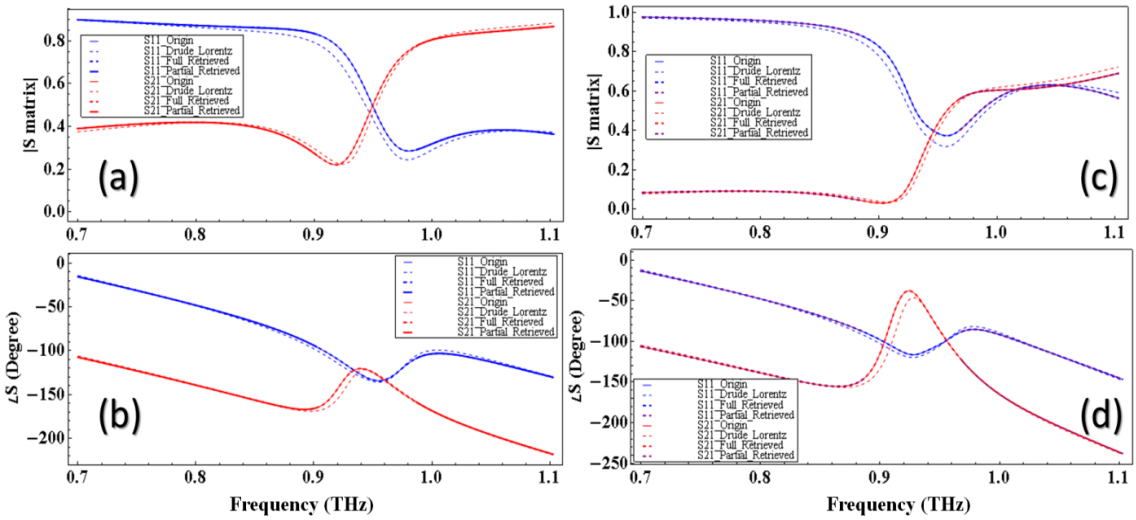

Figure 2.12. The magnitude and phase of S-parameters for the (a,b) single and (c,d) two-cell MMs slabs retrieved by different methods along with the original S-parameters.

2.3.4 *Discussion of Anti-resonant Zone*

The anti-resonant zone is defined as the frequency band where the imaginary part of the permittivity ε'' and μ'' have different signs and seem to violate the lossy and passive material requirements, $\varepsilon'' \geq 0$ and $\mu'' \geq 0$. This phenomenon is illustrated in several papers [66, 67] as a violation of effective medium theory since the wavelength is comparable to (or smaller than) the unit cell size of the metamaterials, so that the MMs can no longer be considered as homogeneous materials in that frequency band. However, we observe that the anti-resonant zone may not have the largest absolute value n' among all retrieved data at frequencies of interest as shown in Figure 2.13 and Figure 2.14, which means that the smallest wavelength among all interesting frequencies is still big enough compared to the unit cell size and the maximum refractive index can be retrieved at this frequency. Examining the max refractive index of material allowed at the resonant frequency provides another piece of evidence suggesting that all wavelengths are large enough to support of effective medium theory [65]:

$$|n'_{Max}| \leq \frac{c_0}{2\, f_0\, L_{cell}} \tag{2.32}$$

where f_0 is the resonant frequency, L_{cell} the unit cell size in the direction of wave propagation, and c_0 is the speed of light in free space. For the SRR-rod metamaterial in this discussion, $L_{cell} = 50\ \mu m$ and $|n'_{Max}|$ at resonant frequency (0.95 THz) is 3.16, larger than any retrieved refractive index.

As shown in Figure 2.13, anti-resonant zone can be reduced as the reference planes are shifted outward from the metamaterial slab. For the SRR-Rod model 1 with reference planes set at the effective boundaries where single cell and 2-cell SRR-Rod metamaterial slabs have the minimum impedance difference, the anti-resonant zone covers most parts of the resonant band. However, for the SRR-Rod model 2, with reference planes set at effective boundaries, anti-resonant zone does not even exist in the whole resonant band.

In conclusion, a unit cell of the metamaterial with narrower width of the rod will have smaller EM wave coupling between SRRs and rods, and the anti-resonance in electric permittivity is weaker.

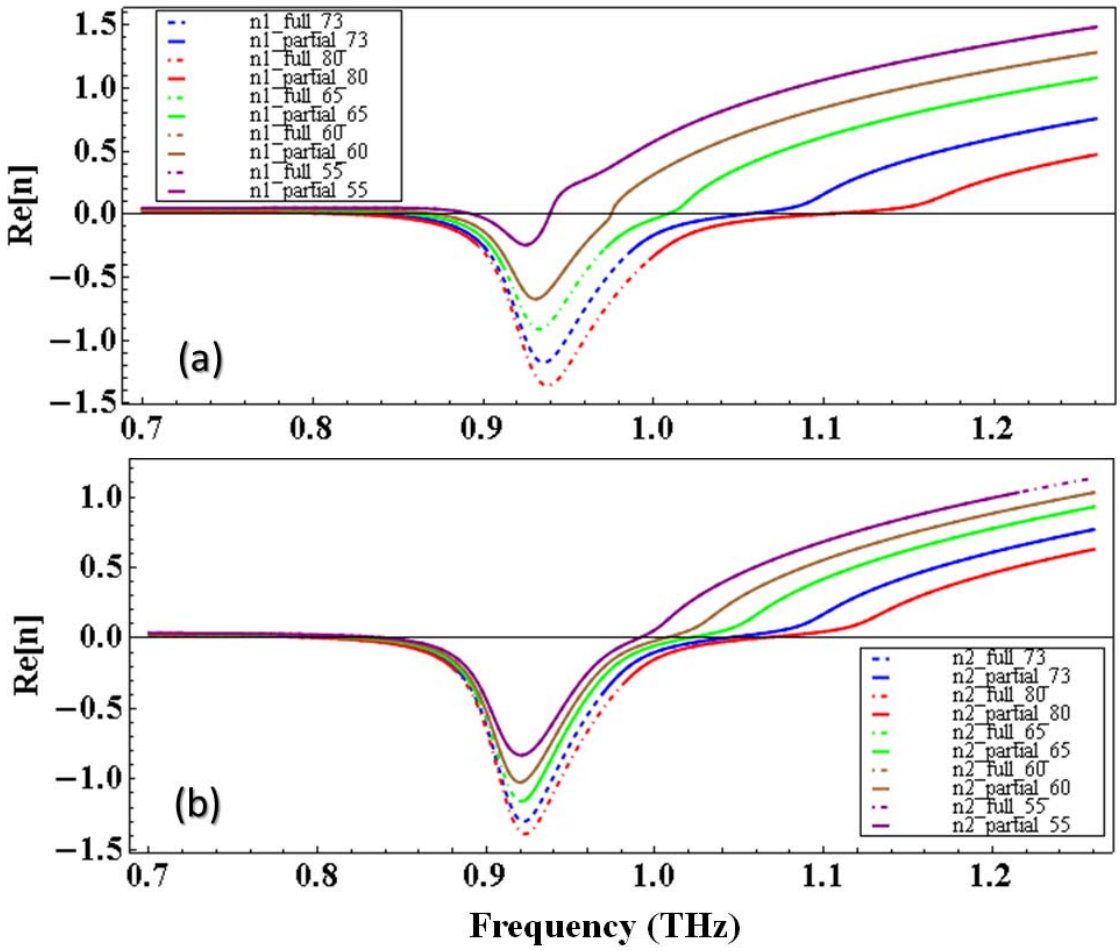

Figure 2.13. Real parts of refractive indices of the (a) single and (b) two-cell MMs slabs retrieved by different methods at different boundaries.

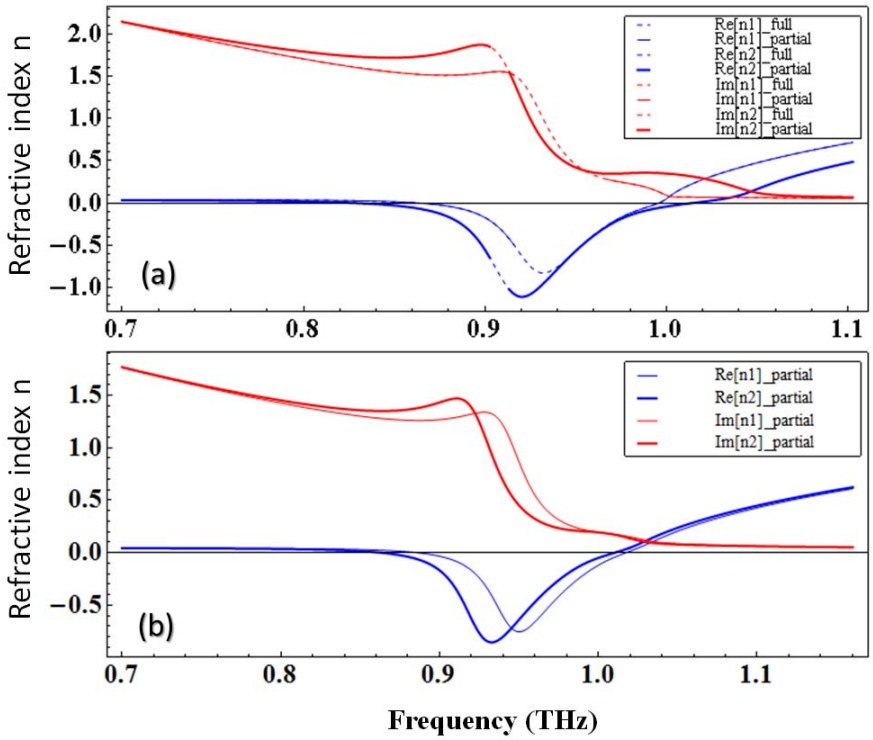

Figure 2.14. (a) n of single and two-cell SRR-Rod Model 1 retrieved by different methods at effective boundaries set at reference planes shifted $L1_s = L2_s = -63\ \mu m$ inward. (b) n of single and two-cell SRR-Rod Model 2 retrieved by different methods at effective boundaries set at reference planes shifted $L1_s = L2_s = -73\ \mu m$.

2.4 Derivations of Equations of Refractive Index and Impedance for Single-Layered Asymmetric Metamaterials

There are certain situations where the proposed method would fail, such as when the metamaterial slab is asymmetric along the wave propagation direction, or when the slab is not mounted exactly in the middle of two measurement ports (as shown in Figure 2.15). For a plane incident wave impinging on the MM slab from port 1, the reflected and transmitted waves will not be the same as the plane incident wave impinging from port 2, i.e., $S_{11} \neq S_{22}$ and $S_{21} \neq S_{12}$.

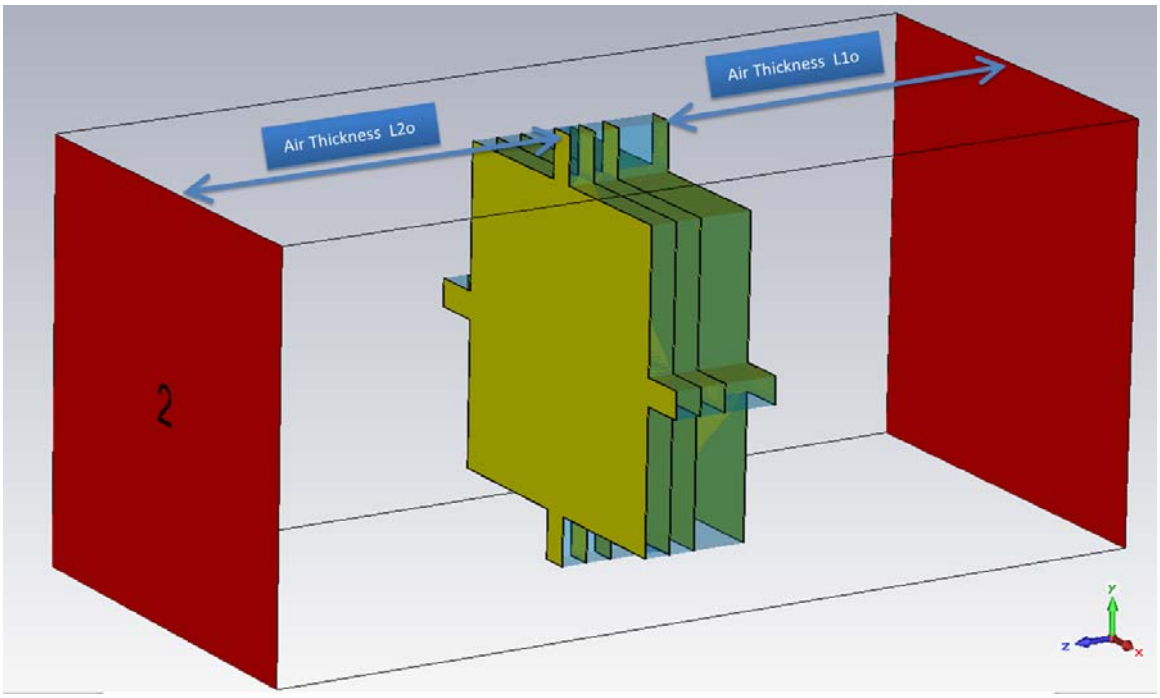

Figure 2.15. Asymmetric fishnet metamaterial slab is not placed in the middle position between the two measurement ports, i.e. $L1_o \neq L2_o$.

To solve this problem, the new equations to retrieve the refractive index and impedance from all S-parameters are required. Conventionally, it is assumed that S_{11} is equal to S_{22} and S_{21} is equal to S_{12} if the slab is located exactly in the middle of two measuring ports in the derivation of (2.6) and (2.7). However, in real measurements, the assumption of equal travelling distance from slab surfaces to each port is not guaranteed and the slab is not always designed to be symmetric in the transverse plane of a wave. For general cases, the refractive index and normalized impedance derived from (2.1) and (2.5) should be

$$n = \frac{\pm 1}{k_0 d}\left(\cos^{-1}\frac{(1+S_{11})(1-S_{22})+S_{21}S_{12}}{2\,S_{21}} + 2\,\pi\,m\right) \tag{2.33}$$

$$z = \pm\sqrt{\frac{(1+S_{11})(1+S_{22})-S_{21}S_{12}}{(1-S_{11})(1-S_{22})-S_{21}S_{12}}}\,. \tag{2.34}$$

By following the procedures mentioned in Section 2.2.3 and considering a L_m thick slab surrounded by air with reference planes set at $(L1_a, L2_a)$, where $L1_a = L1_o + L1_s > 0$

and $L2_a = L2_o + L2_s > 0$, the effective refractive index and normalized impedance equations at any references planes, considering all S-parameters, can be derived as:

$$n_e = \frac{\pm 1}{k_0 d}\left(\cos^{-1}\frac{-\mathrm{j}(\mathrm{S1(L)}(-S_{11}S_{22}+S_{12}S_{21}-1)+(S_{11}+S_{22})\mathrm{S2(L)})+\mathrm{C1(L)}(-S_{11}S_{22}+S_{12}S_{21}+1)+(S_{11}-S_{22})\mathrm{C2(L)}}{2\,S_{21}} + 2\,\pi\,m\right) \quad (2.35)$$

$$z_e = \pm j\sqrt{\frac{-j((S_{11}S_{22}-S_{12}S_{21}-1)\mathrm{S1(L)}+(S_{11}-S_{22})\mathrm{S2(L)})+(S_{11}S_{22}-S_{12}S_{21}+1)\mathrm{C1(L)}+(S_{11}+S_{22})\mathrm{C2(L)}}{j((S_{11}S_{22}-S_{12}S_{21}-1)\mathrm{S1(L)}-(S_{11}-S_{22})\mathrm{S2(L)})-(S_{11}S_{22}-S_{12}S_{21}+1)\mathrm{C1(L)}+(S_{11}+S_{22})\mathrm{C2(L)}}} \quad (2.36)$$

where $\mathrm{S1(L)} = sin(k_0(L1_a + L2_a))$, $\mathrm{S2(L)} = sin(k_0(L1_a - L2_a))$,

$\mathrm{C1(L)} = cos(k_0(L1_a + L2_a))$, and $\mathrm{C2(L)} = cos(k_0(L1_a - L2_a))$.

A fishnet metamaterial slab shown in Figure 2.16 is simulated by CST studio simulation software and the results are utilized to verify and compare the new derived equations, (2.33)-(2.36), with the conventional ones, (2.6) and (2.7). The dielectric sandwiched between the two fishnet-shape gold conductors has $\varepsilon_r = 2.25$ and the unit cell of the fishnet metamaterial slab has a square lattice size $c = 150\,\mu m$, square conductive pad length $d = 104\,\mu m$, and $e = 10\,\mu m$. The slab thickness is the thickness of dielectric layer $t_s = 9\,\mu m$ plus the thickness of two conductive layers $2t_c = 0.8\,\mu m$.

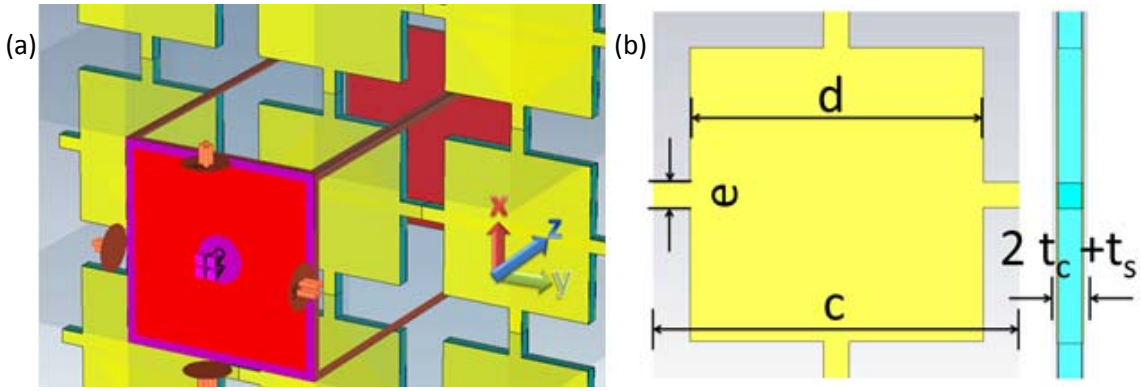

Figure 2.16. (a) A single-layered fishnet MM slab with dielectric sandwiched between the top and bottom fishnet-shaped conductors, (b) Geometry of a fishnet MM unit cell with the slab thickness $L_m = 2\,t_c + t_s$

Considering the case where a plane wave propagates and impinges normal to the symmetric fishnet MM slab's surface in the x-y plane and the S-parameters are measured with ports set equidistant from the slab/air interfaces in the $\hat{z}$ direction, i.e., $L1_0 = L2_0 = 75\,\mu m$, the retrieved effective refractive indices by proposed methods with both the

conventional and newly derived equations are the same and continuous as expected for $S_{11} = S_{22}$ and $S_{21} = S_{12}$. As shown in Figure 2.17, the red lines represent the data retrieved by the proposed partial retrieval method and the blue lines represent the data retrieved by the proposed full retrieval method. It is worth mentioning that discontinuity can be seen in the Im$[z]$ when using $z' \geq 0$ in determination of z'' as shown in Figure 2.18. Zm1p (positive sign) and Zm1n (negative sign) are the impedances calculated from equation (2.34). Zm1t is the impedance with discontinuous z'' determined by $z' \geq 0$. Zm1final is the final determined impedance with continuous z'', which is applied the rule, $\left|e^{-jk_0nd}\right| \leq 1$.

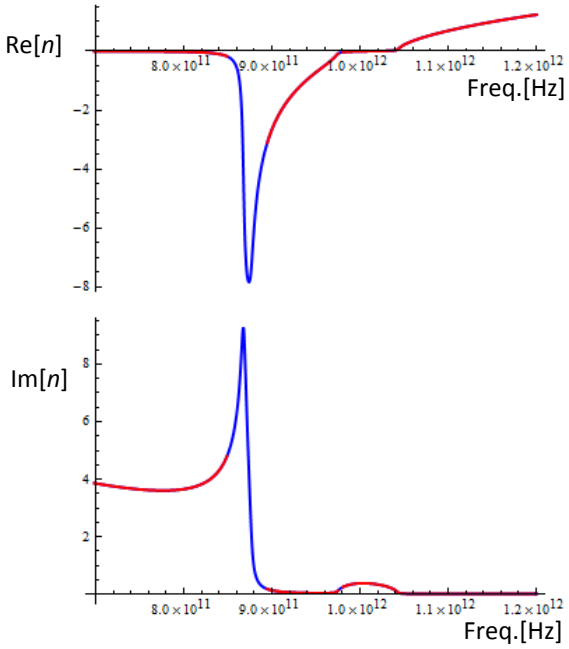

Figure 2.17. Retrieved refractive index of a symmetric single-layered fishnet MM slab with equal distances to the measurement ports from slab/air interface in the x-y plane

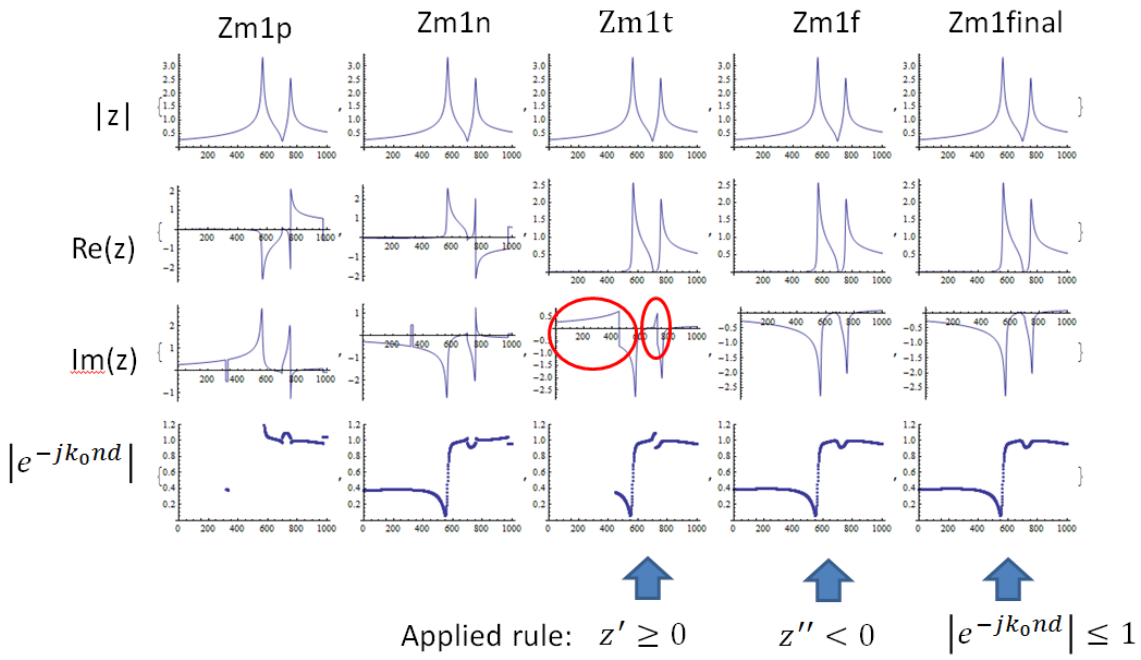

Figure 2.18. Retrieved normalized impedances with different applied rules

Considering the case that a plane wave propagates and impinges on the same fishnet metamaterial slab, but the slab is not placed in the middle of two measurement ports, (i.e., $L1_o = 75\ \mu m, L2_o = 79\ \mu m$) the retrieved effective refractive indices by proposed methods using conventional equations are discontinuous as shown in Figure 2.19 (a). However, the retrieved effective refractive indices by proposed methods using new derived equations are continuous as shown in

Figure 2.19 (b). The reason why the conventional equations fail is due to the lack of considering $S_{11} \neq S_{22}$, $S_{21} \neq S_{12}$. Comparing the results from Figure 2.17 and Figure 2.19 (b), we can see that the retrieved refractive indices are the same since the inspected slab is the same one despite the different locations of the measurement ports.

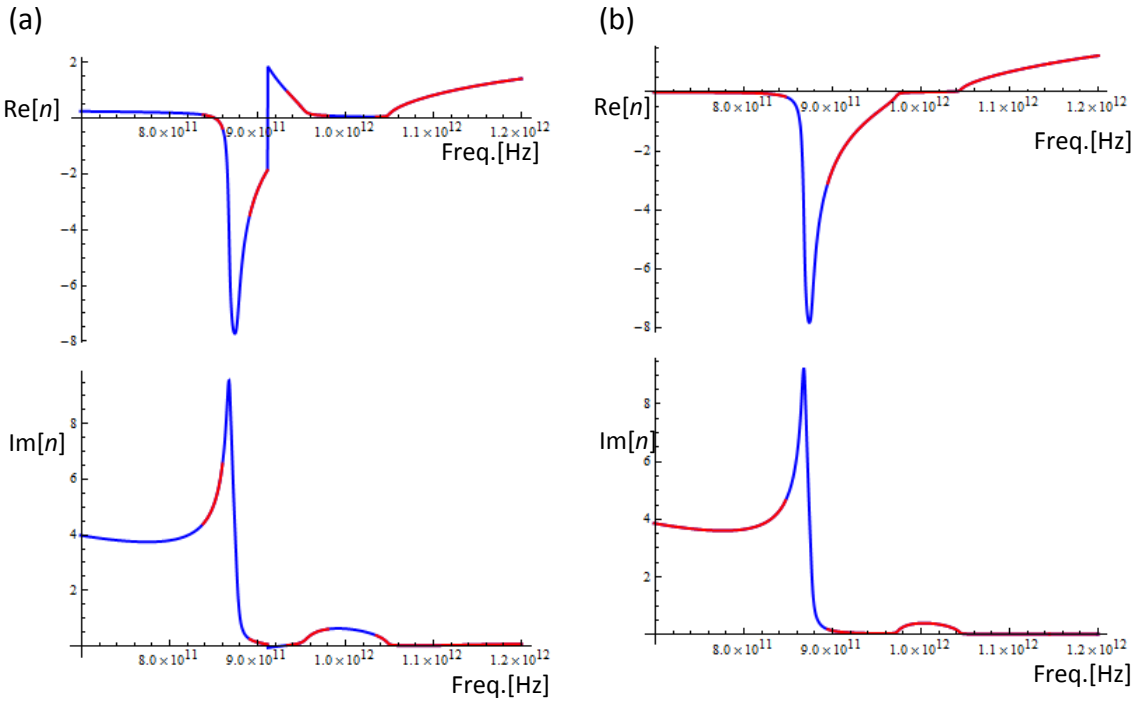

Figure 2.19. (a) Discontinuous retrieved refractive indices of a symmetric single-layered fishnet MM slab using conventional equations. (b) Continuous retrieved refractive indices of the same MM slab using the new derived equations.

2.5 Methods for Multilayered Fishnet Metamaterials

It is interesting that the aforementioned methods, including partial and full retrieval methods, can extract material properties and constitutive parameters from single- or multi-layered SRR-rod and single-layered fishnet metamaterials very well, but not from the multi-layered fishnet metamaterials as shown in Table 2.2. More precisely, the previous methods are functional for the metamaterials whose electrodes or conductors of the unit cell will not have extra coupling effects with the conductors from other layers to create extra resonant modes near the original resonant frequency of the single-layered MMs. The coupling effect is also reported by Liu in [69]; however, there are no detailed procedures describing how to retrieve those material properties, and his reported refractive indices and constitutive parameters are not correct. By observing the refractive

index curves of fishnet metamaterials with three and four conductive layers in his paper, the value of Re[n] at 200 THz is changed from -3.5 to 3. This phenomenon does not happen when an extra conductive layer is added to fishnet MMs with two or four layers. Also, discontinuous curves can be seen in Liu's plots.

In this section, patch algorithms are introduced to modify the previous methods and can successfully extract continuous material properties and constitutive parameters of single-layered and multilayered metamaterials with coupling effects between different conductive layers occurring near the original resonant frequency. The results can be verified by observing forward/backward travelling waves for positive/negative refractive indices at different frequencies in 3D CST simulation software.

Table 2.2 Retrieval methods capability for different metamaterials

	Single-layered SRR-Rod MMs	Multi-layered SRR-Rod MMs	Single-layered & Multi-layered SRR-Rod MMs $S_{11} \neq S_{22}$	Single-layered Fishnet MMs	Single-layered Fishnet MMs $S_{11} \neq S_{22}$	Multi-layered Fishnet MMS	Multi-layered Fishnet MMs $S_{11} \neq S_{22}$
Partial retrieval method	✓	✓	×	✓	×	×	×
Full retrieval method	✓	✓	×	✓	×	×	×
Model-based method	✓	✓	×	✓	×	×	×
Partial retrieval method with new equations	✓	✓	✓	✓	✓	×	×
Full retrieval method with new equations	✓	✓	✓	✓	✓	×	×
Algorithm-based retrieval methods	✓	✓	✓	✓	✓	✓	✓
Coupling effect between layers	×	×	×	×	×	✓	✓

2.5.1 *Coupling Effect Problems with Multilayered Metamaterials*

It is apparent that when a dielectric layer is sandwiched between two conductive layers, there will be a resonant mode due to the capacitance and inductance created by the structure. When a third conductive layer is added, extra resonant modes, due to the coupling effects between 1st - 3rd and 2nd - 3rd conductive layers will appear and the resonant frequencies, $\omega_c = \frac{1}{\sqrt{LC}}$, will depend on the induced inductance and capacitance, i.e., the dielectric constant, surface area, and the distance between conductors. In order to see the impact of the coupling effect in multilayered SRR-Rod and fishnet metamaterial slabs, the SRR-Rod MM model described in Section 2.2.1 is adopted, along with a fishnet MM model based on the one in Section 2.4, slightly modified with 4 μm thick polyimide layer outside the two gold conductive layers of the fishnet unit cell. The SRR-rod and fishnet MMs are stacked in the wave propagation direction for multilayered MM slabs as shown in Table 2.3.

The normalized impedances of multilayered SRR-Rod and fishnet MM slabs are calculated by the procedures in Section 2.2 and evaluated at the material boundaries, i.e., $L1_0 = L2_0 = L1_s = L2_s = 75\ \mu m$, as shown in Figure 2.20 and Figure 2.21. Re[z1] - Re[z4] are the curves of real parts of the impedance corresponding to 1-, 2-, 3-, and 4-layered MM slabs, respectively. There are only two peaks that can be observed on each curve in Figure 2.20, meaning that coupling effect is not occurring at the investigated frequencies after extra layers are added to the original unit cell structure. Thus, the method introduced in Section 2.2.2 to find the effective material boundaries can be adopted.

Table 2.3 Unit cells of 1-, 2-, 3-layered SRR-Rod and fishnet metamaterials and 3D plots of 4-layered SRR-Rod and fishnet metamaterial slabs with Floquet boundary conditions

	SRR-Rod MM	Fishnet MM
Single-layered unit cell	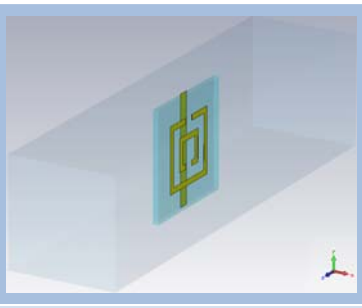	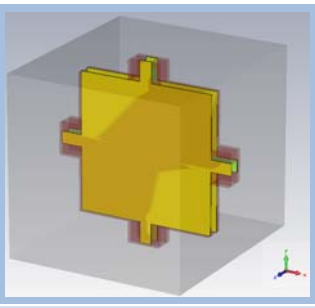
Two-layered unit cell	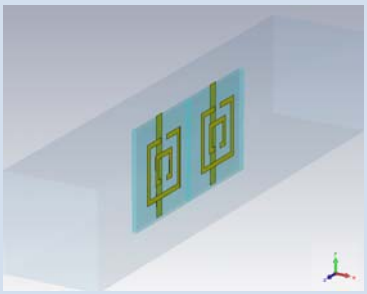	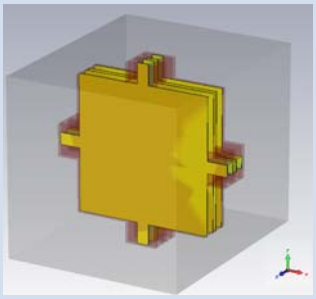
Three-layered unit cell	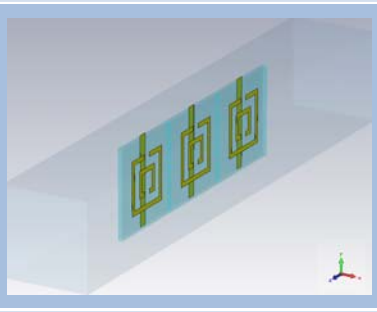	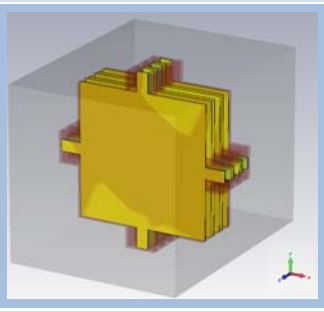
Four-layered MM Slabs with Floquet Boundaries	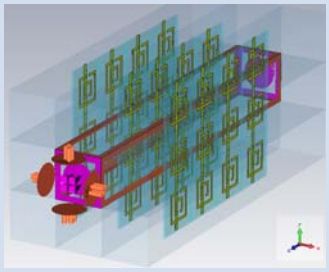	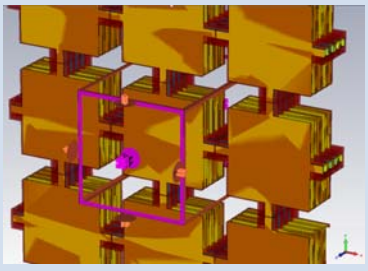

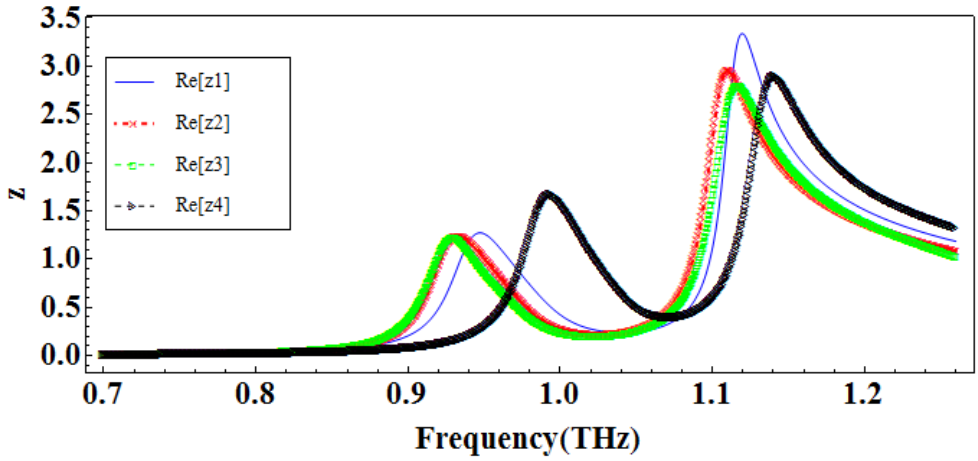

Figure 2.20. The normalized impedances of 1-, 2-, 3-, and 4-layered SRR-Rod MM slabs

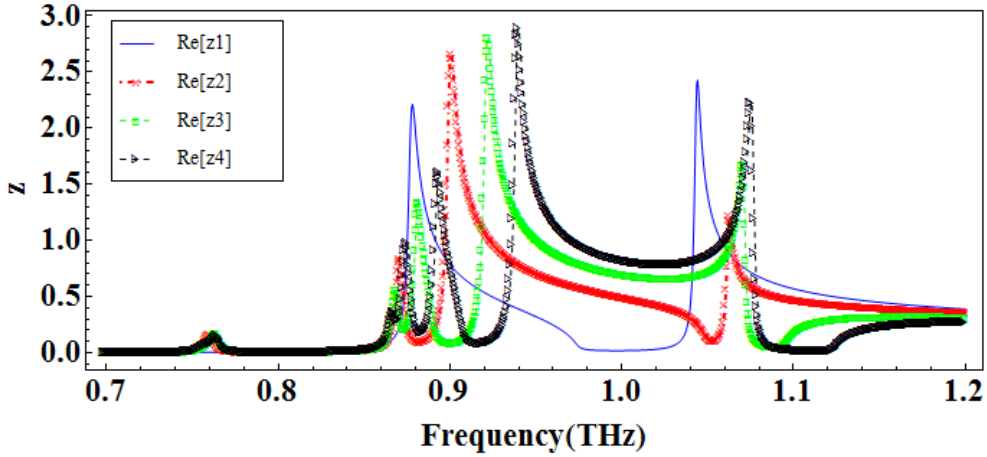

Figure 2.21. The normalized impedances of 1-, 2-, 3-, and 4-layered fishnet MM slabs

However, it is obvious that there are different numbers of peaks to be observed on different curves in Figure 2.21. For example, there are 2 peaks on the single-layered impedance curve, 4 peaks on the 2-layered curve, 5 peaks on the 3-layered curve, and 6 peaks on the 4-layered curve. In other words, extra resonant modes are induced at the investigated frequencies due to the coupling effects of the extra added layers. It is worth noting that the proposed methods to find effective material boundaries should not be applied in this case as there is no meaning to find the boundaries that can minimize the impedance difference of two slabs with different material properties.

Another way to look for the coupling effects is to investigate dramatic changes in the magnitude and phase terms of S_{11} and S_{21}. S-parameters of the multilayered fishnet metamaterial slabs are simulated and plotted in Table 2.4. Red lines represent magnitude and phase of S_{11} and blue lines denote the same for S_{21}. For example, the resonant mode I_a of 1-layered fishnet MM slab can be found at the dip of the $|S_{11}|$ curve corresponding with the phases, $\angle S_{11}$ and $\angle S_{21}$, at the same frequency (0.89 THz) located in the resonant hump zones. For another dip, "mode I_o" of the $|S_{11}|$ curve, only the corresponding phase $\angle S_{11}$ is located in the resonant peak zone but not the $\angle S_{21}$ at the same frequency, 1.06 THz. So, I_o is not a resonant mode of the 1-layered fishnet MM slab. By following the same rule, three resonant modes of the 2-layered fishnet MM slab, II_a, II_b, and II_c, can be found at the dips of the $|S_{11}|$ curve with corresponding phases in the resonant humps. The extra resonant modes, II_b and II_c are introduced by the coupling effects between the original layer and the added layer of fishnet MMs. In order to see these three resonant modes of 2-layered fishnet MM slabs, two different types of fishnet MM slabs are simulated. One is the fishnet MM with PI layers, the other one is the fishnet MM without PI layers. The corresponding E-field and H-field plots are shown in Table 2.5 and Table 2.6, respectively.

Further evidence showing that the retrieved refractive indices and constitutive parameters are not correct in [69] is to observe the wave travelling directions at the resonant mode frequencies in the 3D simulation software. In [69], the refractive indices of multilayered MM slabs with four and five conductive layers at the fundamental resonant "mode a" were claimed to be positive. However, our simulations show backward travelling waves occur at the fundamental "mode a" frequencies of 1-, 2-, 3-, and 4-layered fishnet MM slabs.

Because of the coupling effects, discontinuous refractive indices are extracted from the multilayered fishnet MM slabs by using the previous (unpatched) methods and are illustrated in Figure 2.22. Even though the retrieved results are not correct at all investigated frequencies, we can still see the negative refractive indices at the

fundamental resonant "mode a" of different multi-layered fishnet MM slabs, which agreed with the 3D simulation results.

Table 2.4 S-parameters of 1-, 2-, 3-, and 4-layered fishnet MM slabs obtained from 3D simulation software

	|S11| and |S21|	Phases of S-parameters (rad)
Single-layered	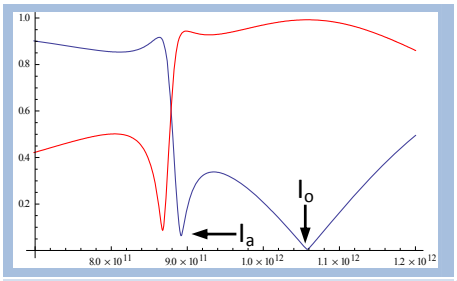	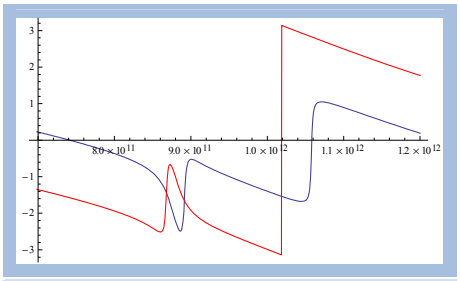
Two-layered	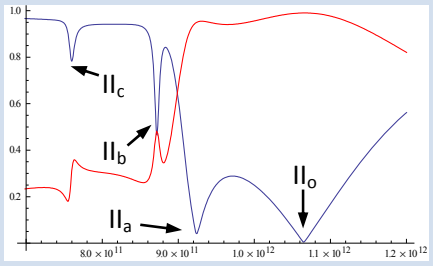	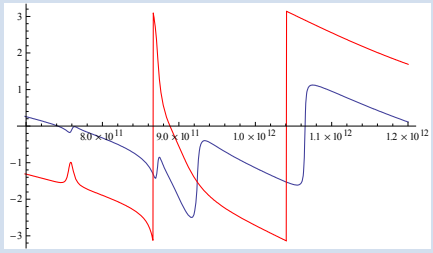
Three-layered	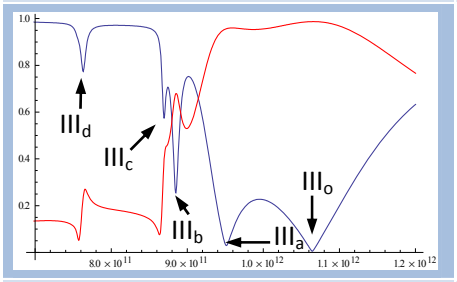	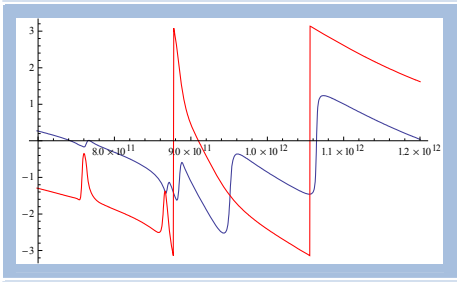
Four-layered	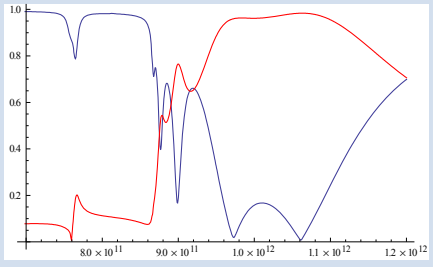	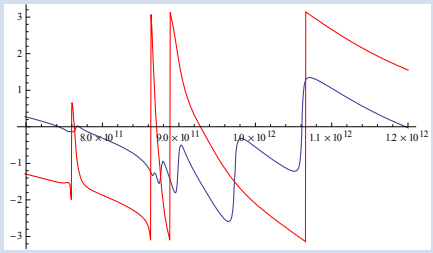

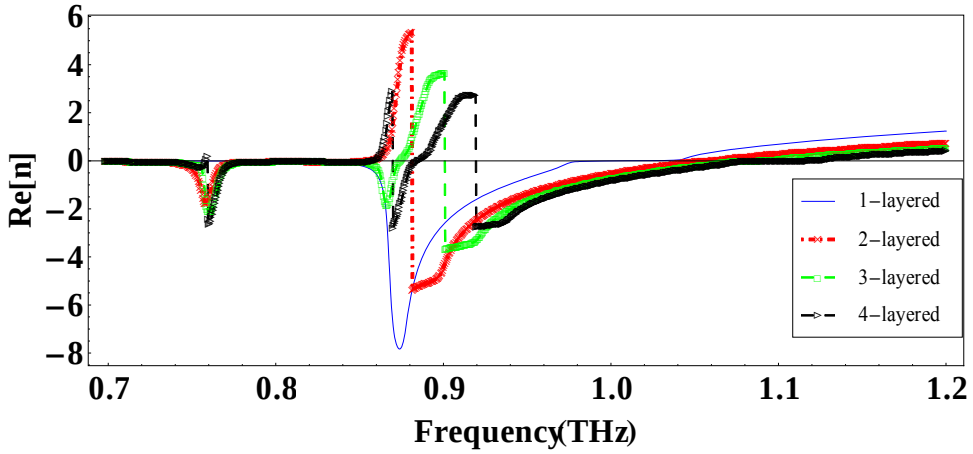

Figure 2.22. Continuous and discontinuous refractive indices of 1-, 2-, 3-, and 4-layered fishnet MM slabs are retrieved by previous unpatched methods.

Mathematically, there are three major classifications of discontinuities, including removable, jump and essential discontinuities [70]. In Figure 2.22, the jump discontinuity can be observed easily. Since material properties are described in complex numbers, the phase terms can also be adopted to distinguish the continuity. A jump discontinuity can be seen on the phase curve of refractive index of the 2-layered fishnet MM slab in Figure 2.23.

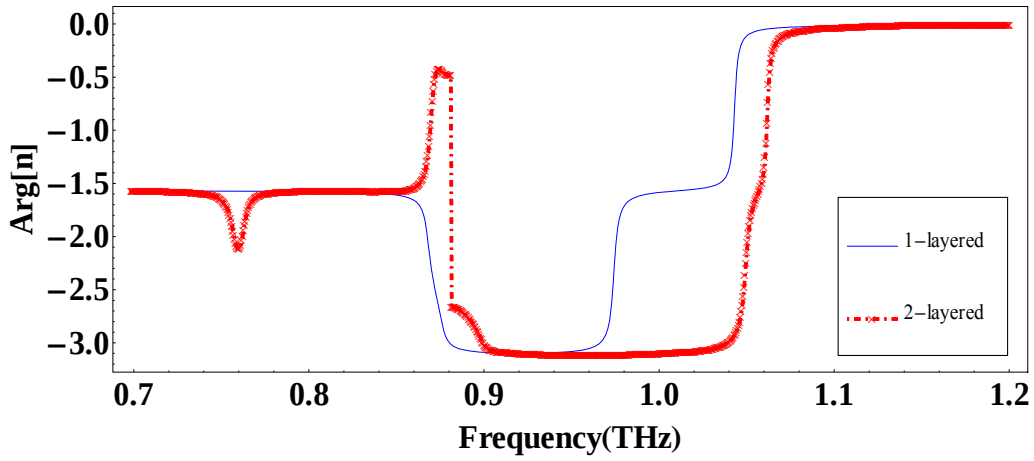

Figure 2.23. Continuous and discontinuous phases of refractive indices of 1- and 2-layered fishnet MM slabs are plotted in the blue and red curves, respectively.

Table 2.5 E-field plots of 2-layered fishnet MM slabs

	Fishnet MM with PI layers	Fishnet MM without PI layers
II_a E-field	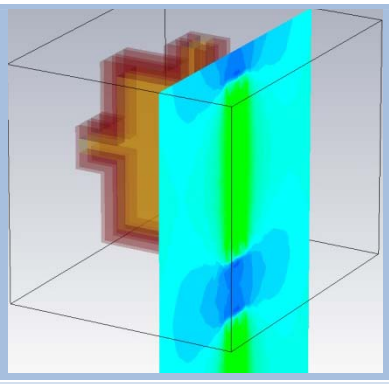	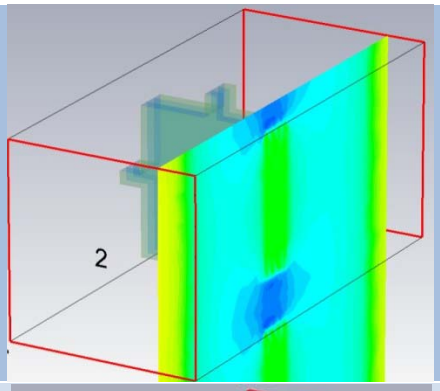
II_b E-field	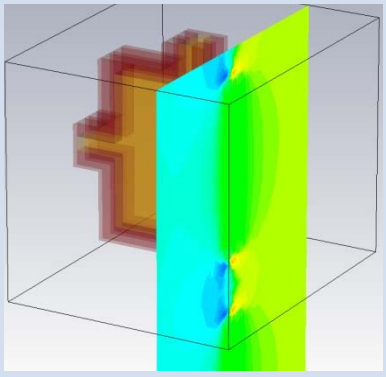	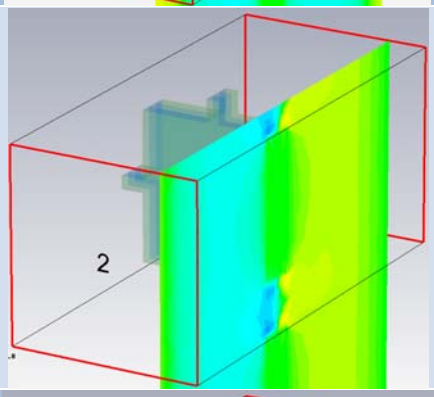
II_c E-field	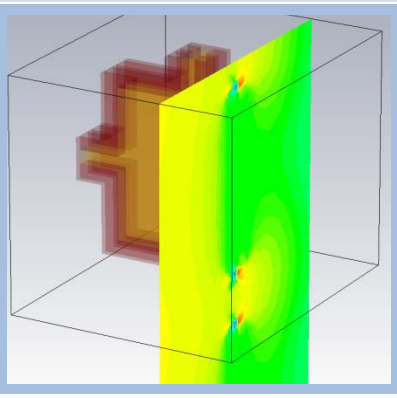	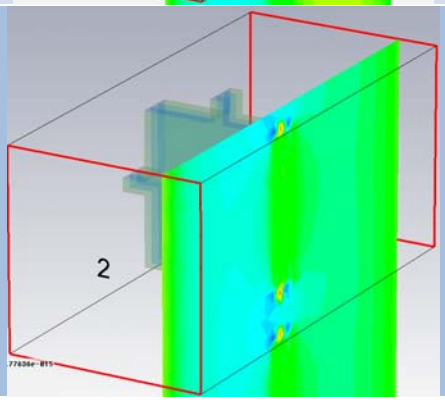

Table 2.6 H-field plots of 2-layered fishnet MM slabs

	Fishnet MM with PI layers	Fishnet MM without PI layers
II_a H-field	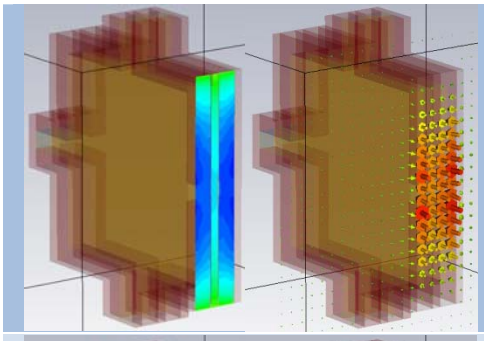	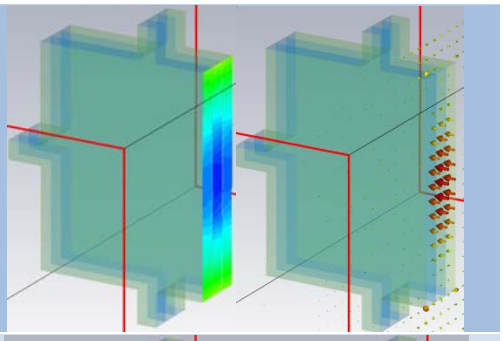
II_b H-field	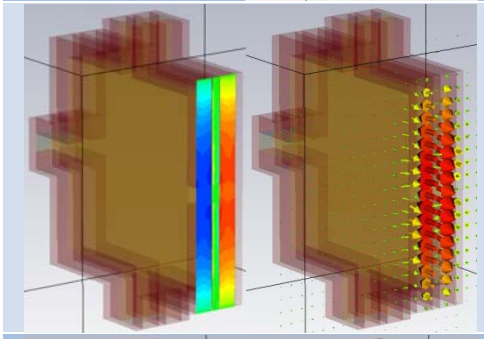	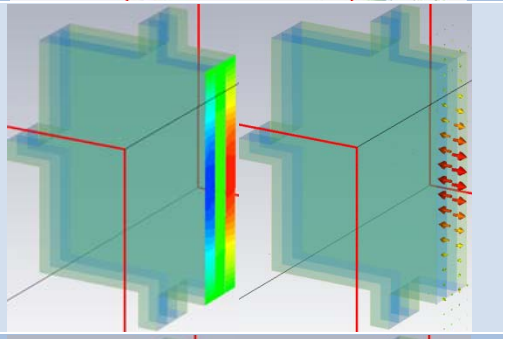
II_c H-field	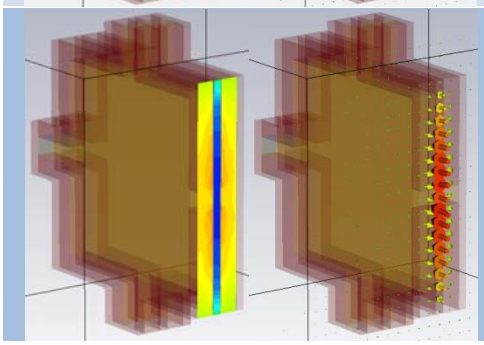	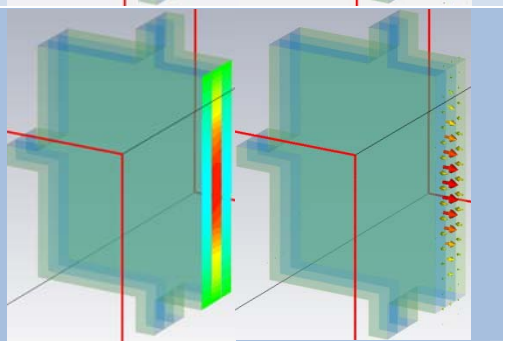

2.5.2 *Reasons for Discontinuities of Retrieved Refractive Indices*

Since the retrieved results in Figure 2.22 are discontinuous, it implies something went wrong in the retrieving procedures. To find out what causes the jump discontinuities of retrieved refractive indices of multilayered MM slabs, the refractive index candidates, n_+ and n_-, and S-parameters, S_{11} and S_{21}, of the single-layered fishnet MM slab are investigated and plotted in Figure 2.24. n_+ and n_- represent the refractive index candidates with the positive and negative sign in the n equation and branch index $m = 0$.

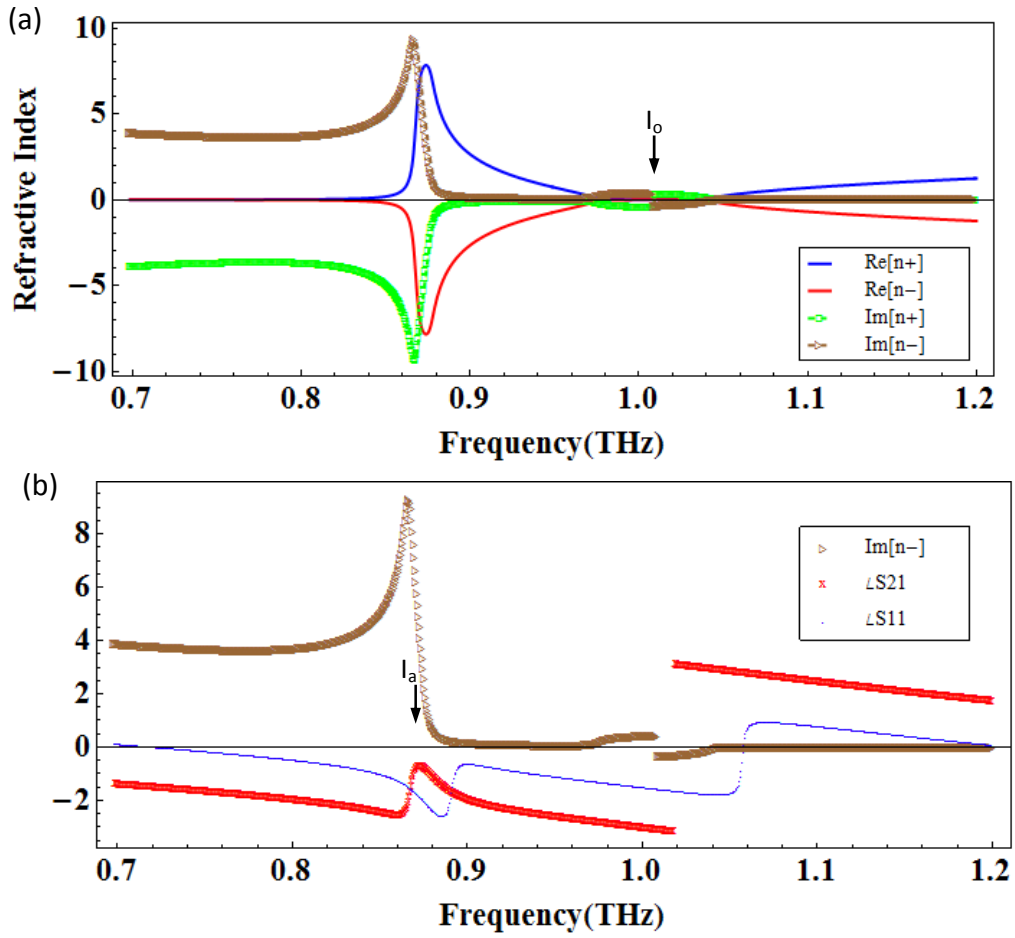

Figure 2.24. (a) Refractive index candidates $n_+$and n_- of 1-layered fishnet MM slab, (b) Im[n_-] and phases of $S_{11}$and S_{21}

In Figure 2.24 (a), there is one jump discontinuity on the curves of imaginary parts of refractive index candidates at the frequency around "mode I_0" (1.01THz), where there is a resonant hump area of $\angle S_{11}$ curve nearby (1.06THz) and a principle angle phase change of $\angle S_{21}$ curve (1.02THz) as shown in Figure 2.24 (b). This jump discontinuity at the frequency around "mode I_0" can be solved by simply applied the rule, $n'' > 0$, mentioned in the previous methods to determine the final continuous result of the refractive index.

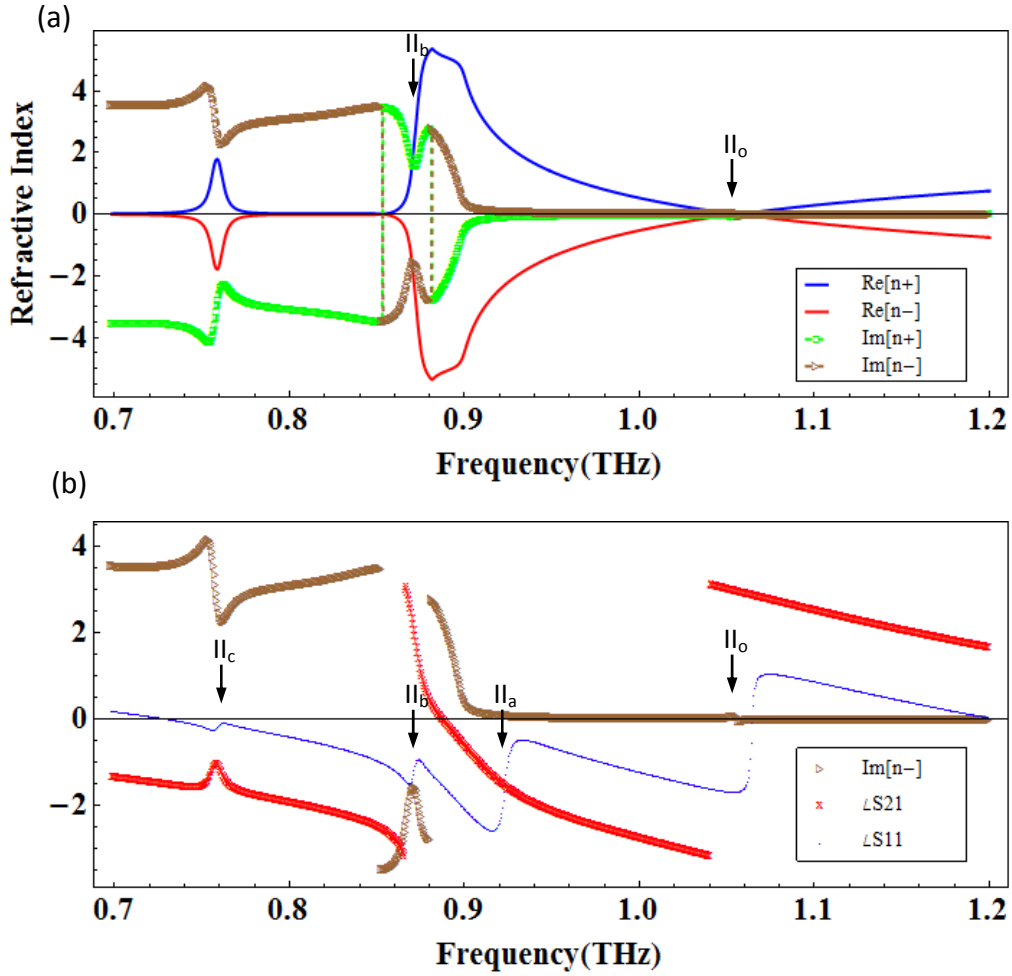

Figure 2.25. (a) Refractive index candidates $n_+$and n_- of 2-layered fishnet MM slab, (b) Im[n_-] and phases of $S_{11}$and S_{21}

There are more than one jump discontinuities observed in Figure 2.25 (a). At the frequency of "mode II_0" (1.06THz), the jump discontinuity on the curve of imaginary parts of refractive index candidate Im[n_-] is the same as the one of 1-layered fishnet MM slab and can be solved by simply applying the rule, $n'' > 0$, mentioned in the previous method. This kind of jump discontinuity happens with a resonant hump occurring on only one phase curve of an S parameter (S_{11} or S_{21}), not in both. However, two more jump

discontinuities can be observed on the same curve around the frequency of "mode II_b" (0.87THz). This kind of jump discontinuity happens with a resonant hump occurring on both phase curves of S-parameters (S_{11} and S_{21}). In other words, this kind of jump discontinuity is due to the coupling effect resonant mode causing phase changes in S-parameters. After using these S-parameters in the refractive index equation, the jump discontinuities can happen naturally due to the phase changes in S-parameters.

2.5.3 *Patch Algorithms*

As shown in Figure 2.25 (a), one resonant mode caused by the coupling effect may create two jump discontinuities, and the values of the curves between the two jump discontinuities have sign changes that cause the wrong determination and a discontinuous result in the final retrieved refractive index.

The first proposed patch algorithm, called the pre-fixing algorithm, is to fix the unwanted jump discontinuities in the refractive index candidates before applying the methods proposed in Section 2.2-2.4 to determine the final refractive index. The algorithm is described as follows:

1. Determine the frequencies of resonant modes and the types of the resonant modes from the dips on the |S11| curve.
2. Associate the modes with the jump discontinuities of the refractive index candidates.
3. Fix the jump discontinuities associated with the resonant modes by changing the signs of values.
4. Follow the methods proposed in Sections 2.2-2.4 to retrieve material properties and constitutive parameters.

The patched and original refractive index candidates are shown in Table 2.7. Only the discontinuities associated with resonant modes are modified. After pre-fixing the refractive index candidates, the continuous refractive indices can be retrieved.

Table 2.7 Patched and unpatched refractive index candidates of different layered fishnet MM slabs

	Unpatched n candidate	Patched n candidate
Single-layered	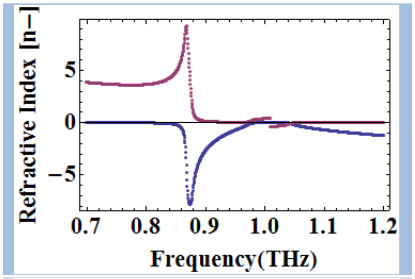	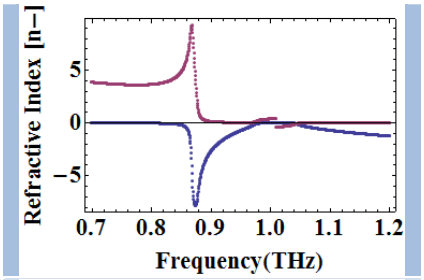
Two-layered	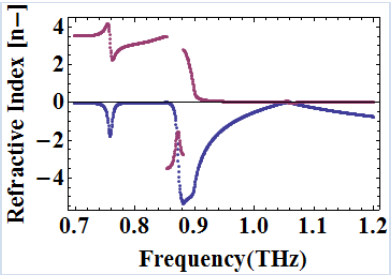	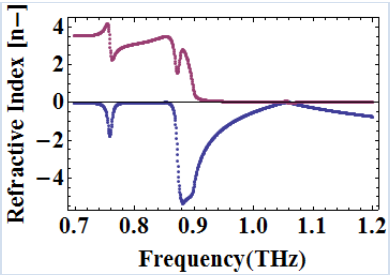
Three-layered	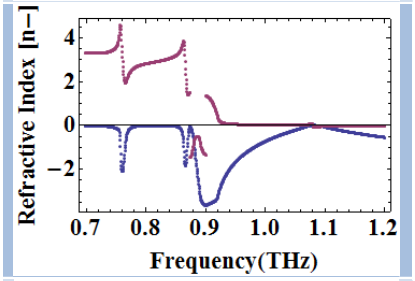	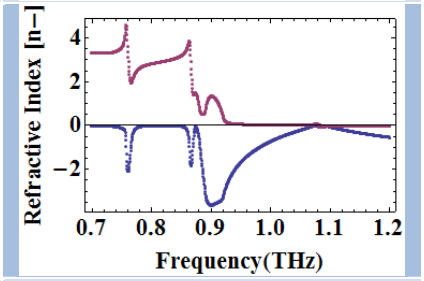
Four-layered	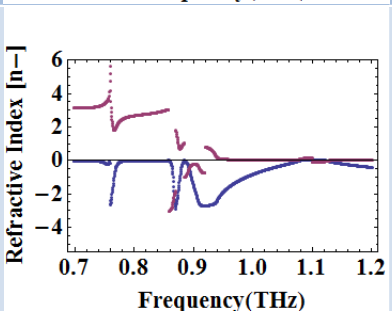	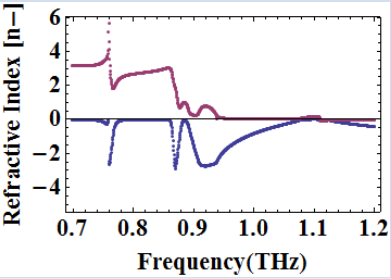

The second patch algorithm is called the ‘iterative fixing algorithm’. It can be used to fix the refractive index candidates and then follow the proposed methods to retrieve material properties. Alternatively, it can be used to fix the incorrect and discontinuous refractive indices retrieved by the previously proposed methods without fixing the refractive index candidates in advance. Since the jump discontinuities in the refractive index candidates can only occur in the resonant mode frequencies, and each resonant mode may come with zero or two jump discontinuities in the refractive index candidates that cause one jump discontinuity in the final retrieved refractive index, we can search for the discontinuities in the resonant band starting from the low resonant mode frequency to high resonant frequency and change the sign of all the following values after the frequency of the discontinuity. The algorithm for fixing the refractive index candidates is implemented as follows:

```
For (f_resonant_low<fi< f_resonant_high or f_last_jump_discontinuity_mode_o )
{
 If jump_ discontinuity [n’’(fi)] is true
 Do
  {
   n’’_new(fi+1)=n’’_origin(fi+1)
   fi=fi+1
  } Until (fi<f_investigation_high or f _last_jump_discontinuity _mode_o)
}
```

The transitions of retrieved refractive indices in the fixing process by the iteratively fixing algorithm are shown in Table 2.8. Blue, red, green and black curves represent the refractive indices of 1-, 2-, 3- and 4-layered fishnet MM slabs, respectively. For 2- and 3-layered fishnet MM slabs, the correct and continuous results can be obtained after two iterations of the algorithm, fixing the jump discontinuity since there are two discontinuities on their refractive index candidates. The original correct value of n after the discontinuity might be changed to the wrong sign after the 1st iteration but it will be

changed back to the correct sign after the 2nd iteration, as expected, because for one resonant mode there can only be zero or two discontinuities.

Table 2.8 The changes of retrieved refractive indices of different layered fishnet MM slabs by the iterative fixing algorithm

	Real parts of Refractive indices
Original discontinuous results	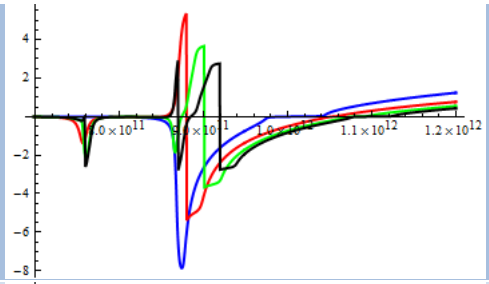
Iteration 1: Fixing 1st jump discontinuity	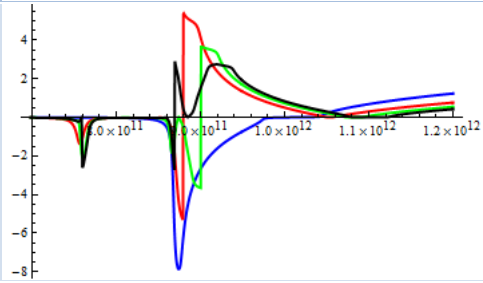
Iteration 2: Fixing 2nd jump discontinuity	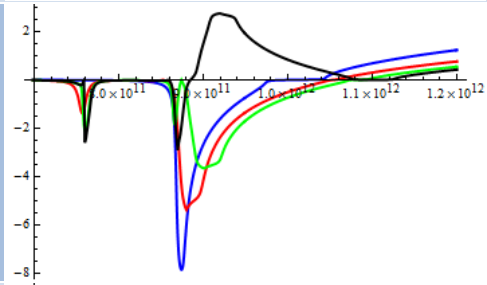
Iteration 3: Fixing 3nd jump discontinuity	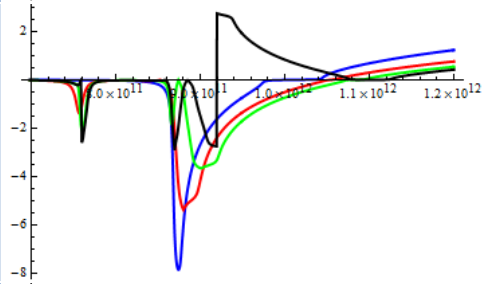
Iteration 4: Fixing 4th jump discontinuity	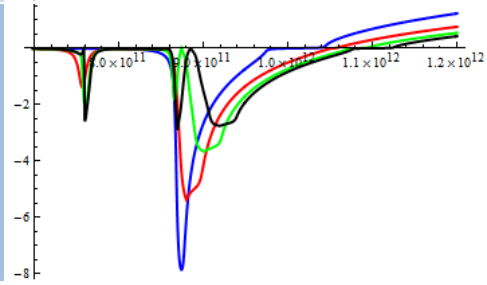

The third proposed patch algorithm is called the post-fixing algorithm. By applying the physical rules and examining the continuity of retrieved results of the effective refractive index, impedance, permittivity and permeability, we can determine which signs of values have to be changed. Since $n''$and z' are already determined by physical rules, we can first plot the phases of n and z to see if either n'or z'' is one to be corrected. Then, we can fix the parts that cause a jump discontinuity of any material properties or constitutive parameters. For example, the phase of the refractive index of 2-layered fishnet MM is discontinuous, as shown in Figure 2.23. It can be seen that n' is one to be corrected. The patched and unpatched n and z can be used to derive ε and μ as shown in Figure 2.26. It can be observed the original sharp rising μ′ at the resonant mode II_a is suppressed by the resonant mode II_b induced by the coupling effect.

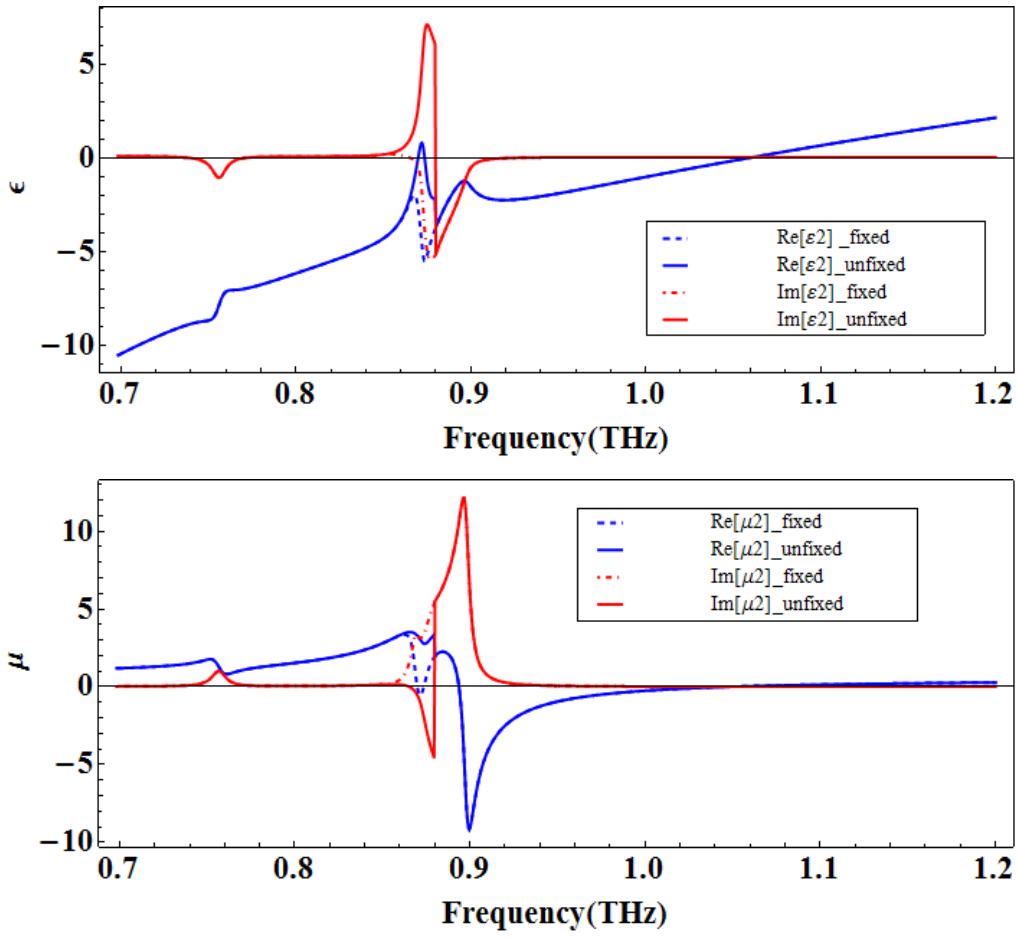

Figure 2.26. Patched and unpatched permittivity curves (a) and permeability curves (b) of 2-layered fishnet MM slab

The figure of merit (FOM) [71] is defined as - n'/n'' to determine the "quality" of negative refraction, i.e. , the number of times that the wave can oscillate inside the metamaterial before being absorbed or dissipated [72]. By feeding the retrieved effective refractive indices into FOM and observing the FOM of multilayered fishnet MM slabs in Figure 2.27, the maximum values of FOM increase with more layers of fishnet metamaterials stacked up in the slab. In this case, the full width at half maximum (FWHM) bandwidth of the FOM for a multilayered fishnet MM slab is wider than the 1-layered fishnet MM slab.

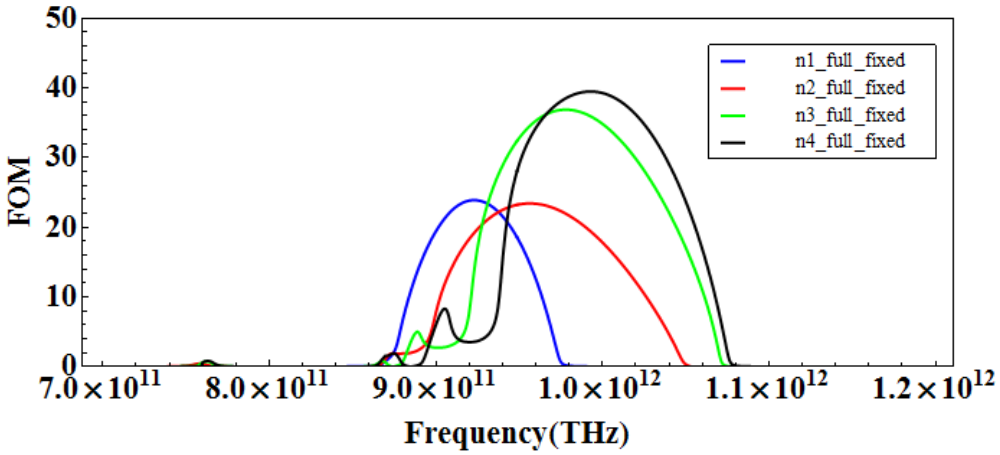

Figure 2.27. The figure of merit (FOM) for 1-, 2-, 3-, and 4-layered fishnet MM slabs

The final retrieved refractive indices of 2-layered fishnet MM slab show the negative n at the resonant modes II_a and II_b while the paper [69] claimed the positive n at the resonant mode II_a and the unpatched methods extracted positive n at the resonant mode II_b. To verify the negative n at the resonant modes II_a and II_b, we use 3D simulation software to observe backward travelling waves and validate the correction of final retrieved results as shown in Table 2.9. In the simulation model, a plane wave is travelling from the front to the back side of a fishnet MM slab and a backward travelling wave can be observed around the fishnet slab travelling anti-parallel to the incident wave.

Table 2.9 Backward travelling waves observed by 2D E field plots at the resonant modes II_a and II_b with phase variations from 0 to 180 degree

	∠0°	∠30°	∠60°	∠90°	∠120°	∠150°	∠180°
E field at mode II_a	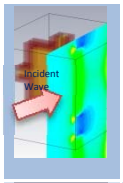	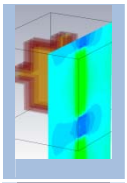	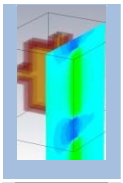	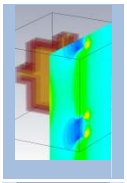	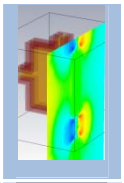	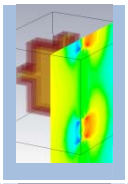	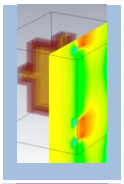
E field at mode II_b	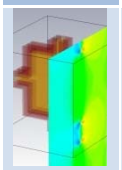	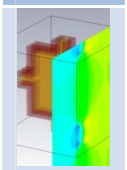	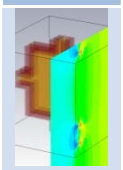	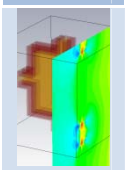	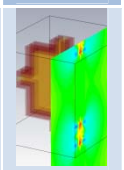	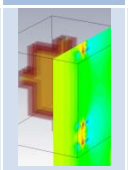	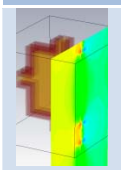

2.6 CONCLUSIONS

In this chapter, improved robust methods were proposed to fully retrieve effective material properties and parameters of metamaterials based on the material continuity and dispersion models. The first extraction method based on material continuity can retrieve missing properties in anti-resonant zone, where imaginary part of permittivity is negative, from partially retrieved data. The second extraction method can retrieve material parameters of dispersive Drude and Lorentz models by genetic algorithms and optimization methods, and use these models to find effective impedance and refractive index at all frequencies of interest. Imaginary parts of permittivity retrieved by the first method will still be negative in anti-resonant zone, while the imaginary parts of permittivity and permeability retrieved by the second method will always be positive. In addition, improvements in finding effective material boundaries are made by a clearer and better definition on the effective boundary based on a plane incident wave and the homogenous material condition. Moreover, a very efficient algorithm in choosing the correct branch of n' is proposed and can reduce two comparisons in the procedures to one, saving computational time in solving the binominal equation (Eq. 7 in [52]). Equations of effective refractive index and impedance at new reference planes are derived and can be used in examining anti-resonant effect at different boundaries.

Additionally, the equations to fix discontinuous retrieved material properties due to unequal distances from material boundaries to the measurement ports were derived. The effective material properties, such as impedance, refractive index, electric permittivity and magnetic permeability that were obtained by different methods agree very well with each other. The scattering parameters reconstructed from retrieved permittivity and permeability at original reference planes are consistent with the original data obtained from the simulation software, showing the allowance of retrieved negative imaginary parts of permittivity.

Furthermore, extra resonant modes that occur in multilayered fishnet metamaterials due to strong coupling effects between different conductive layers create problems in choosing the correct branch index m of the refractive index and end up with the discontinuous retrieved effective refractive indices. To solve this special issue, several patch algorithms were proposed to successfully retrieve the results of continuous material properties and constitutive parameters. The retrieved negative refractive index can be verified by observing the backward travelling wave inside the material from 3D CST simulation software, i.e., the directions of the phase velocity of the incident wave inside the material is antiparallel to the Poynting vector of the wave.

Although the debate over whether the negative imaginary parts of permittivity or permeability should exist or not still remains, two retrieval methods along with patch algorithms for multilayered strong coupled fishnet metamaterials were proposed for both sides of the discussion. In addition, the anti-resonant zone can be reduced by shifting the reference planes outward from the metamaterial slab or by changing the geometry of the unit cell. Also, the anti-resonant zone may exist at the frequency band where the absolute value of real part of refractive index is not the largest, i.e., the wavelength at the anti-resonant zone is still sufficiently large compared to the MM unit cell size. In other words, the assumption of effective medium theory still stands at the anti-resonant zone.

Chapter 3. TUNABLE ACTIVE METAMATERIALS

Passive metamaterials intrinsically can only be operated at certain narrow frequency bands, with electric and magnetic resonant frequencies fixed by the geometry and material properties of the unit cell. In order to fully utilize the potential of metamaterials and dynamically control the material properties in real time, a study of tunable active metamaterials (AMMs) is necessary. This chapter investigates variations in the modulation of THz electromagnetic waves by using different unit cell geometries (Figure 3.1) in periodic structures and different tuning mechanisms, such as changing the material properties of the dielectric or conductive elements of the unit cells.

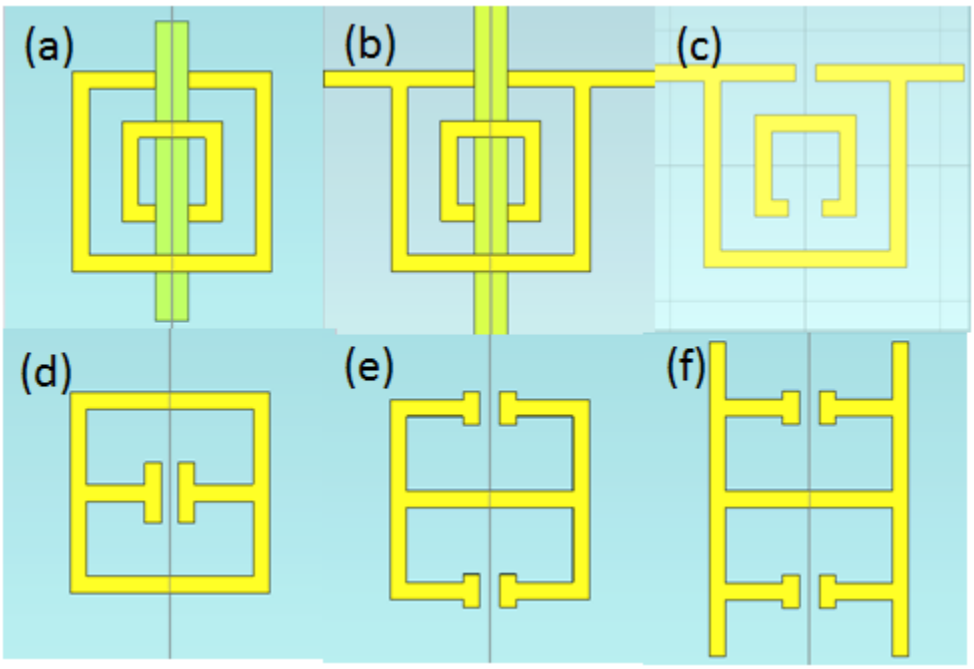

Figure 3.1. Several SRR-based patterns for MM unit cells. (a) typical SRR-Rod unit cell, (b) modified SRR-Rod unit cell, (c) modified SRR unit cell, (d) SRR with one internal gap,(e) SRR with two external gaps, (f) modified SRR with external gaps in two axial directions.

The SRR-based patterns in Figure 3.1 can either generate negative permittivity, negative permeability, or a double negative effect according to the polarization directions of the incident waves. By combining patterns in a single MM unit cell, for example, patterning SRR with one internal gap, as shown in Figure 3.1(d), on top and bottom surfaces of the unit cell, the resonance can occur for multiple polarization directions. The pattern in Figure 3.1(f) is proposed in order to have negative electric resonant effect in both $\hat{x}$ and $\hat{y}$ directions. The key point for designing these patterns is to generate equivalent lump element models, inductance and capacitance, for electric and/or magnetic resonance in order to create negative permittivity and/or permeability. If a surface current flows along a long conductive strip in a pattern, then the strip can serve as an inductance element. If a surface current flows on the conductive strip with a gap, then the gap can serve as a capacitive element. Further studies on these patterns can help the design of proposed devices for wave manipulation in Chapter 4.

3.1 MECHANICALLY TUNABLE AMM

Assuming that the metamaterial slab is stretchable, we can mechanically modulate an AMM by simply elongating or compressing the metamaterial slab along the transverse or longitudinal direction. In this case, the geometries of both conductive metal and dielectric substrate are modified mechanically. Another way is to manipulate the metallic conductor of metamaterials based on the lateral movement of a Micro-Electro-Mechanical Systems (MEMS) comb drive such that the gap sizes of the split rings or the SRR patterns can be changed as desired. Another kind of structurally tunable MM is achieved by shifting the whole MM layer in the transverse wave direction, while maintaining the geometry of the unit cell. This lateral-shift AMM has been realized in the microwave [73] and THz [74] ranges. Additionally, Tao has demonstrated a structurally tunable MM created by reorienting the SRR direction using MEMS technologies [75].

First, to investigate the effect of gap size change in the unit cells, a typical SRR-Rod metamaterial with a plane incident wave polarized in (Ey, Hx) is used (Figure 3.2).

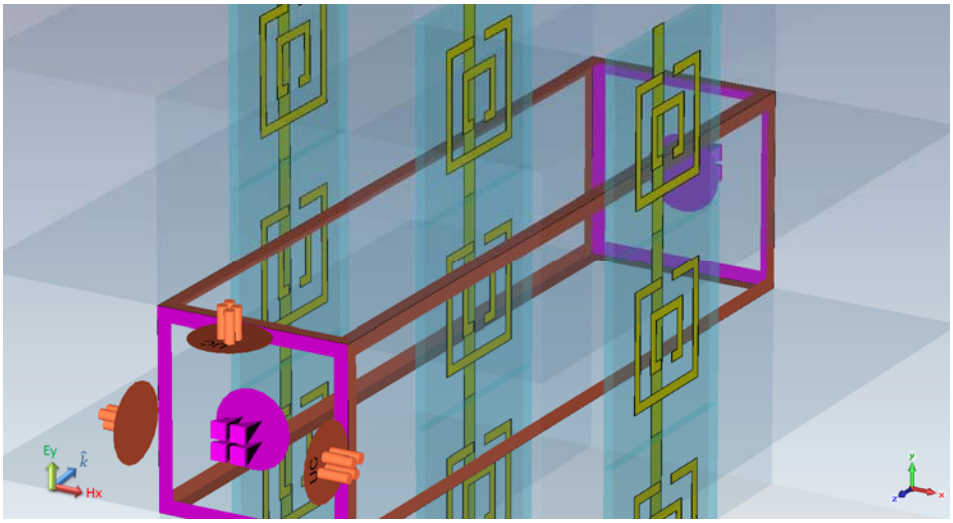

Figure 3.2. A typical SRR-Rod metamaterial for a plane incident wave propagating in the $\hat{z}$ direction with E field polarized in the $\hat{y}$ direction

It can be observed that the frequency where S11 and S21 intersect shifts from 1.1658 to 1.2208 THz in Figure 3.3, because the gap size of SRR varies from 0.5 μm to 0.75 μm, causing the capacitance change in the resonant mode.

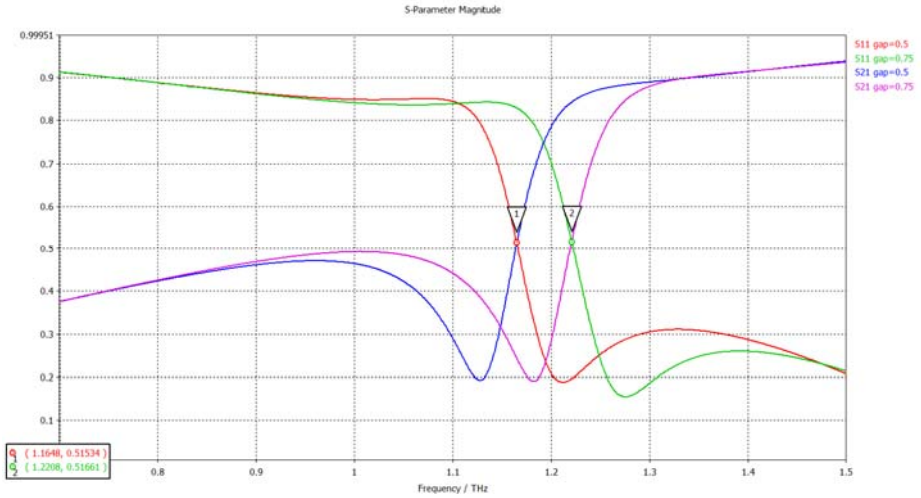

Figure 3.3. Simulation results for a typical SRR-Rod metamaterial with gap size variations from 0.5 to 0.75 μm

Second, reorientation of either the SRR or Rod in the unit cell is studied in four cases, shown in Table 3.1. The simulation results of S11 and S21 are plotted in blue and red

colored lines, respectively. Case 1 is the default, where the SRR and rod are in their original orientations. In case 2, both the SRR and rod are rotated 90 degrees around the $\hat{x}$ axis, placed at the center of the cell. In case 3, only the SRR is rotated 90 degrees around the $\hat{x}$ axis. In case 4, only the rod is rotated 90 degrees around the $\hat{x}$ axis.

Observing the transmission coefficients S21 of these four cases in Figure 3.4 and 3D simulation results shows that dramatic changes in the characteristics of the transmitted signals (including the phase, magnitude, and the phase velocity direction of the transmitted wave) occur at 1.1 THz. At 1.1 THz, the transmitted wave can be found with the backward travelling wave in case 1 and with the forward travelling wave for the other cases. Meanwhile, the minimum and maximum magnitude of S21 from four cases at 1.1 THz can be found in case 3 and case 4, respectively. It means that by mechanically rotating the SRR or Rod of the unit cell in plane, the original MM slab can be changed from a DNG material to a DPS or SNG material, resulting in high transmission, reflection or other effects.

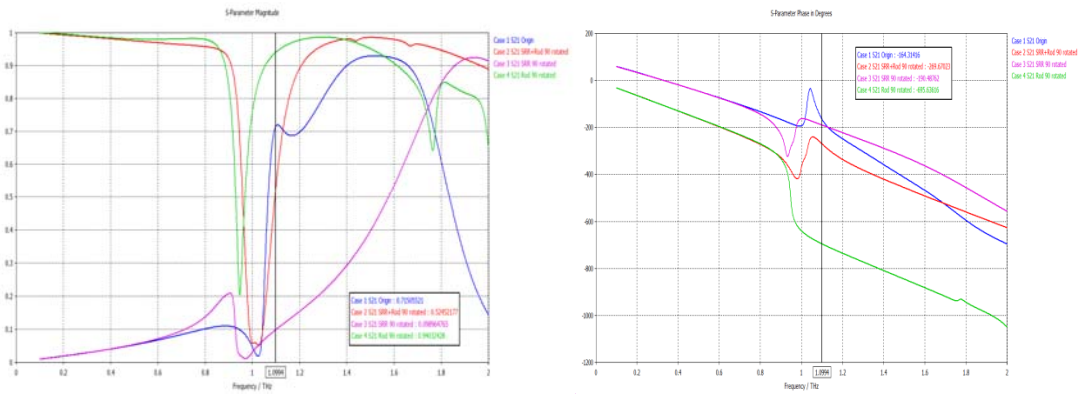

Figure 3.4. S-parameters of the SRR-Rod MM unit cell for four different orientations

Table 3.1 SRR-rode models for reorientation study and their S-parameters.

Case	The unit cell of the model	S-parameters
1 Original DNG SRR-Rod	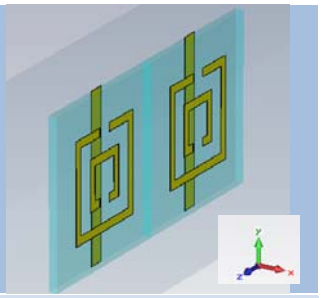	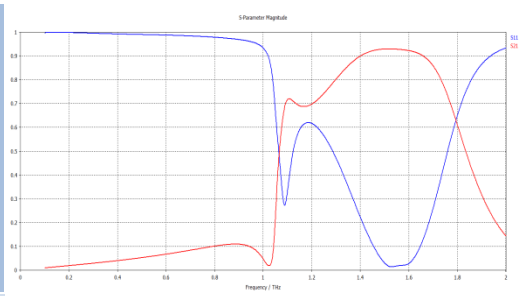
2 SRR and Rod are Rotated 90°	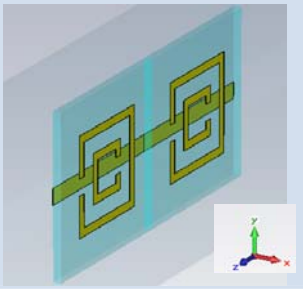	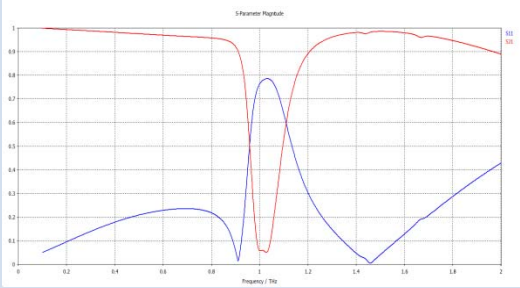
3 SRR is Rotated 90°	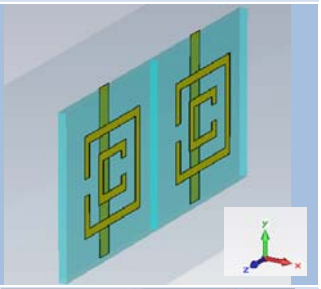	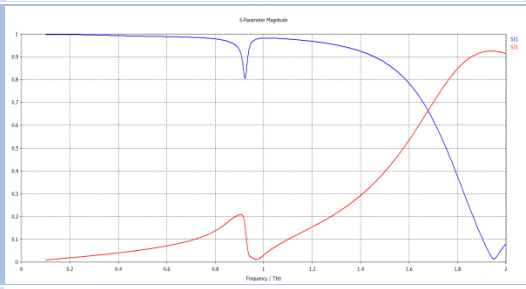
4 Rod is Rotated 90°	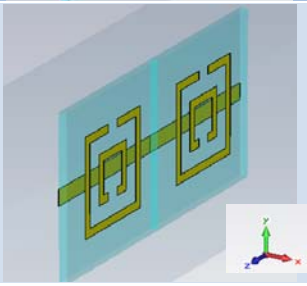	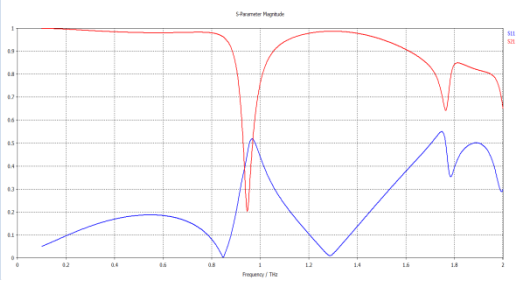

Third is a study on changing the coupling effect of multilayered fishnet MM slab mechanically. By shifting two MM layers in the wave propagation direction, the gap between the two MM layers and distances between top and bottom metallic conductors on different MM layers will be changed so that the induced resonant modes will occur at different frequencies, changing the corresponding phases and magnitudes of the transmitted waves. This study utilizes the fishnet MM model with PI protection layers described in Section 2.5. The size of the gap will vary from 0, 1, 2, 3, 4, to 8 μm.

Figure 3.5 shows the induced resonant modes are shifted due to the coupling effects between the two MM layers as the gap space changes, and can be observed in the S21 magnitude or by the S21 phase as indicated by the colored arrows. As the gap space increases, the capacitance value for the induced resonance decreases and the induced resonant frequency increases as expected.

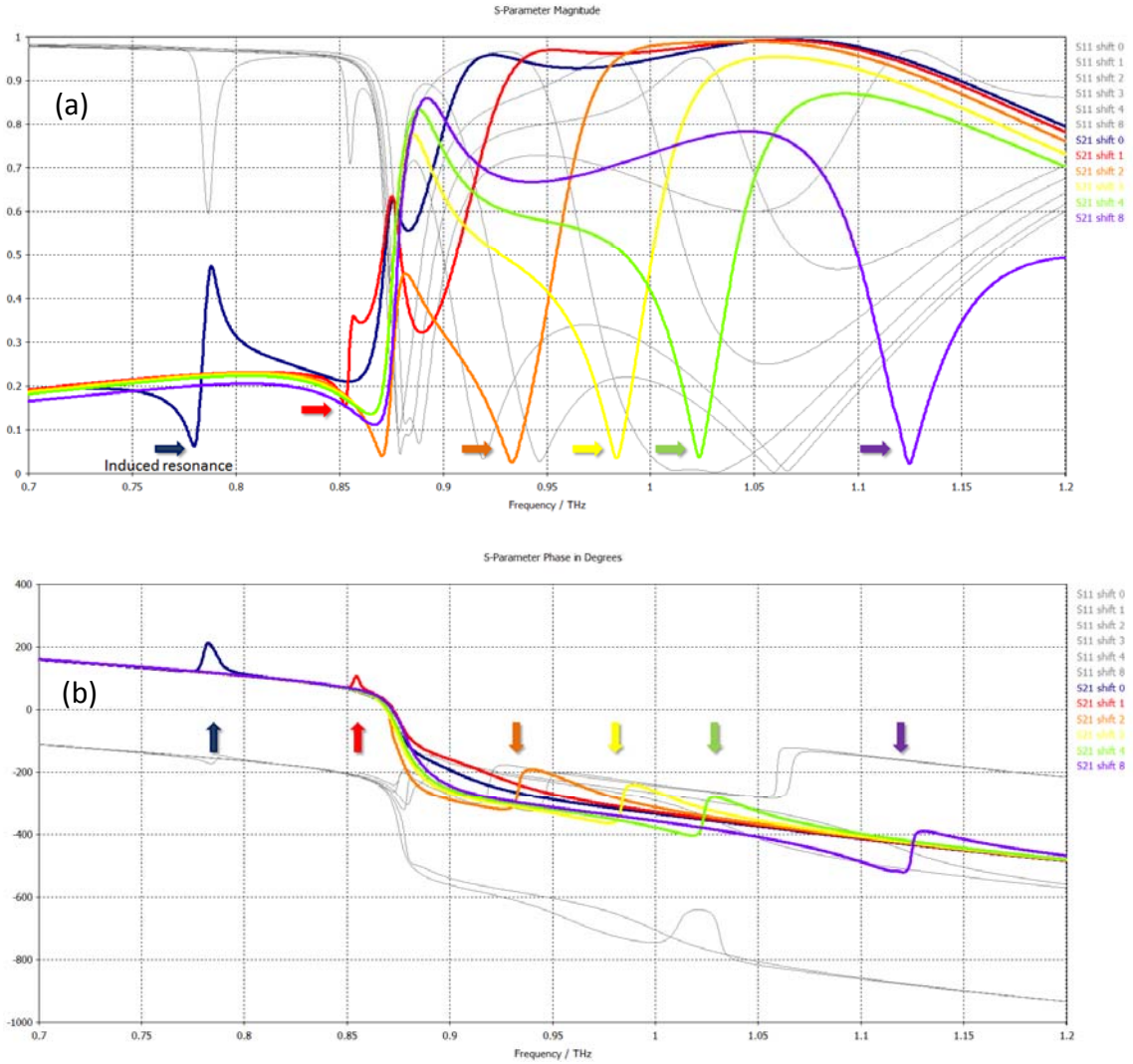

Figure 3.5. (a) The magnitudes and (b) the phases of S-parameters of a 2-layered fishnet MM slab with different shifted gap spaces between layers

In Figure 3.5, it can be seen that the transmitted signal can be changed dramatically by the shift. For example, at 0.94 THz, the magnitude of S21 can vary from 0.12 to 0.95 as

the gap size changes from 2 to 1 μm. It is worth noting that if the gap is increased to 200 μm, the backward travelling wave can be observed around the effective boundaries of the two MM layers, while the forward travelling wave can be seen in air zone between the two effective boundaries of the MM layers at the resonant mode II_a (or DNG frequency band).

3.2 ELECTRICALLY TUNABLE AMM

In addition to manipulating the metallic conductors of MM cells, moving the whole MM layer laterally, and reorienting the unit cells of MMs, there are several different tuning mechanisms based on manipulating the raw material properties (e.g. dielectric constant or conductivity) of dielectric substrates of MM cells. In [53], the conductivity of the silicon layer substrate in the gap regions is changed by laser exposure and its frequency shift can be controlled by varying the laser energy. The pattern shown in Figure 3.1(e) on the top and bottom surfaces of the MM cell and a semi-conductive substrate with varying conductivity is considered to simulate this effect. The simulated surface currents for top impinging waves with differing polarizations are shown in Figure 3.6 (b) and (c). It can be seen that for a plane incident wave polarized as (E_y, H_x), the surface currents induced by the incoming E field in the $\hat{y}$ direction cannot generate a capacitance between the gap splits of the ring. However, for an incident wave polarized as (E_x, H_y), the E field induced surface currents in the $\hat{x}$ direction can provide the capacitance required for the electric resonance between the gaps. The S11 and S21 curves for different conductivity are plotted in Figure 3.7.

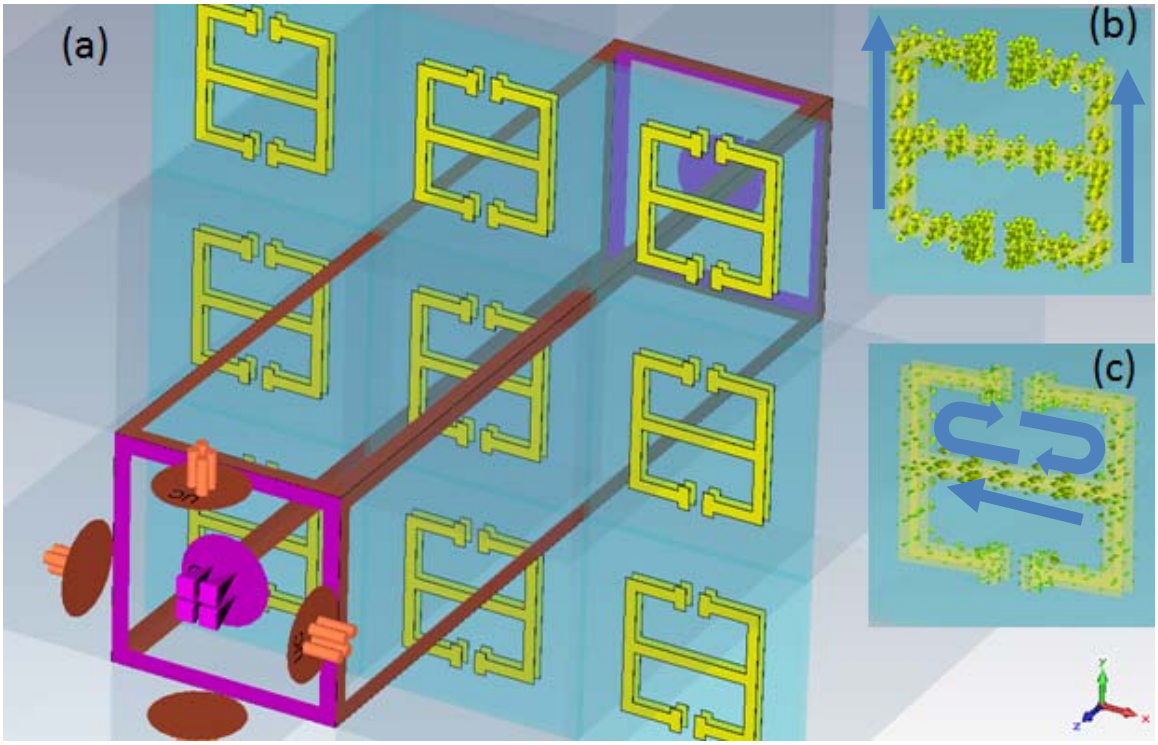

Figure 3.6. (a) Metamaterial slab impinged by an incident wave propagating in surface normal direction, (b) induced surface currents by a (E_y, H_x) polarized wave, (c) induced surface currents by a (E_x, H_y) polarized wave.

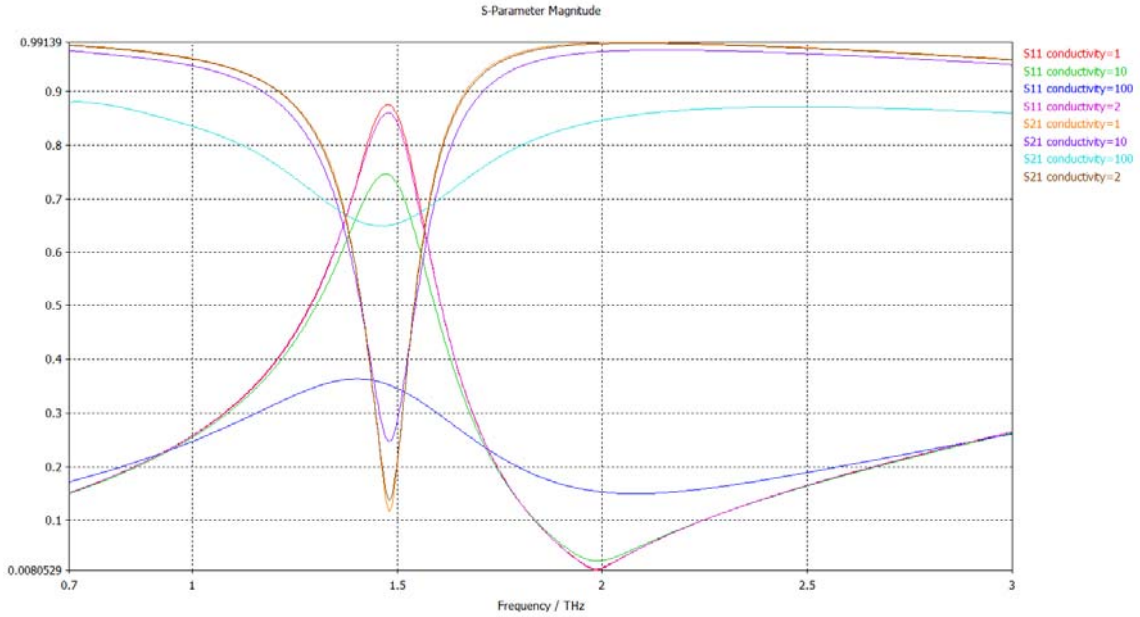

Figure 3.7. Simulation results for semi-conductive substrate metamaterials with variations in substrate conductivity

Liquid Crystal (LC) molecules are well-known for their birefringence, $\Delta n = n_e - n_o$, and reorientation ability causing refractive index changes as shown in Figure 3.8.

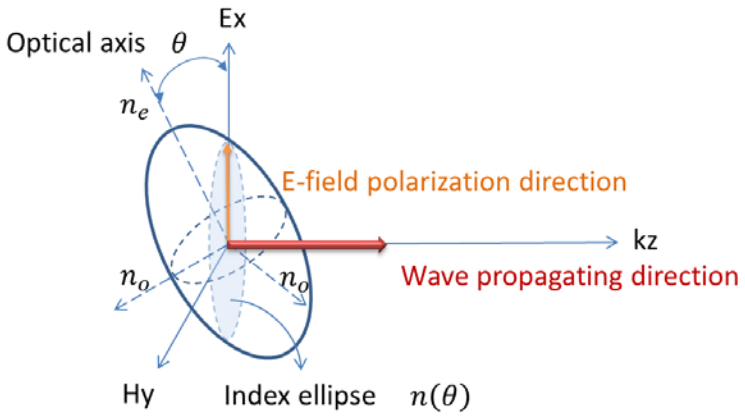

Figure 3.8. A LC molecule tilted an angle θ w.r.t the E-field polarization direction of an EM wave

The refractive index can be calculated by the refractive index of ellipse equation in (3.1):

$$\frac{1}{n^2(\theta)} = \frac{cos^2(\theta)}{{n_e}^2} + \frac{sin^2(\theta)}{{n_o}^2}$$
$$n(\theta) = \frac{n_o n_e}{\sqrt{{n_o}^2 cos^2(\theta) + {n_e}^2 sin^2(\theta)}} \quad (3.1)$$

where n_e and n_o are the ordinary and extraordinary refractive indices of a LC molecule, θ is the angle between the optical axis of the LC molecule and the wave's E-field polarization direction.

Assuming that an EM wave polarized as (Ex, Hy) is propagating in the $\hat{z}$ direction and the LC molecule with $\mu = 1$ has the optical axis aligned in the $\hat{x}$ axis, the ε of the LC molecule in tensor form can be written as

$$\varepsilon = \begin{bmatrix} {n_e}^2 & 0 & 0 \\ 0 & {n_o}^2 & 0 \\ 0 & 0 & {n_o}^2 \end{bmatrix}. \quad (3.2)$$

If the optical axis of the LC molecule is only reoriented on x-y plane and a EM wave is also polarized as (Ex, Hy), the ε of the LC molecule in tensor form can be written as

$$\varepsilon = \begin{bmatrix} \frac{{n_o}^2 {n_e}^2}{{n_o}^2 cos^2(\theta) + {n_e}^2 sin^2(\theta)} & 0 & 0 \\ 0 & \frac{{n_o}^2 {n_e}^2}{{n_e}^2 cos^2(\theta) + {n_o}^2 sin^2(\theta)} & 0 \\ 0 & 0 & {n_o}^2 \end{bmatrix}. \quad (3.3)$$

If the optical axis of the LC molecule is reoriented to be on y plane for the same EM wave polarized as (Ex, Hy), the ε of the LC molecule can be derived from (3.3) as

$$\varepsilon = \begin{bmatrix} {n_o}^2 & 0 & 0 \\ 0 & {n_e}^2 & 0 \\ 0 & 0 & {n_o}^2 \end{bmatrix}. \quad (3.4)$$

The ε of the LC molecule in different tensor forms can be used and selected carefully in the simulations to describe the anisotropic material property under different conditions, such as varied polarizations of the incident waves and orientations of the LC molecules.

Thus, another tuning mechanism can be achieved by using the reorientation property of LC. LC molecules were designed and used as a superstrate and a substrate on a MM slab for near-infrared frequencies [76]. Minovich *et al.* [77] reported an optical range design using small amounts of LC in the voids of a fishnet MM slab, while Zhang *et al.* [78] demonstrated a tunable fishnet MM with LC sandwiched by two metallic fishnet conductors operating in the microwave range. Zhao *et al.* [79], presented a design for tunable negative permeability using a periodic array of SRR infiltrated with nematic LC. In addition, variators were reported to create tunable MM with SRRs in [80, 81]. This reseach proposes the creation of a new type of tunable MM by replacing variators/capacitors in the gaps of SRR metallic patterns with a small amount of LC. The orientation of LC molecules can be controlled by using static or slowly-varying biased electric field [79], by applying external magnetic field [82], or by thermal fluctuations. Among these options, controlling the electric field achieves the best spatial resolution, with small electrode pads on the LC cells. In THz region, the LC molecules evaluated in [83] possess an ordinary optical index of $n_0 = 1.38$ and an extraordinary optical index of

$n_e = 1.43$. In the following simulations, the dielectric permittivity at LC orientation angles of 0° and 90° is assumed to be 2.0449 at and 1.9044, respectively.

Two metamaterial slabs composed of the unit cell pattern from Figure 3.1(e) on one side of the surfaces and of the unit cell with the same pattern on top and bottom surfaces are investigated as shown in Figure 3.9 (a-b).

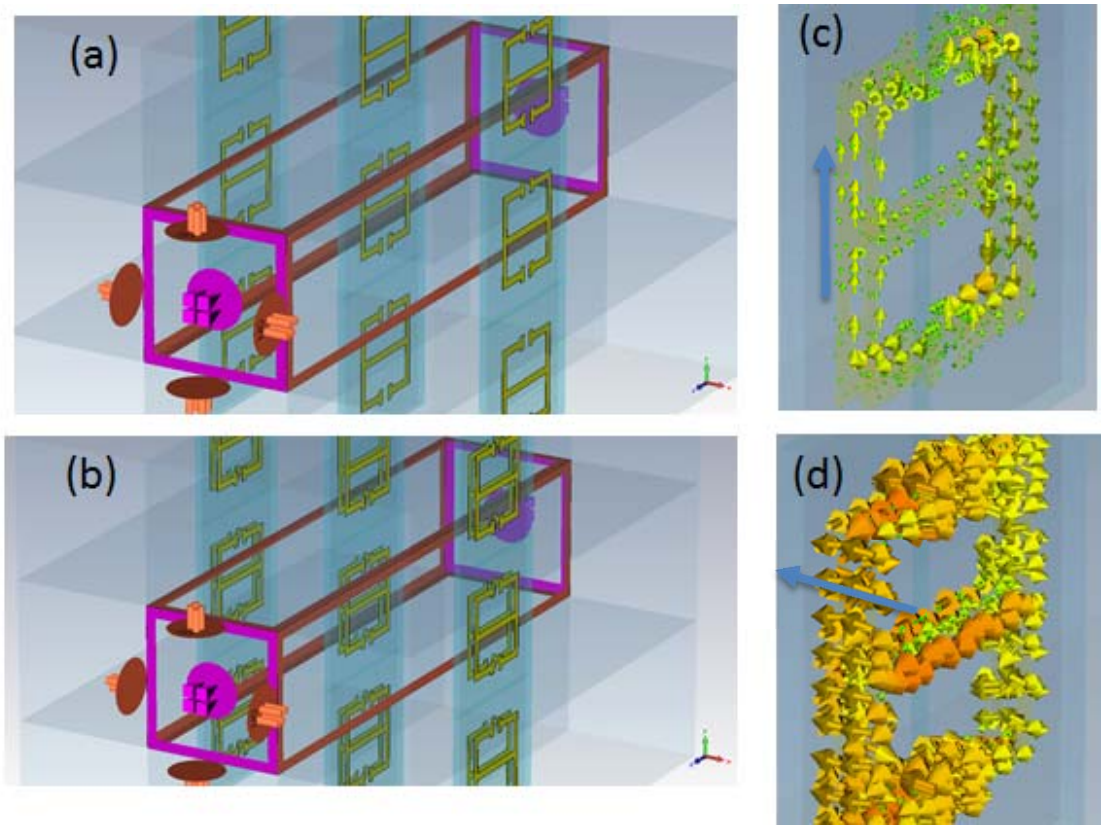

Figure 3.9. (a) The metamaterial slab with the single-side patterned unit cell, (b) the metamaterial slab with the two-side patterned unit cell, (c) TE(E_y, H_x)-wave induced surface currents, (d) TM(E_x, H_y)-wave induced surface currents.

Figure 3.9 (c-d) shows that the (E_y, H_x)-wave can generate the resonance for the capacitance in the gap splits of metallic patterns induced by looped surface currents and (E_x, H_y)-wave cannot. The simulation results are shown in Figure 3.10. Clearly, the double-side patterned MM slab has larger frequency shifting range than the single-side patterned slab.

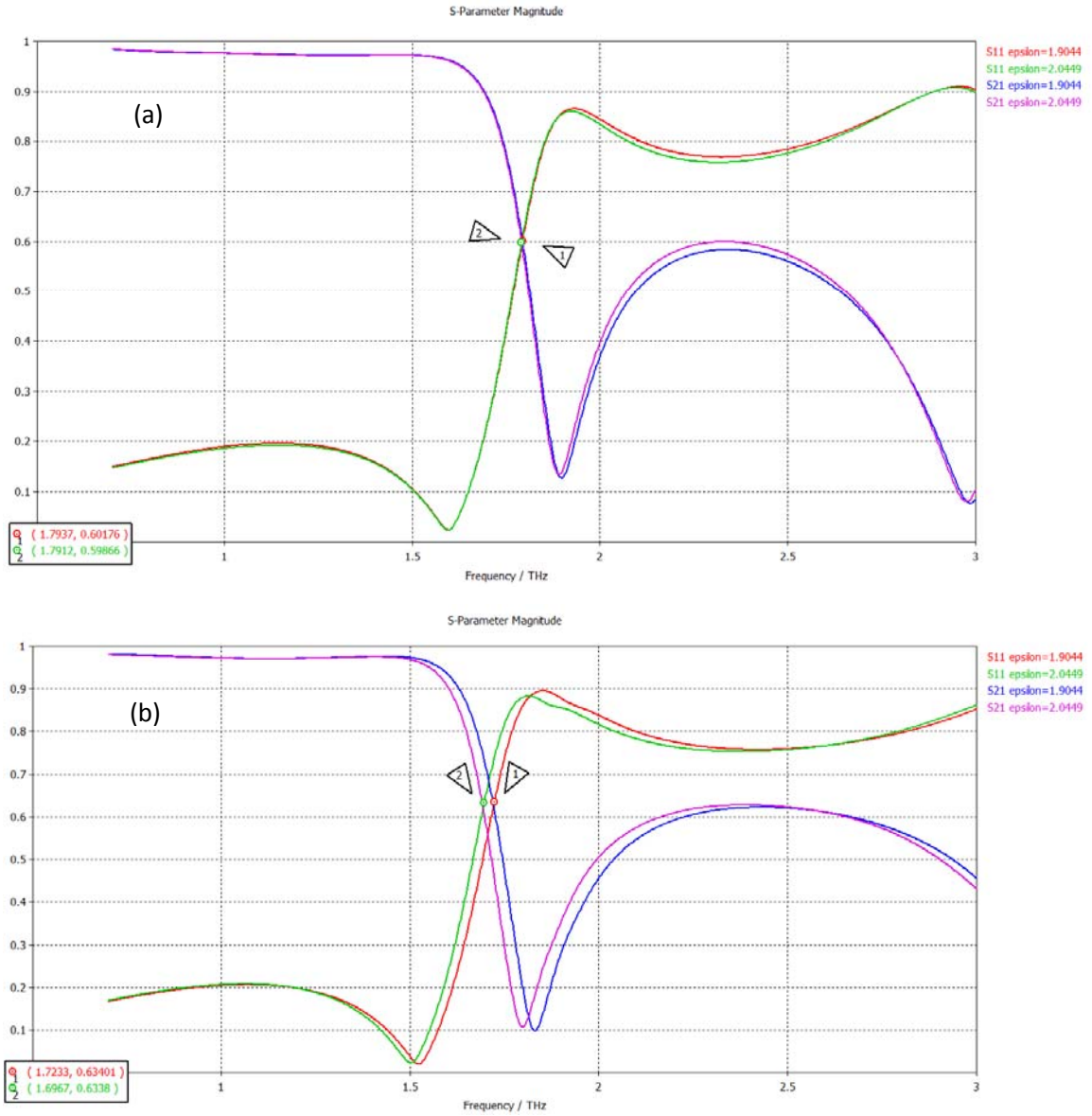

Figure 3.10. (a), (b) Simulations results of two metamaterial slabs in Figure 3.9 (a), (b) with epsilon variation, respectively.

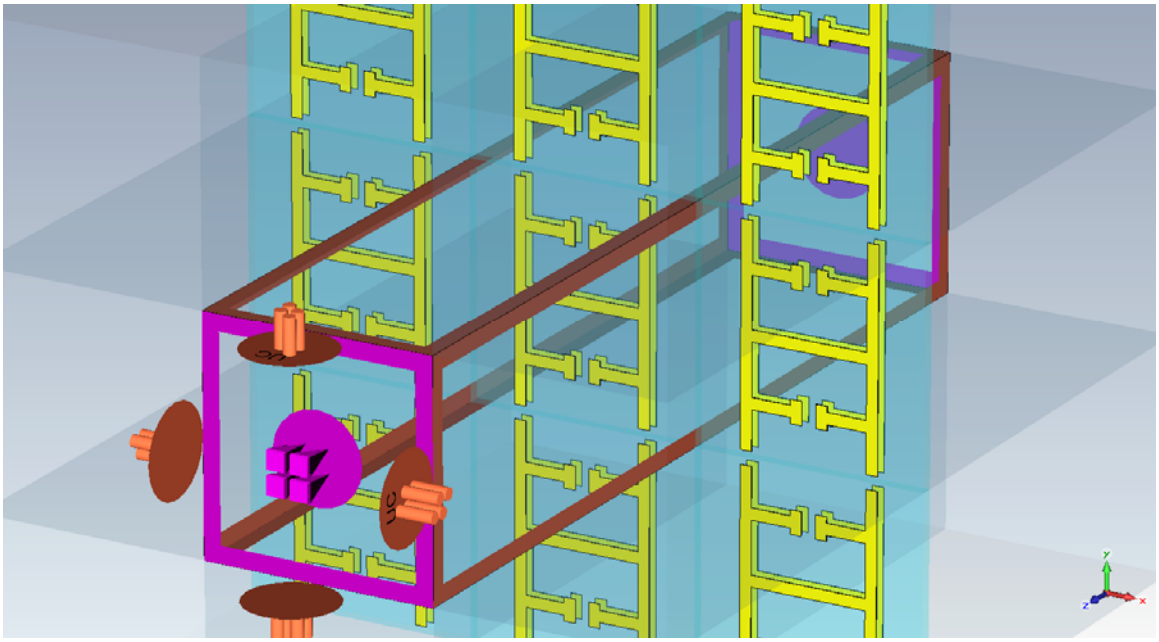

.

Figure 3.11. Metamaterial slab with double patterns on top and bottom surfaces using the SRR pattern in Figure 3.1(f)

Using the periodic unit cell patterned with gap splits in both $\hat{x}$ and $\hat{y}$ directions (shown in Figure 3.1(f)) in a metamaterial slab creates the configuration shown in Figure 3.11. Here, both the top and bottom surface are impinged upon by an incident wave propagating in the surface normal direction. The simulation results reveal that the MM reacts to both (E_y, H_x) and (E_x, H_y) polarized waves, because both waves can generate the capacitances necessary for resonant modes by the induced surface currents.

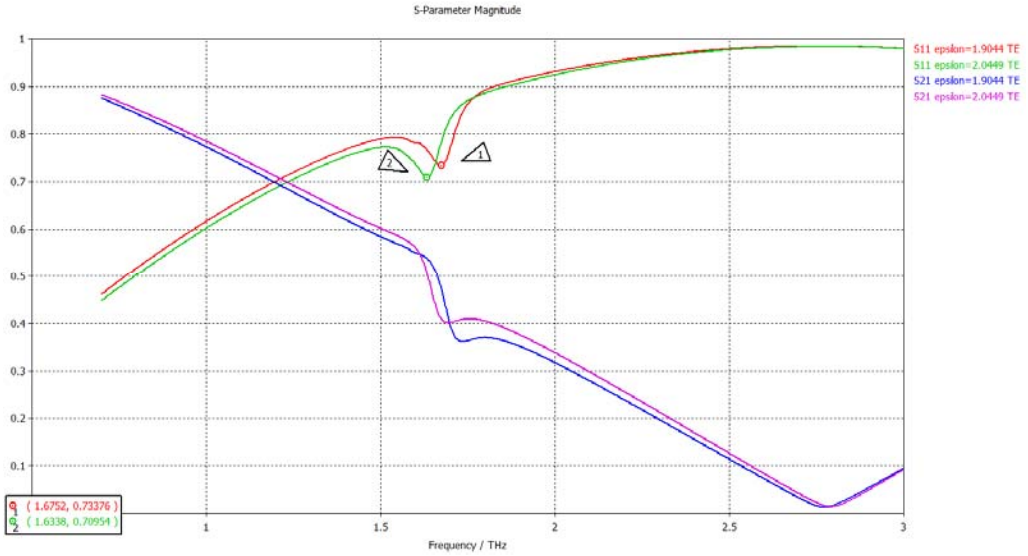

Figure 3.12. S-parameters of the MM slab for (E_y, H_x) incident wave

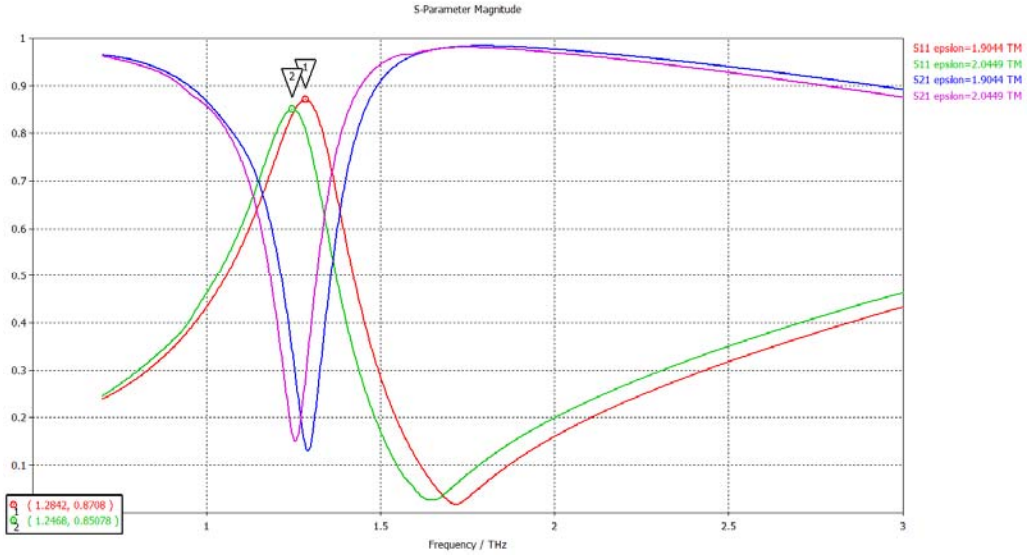

Figure 3.13. S-parameters of the MM slab for (E_x, H_y) incident wave

Next, the substrate of the 1- layered fishnet MM slab described in Section 2.5 is replaced by the LC molecules. The slab is simulated for three different orientations of the LC optical axis, aligned with the $\hat{x}$, $\hat{y}$ and $\hat{z}$ axes. The results are shown in Figure 3.14. By observing the intersections of S11 and S21 curves (the marker 1 and 2 in Figure 3.14), it can be seen that the maximum tuning frequency range is about 0.1 THz by reorienting the optical axis of LC from the $\hat{x}$ to $\hat{z}$ direction. At 0.882 THz, the magnitudes of S21 for LC optical axis aligned with the $\hat{x}$ axis and with the $\hat{z}$ axis are the same, but the phase

difference can be up to 92.2°, i.e., the phase can be changed from 69.3° to 161.5°if the LC optical axis is reoriented from the $\hat{x}$ to $\hat{z}$ axis.

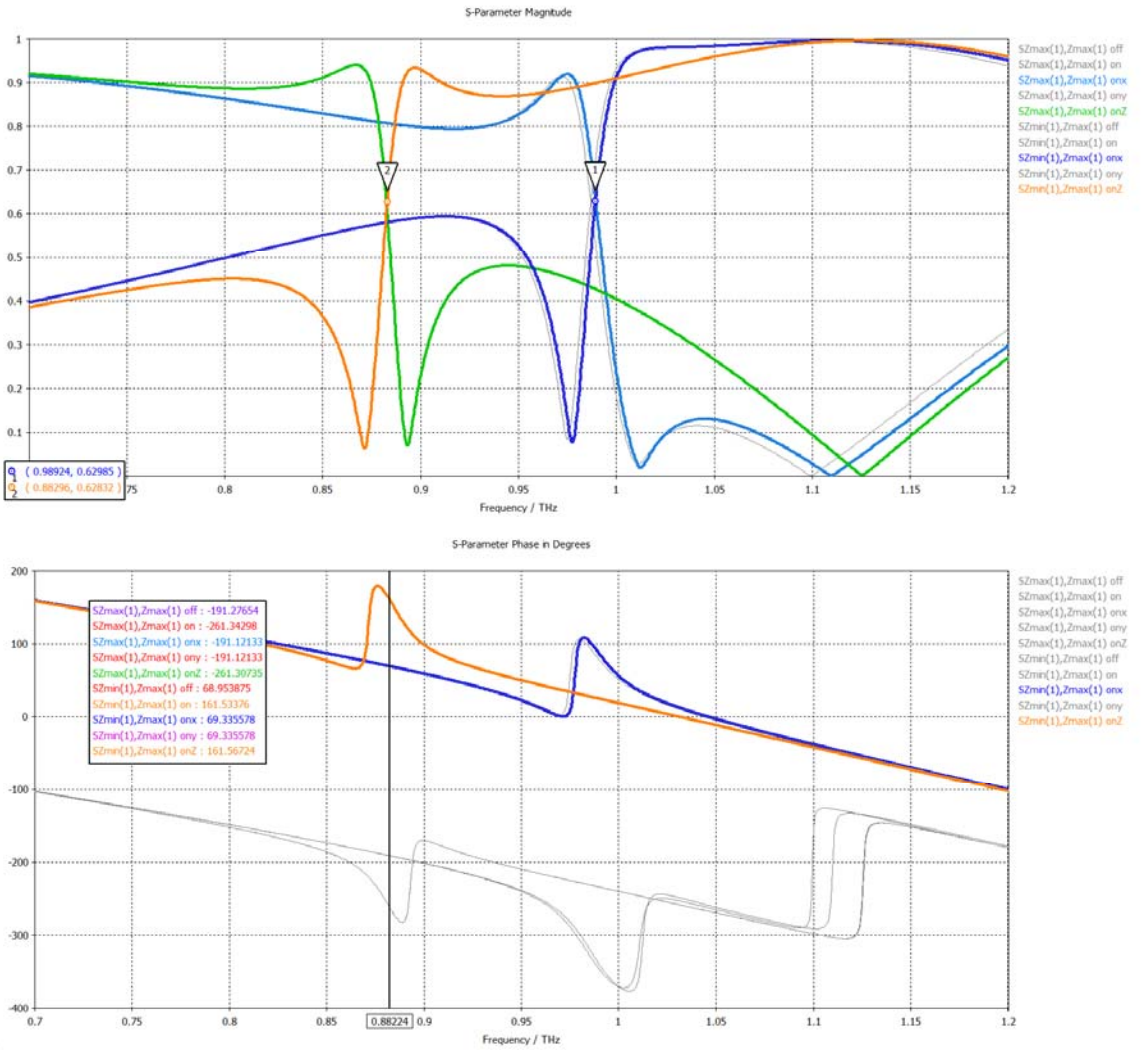

Figure 3.14. S-parameters of the single-layer fishnet MM slab for LC aligned with the $\hat{x}$, $\hat{y}$ and $\hat{z}$ axes

An investigation of the 3-layer fishnet MM slab with the LC optical axis aligned with the $\hat{x}$, $\hat{y}$ and $\hat{z}$ axes was also conducted, with the corresponding S-parameters from the simulation is shown in Figure 3.15. It can be seen that the simulation results of the cases with the LC optical axis aligned with the $\hat{x}$ and $\hat{y}$ axes are identical because of the symmetric geometry. By comparing the "mode a" resonances with the LC optical axis reoriented from the $\hat{x}$ to $\hat{z}$ axis as marked, the observed frequency shift is about -0.055

THz. The phase shift at 1.8942 THz is about -90.3°. The retrieved refractive indices with the LC optical axis aligned with the $\hat{x}$ and $\hat{z}$ axes are shown in Figure 3.16. At 0.856 THz, the real part of refractive index can be changed from -3.85 (LC aligned with the $\hat{z}$ axis) to -0.10 (LC aligned with the $\hat{x}$ axis).

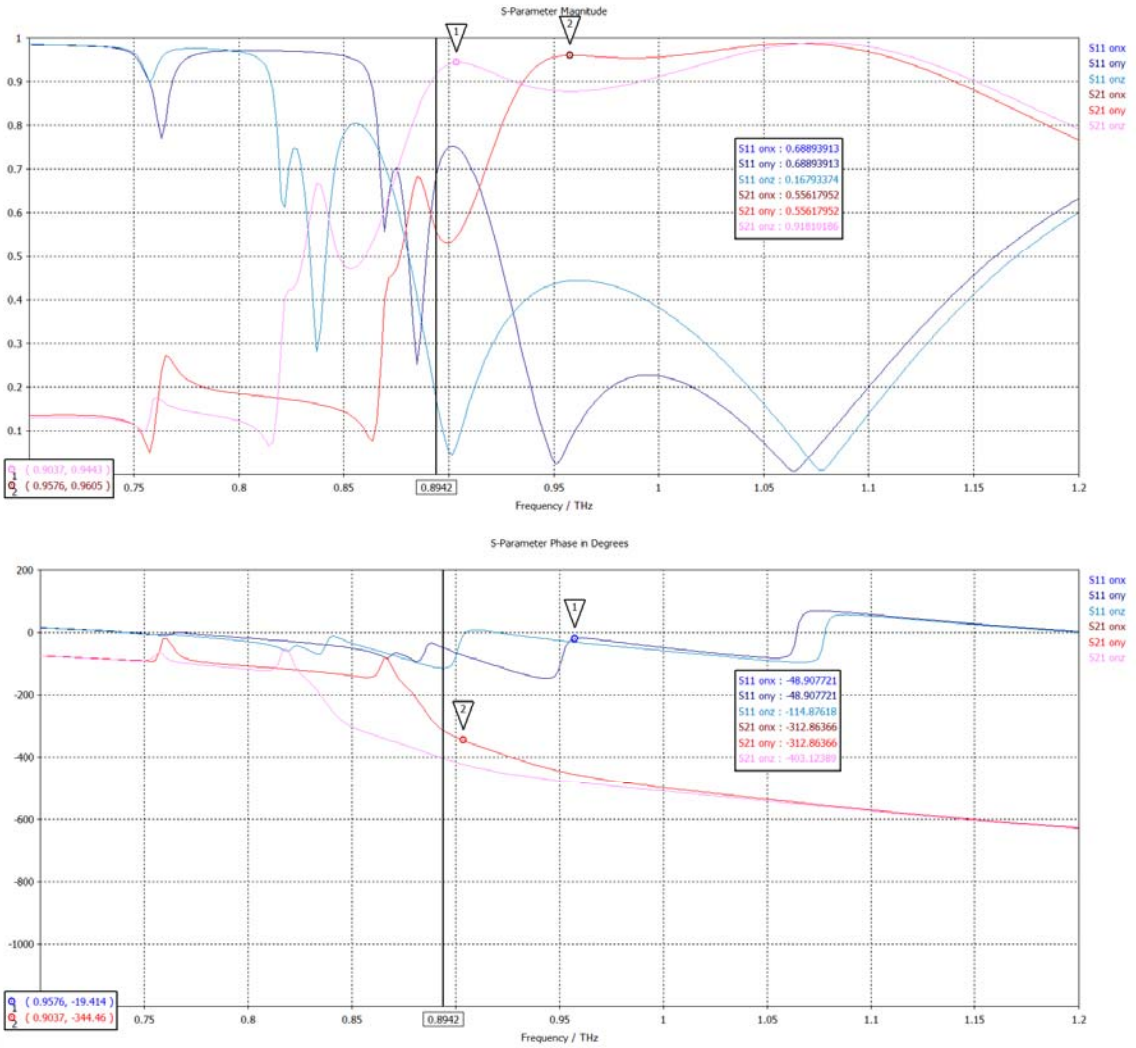

Figure 3.15. S-parameters of the 3-layered fishnet MM slab for LC aligned with the $\hat{x}$, $\hat{y}$ and $\hat{z}$ axes

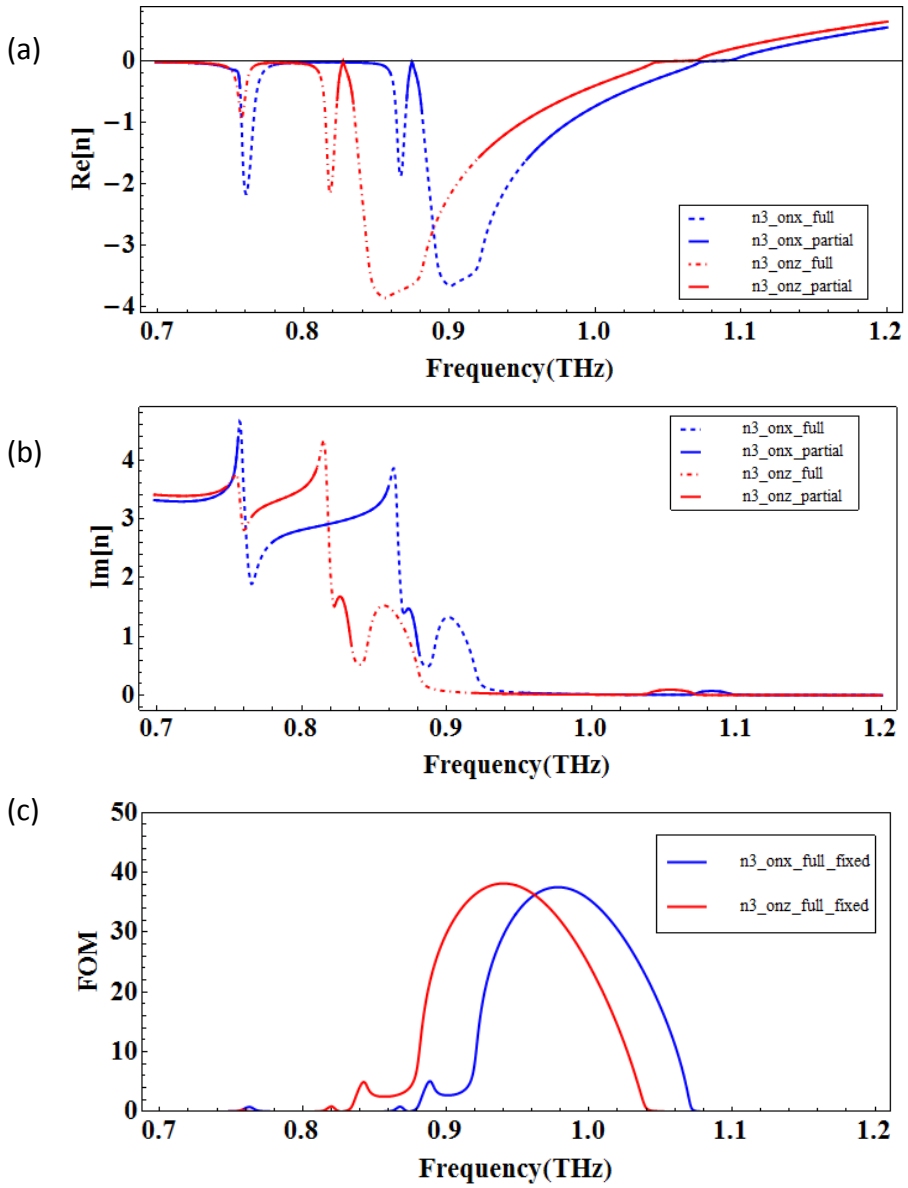

Figure 3.16. The real parts (a), imaginary parts (b) and FOM (c) of the refractive indices of the 3-layered fishnet MM slab for LC aligned with the $\hat{x}$ and $\hat{z}$ axes

Another interesting discovery of the fishnet MM is that the transmitted wave is stronger if the substrate, without the metallic conductors covering the top and the bottom, is removed or cut off. Here, several different situations of 1-layered MM models (shown in Figure 3.17) are simulated and compared, including the lossy and lossless dielectric substrate and PI layers, cut and uncut uncovered substrates and PI layers. The simulation results are calculated using the proposed methods, and shown in Table 3.2.

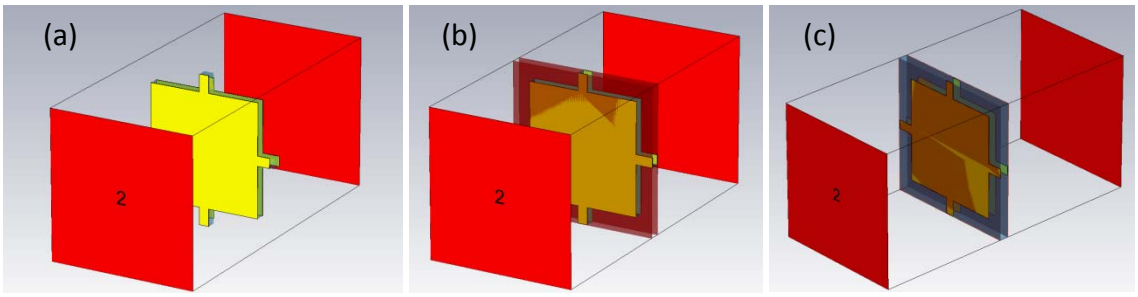

Figure 3.17.Single-layer fishnet MM models: (a) metal-uncovered substrate and PI cut off, (b) metal-uncovered substrate cut off, (c) uncut substrate and PI.

Table 3.2 The simulation results of 1-layered MM with different situations.

Gold + Lossless PI + Lossless Substrate	Max |Re[n]| @ Frequency(THz)	Max |S21|@ Frequency(THz)	Re[n]@ Max |S21|
Cut (PI+Sub.)	12.56 @0.877	0.9368 @0.896	-5.734
Cut Sub. + uncut PI	11.64 @0.869	0.9551 @0.899	-3.89362
Uncut (PI+Sub.)	9.7214 @0.815	0.9716 @0.864	-1.29721
Gold + slightly LOSSY PI + LOSSY Substrate	**Max |Re[n]| @ Frequency(THz)**	**Max |S21|@ Frequency(THz)**	**Re[n]@ Max |S21|**
Cut (PI+Sub.)	12.1428 @0.8775	0.9256 @0.897	-5.56191
Cut Sub. + uncut PI	11.2091 @0.869	0.9460 @0.9	-3.89362
Uncut (PI+Sub.)	9.15051 @0.815	0.9684 @0.865	-1.24243
Gold + more LOSSY Substrate	**Max |Re[n]| @ Frequency(THz)**	**Max |S21|@ Frequency(THz)**	**Re[n]@ Max |S21|**
Cut Sub.	9.35225 @0.8795	0.8583 @0.9115	-4.09174
Uncut Sub.	7.58056 @0.839	0.8902 @0.867	-3.39499

It can be seen that the maximum values of $|n'|$ and $|s_{21}|$ of lossy substrate cases are always smaller than the lossless substrate case. Regardless of whether the substrate and PI are lossy or lossless, the maximum values of $|n'|$ are always found in the cases where

the substrates without metal coverings are cut off and removed, and the maximum transmitted waves are always found in uncut substrate cases while the corresponding $|n'|$ are smaller than cut substrate cases. For cut substrate cases, the resonant frequencies are always higher than uncut cases because the less the substrate is in the MM slab, the lower the capacitance is for the resonance.

3.3 CONCLUSIONS

In this chapter, several tuning mechanisms and metamaterial patterns based on SRR have been proposed and simulated. The results show good tuning ability, especially for unit cells with double patterns on top and bottom surfaces. However, due to the anisotropic characteristics of a typical SRR pattern, the polarization orientation of the incident wave is critical and selective. The proposed SRR-based pattern needs to be modified to react to incident waves with different polarizations. Some of the proposed SRR designs can only provide negative permittivity for certain incident directions, while others can provide DNG for certain incident directions. In addition, the dielectric permittivity of LC cannot be controlled using the metals on top and bottom surfaces as electrodes to create biased voltages, due to the discontinuity of the metallic conductor in the SRR-based pattern. To solve this problem, a fishnet structure is adopted for tuning LC with top and bottom conductive patterns as electrodes. Finally, to have a conformable metamaterial slab, a flexible polymer-based substrate and active metamaterial is necessary to fine tune the requested properties.

Chapter 4. NOVEL DEVICES BASED ON ACTIVE CONTROL OF TUNABLE METAMATERIALS

Lenses are the most fundamental optical elements in manipulating electromagnetic waves. Lenses can be used to collimate, reflect, refract, focus, or filter EM waves depending on their geometry, curved interfaces, and materials. Traditionally, a lens can only be designed for one purpose; as a result, an optical system usually requires many elements and can end up becoming very bulky and complicated. In addition, the diffraction limit, which is roughly half of the operating wavelength in the medium, imposes constraints on the device geometry and limits to the spatial resolution. To overcome these problems, two techniques are proposed: one using an active controlled metamaterial lens that can transform the lens to perform different functions (e.g. convergence, divergence, collimation, etc.) by applying a voltage. The second design is an active controllable patternless metamaterial waveguide to achieve a low-dispersion, low-loss waveguide while actively controlling wave propagation properties.

4.1 MULTIFUNCTIONAL FLAT LENSES

A conventional lens shaped with different curves can be operated with positive refractive index but constrained by the diffraction limit. However, the spatial resolution of the lens can be improved by liquid or solid immersion techniques [84-86], but it is still limited by the refractive index of natural materials. As shown in Figure 4.1, a gradient flat lens infiltrated with nonuniformly distributed LC molecules can create an optical effect similar to a triangular prism. To create such gradient LC cells, a UV curable polymer dispersed liquid crystal (PDLC) is adopted in the design as a dielectric substrate. Exposing the material at different intensities forces the LC inside the polymer matrix to form pockets of varying sizes. Since the ordinary and extraordinary refractive indices of PDLC can be changed corresponding to the average size of the liquid crystal droplets inside the polymer host medium, the material can be exposed at a constant increase

dosage to achieve the effect of a prism. In this chapter, a multifunctional flat lens sandwiched a gradient PDLC substrate is proposed. The idea is to use this design to create a tunable flat lens, a prism with active steering, or even more complicated lens designs depending on how the PDLC substrate is configured. However, this type of flat lens still possesses a positive refractive index, meaning that it is constrained by the diffraction limit, and cannot achieve subwavelength focus.

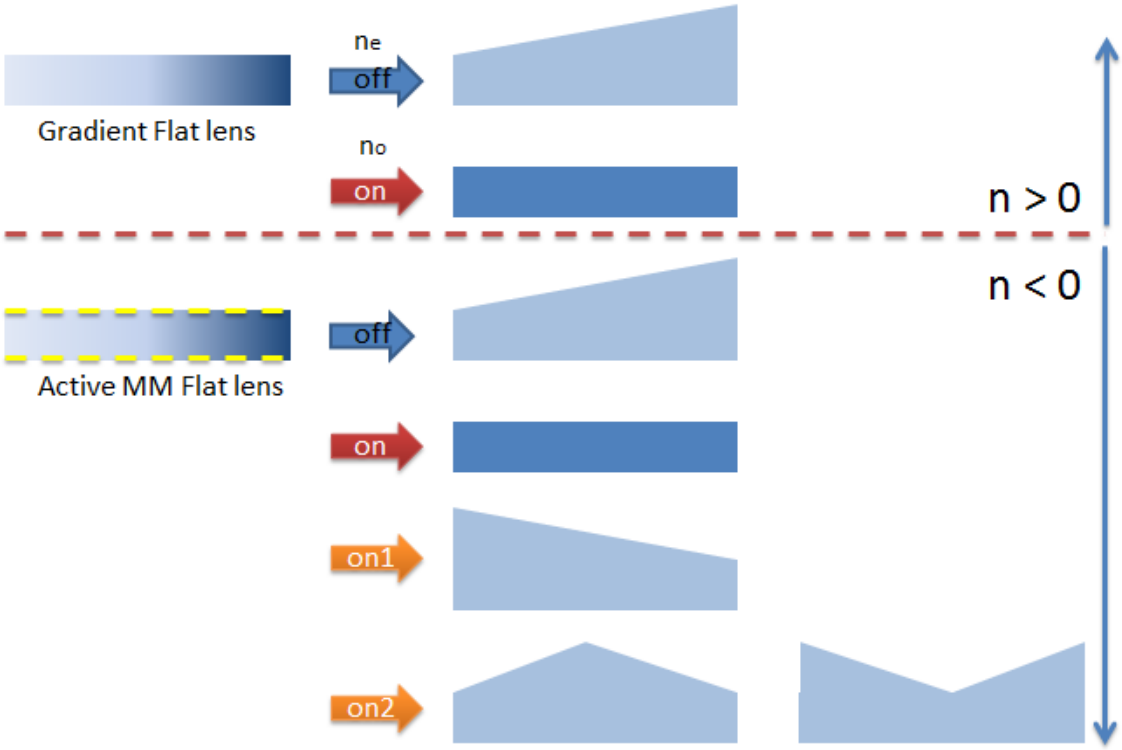

Figure 4.1. Proposed multifunctional flat lenses

A multifunctional flat lens with a negative refractive index and sub-wavelength focusing capabilities will need to be made of tunable active metamaterials and a gradient PDLC substrate whose material properties of each individual cell can be altered independently. When no biasing voltage is applied to the gradient PDLC substrate, the lens will act like a wedge-shaped prism with a negative refractive index. When a biasing voltage is applied, the lens loses the gradient refractive index and can be regarded as a flat lens with a controllable negative refractive index. However, if the conductive metallic wires and patterns on the metamaterial surface are all connected (as in fishnet MMs), the wires

cannot be used as electrodes to address and control each MM unit cell independently. As a result, the whole material has to be tuned in the same pace, as discussed in Section 3.2. Naturally, if all the wires to the patch patterns on the MM surface are disconnected, there is no way to apply a biasing voltage to the unit cells. Adding additional wires to apply biasing voltages will destroy the resonant mode of the original pattern. Therefore, when the SRR MM slab in Figure 2.1 is infiltrated with electrically-tunable dielectric (e.g. LC, PDLC, or EO), it can be tuned by external electrodes placed on opposing surfaces (e.g. top and bottom surfaces on y-z plane) of the slab, such that any applied voltage affects the entire slab.

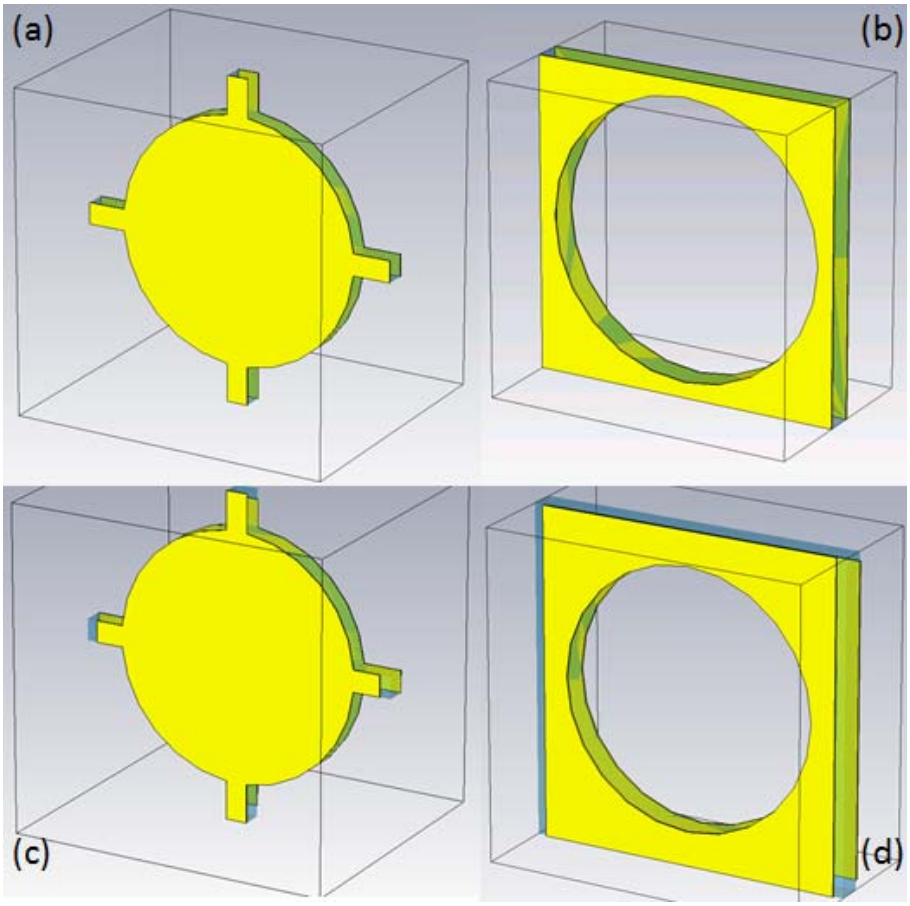

Figure 4.2. Proposed active metamaterial patterns: (a) 'Dotnet' MM unit cell, (b) 'Holenet' MM unit cell, (c) partially disconnected dotnet MM unit cell, (d) partially disconnected holenet MM unit cell.

In this chapter, several active metamaterial pattern designs (shown in Figure 4.2) are proposed to achieve independent control of each MM unit cell. A flat lens composed of

the pattern shown in Figure 4.2 (d) is plotted in Figure 4.3. It can be seen easily that the metallic conductors on the top surface are all connected in the $\hat{y}$ direction and disconnected in the $\hat{x}$ direction. On the bottom layer, the conductors are all connected in the $\hat{x}$ direction and disconnected in the $\hat{y}$ direction. As a result, different voltages can be applied to the different metallic strips, resulting in variable biasing voltages for each unit cell of a MM slab. The Appendix demonstrates several different functions for the voltage distributions on the top and bottom electrodes so that different voltage biases can be generated to alter the orientations of the PDLC for different unit cells. These functions create different equivalent 3D geometries of the lens conductors, including prisms with the flat surface tilted in different directions, a wedge with 2 different tilted slopes as a beam splitter, 1D/2D concave/convex lenses, and periodic ridged grating lenses, etc. In addition, the transformation optics [87] technology is the key to providing a well-calculated gradient distribution of refractive indices in the material, which is required to create a Luneburg lens or a perfect cloaking system.

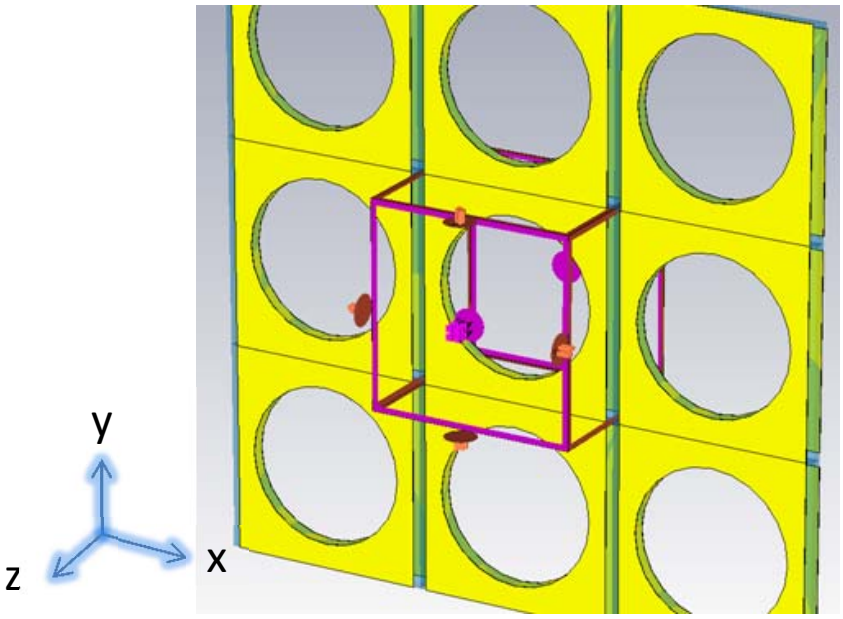

Figure 4.3. A proposed multifunctional flat lens is made by the active metamaterial pattern with disconnected wires in one lateral direction.

In Figure 4.4 (a), a beam converter is simulated by a gradient negative refractive index distribution from -3 at two sides to -1 at the center of a flat lens (greater computing power

is necessary for more complex situations). A plane incident wave is converged to a focal point and the wave front is changed from planar to circular. In Figure 4.4 (b), a beam splitter is simulated by a gradient negative refractive index varying from -1 at the sides to -2 at the center of the lens, separating the incident plane wave into two main beams propagating in different directions.

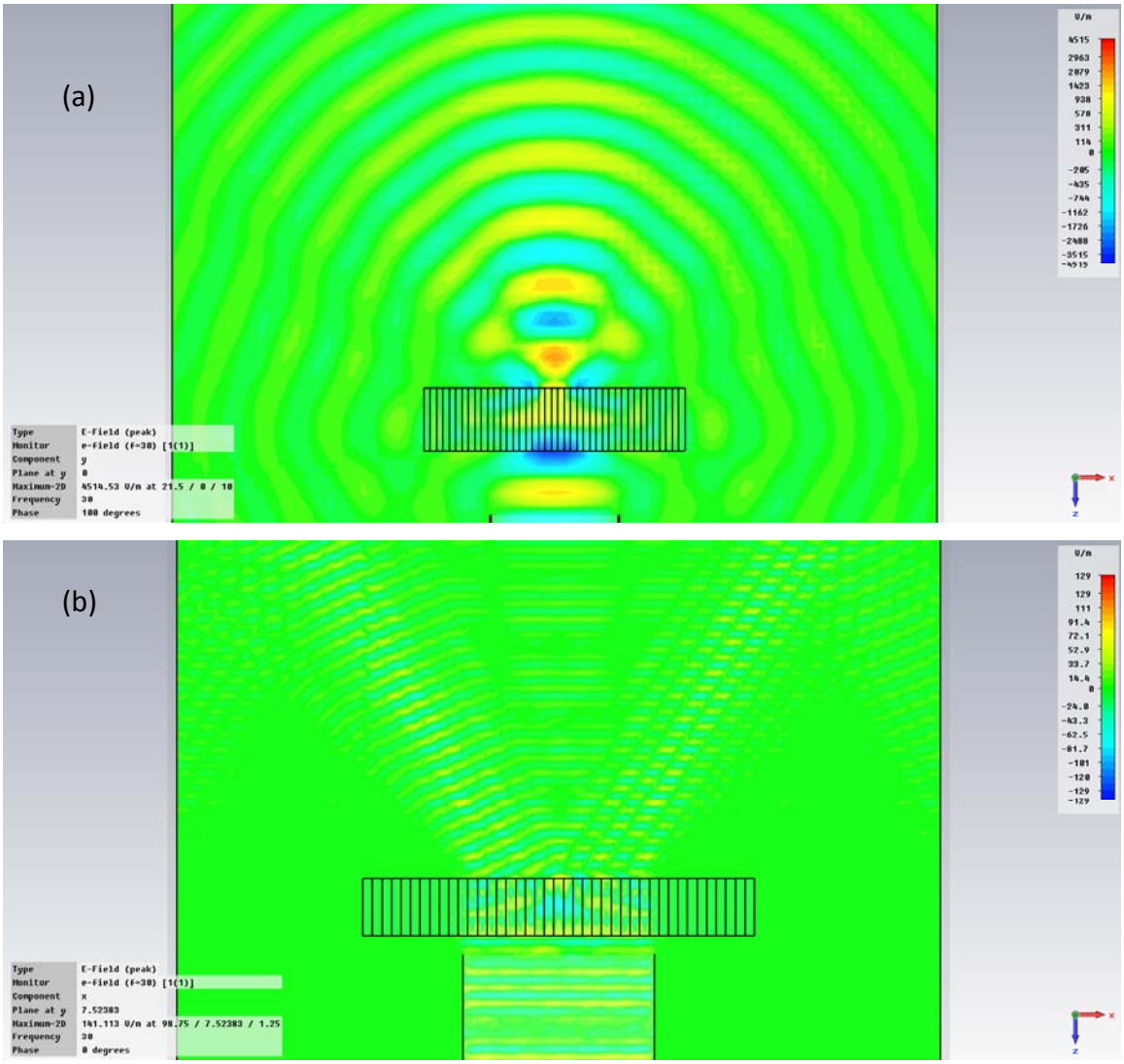

Figure 4.4. The proposed multifunctional flat lens emulating: (a) an equivalent beam converter, (b) a beam splitter .

4.2 PATTERN-LESS WAVEGUIDE

Waveguides are widely used to confine and steer EM waves while maintaining signal integrity. However, due to the wave propagation in free space or naturally occurring media, the diffraction limit still constrains the size of waveguide designs. To get around the diffraction limit, minimizing the device size and increasing the spatial resolution, the waveguide must be able to operate on EM waves with a beam size smaller than half of the wavelength.

The design for this waveguide is shown in Figure 4.5. Parallel metallic plates possessing negative permittivity can be considered 1D waveguides, confining the wave between the plates in sub-wavelength degree, with the E field polarized parallel to the surface normal. However, in another transverse direction, the beam size of the wave is still constrained by the diffraction limit. Analogous to waves with E fields polarized parallel to the surface normal of the plates, the waves with magnetic fields polarized parallel to the surface normal of parallel negative permeability plates can also be confined. Therefore, a novel waveguide based on active metamaterials is proposed, able to be controlled and tuned to become DNG or ENG or MNG material.

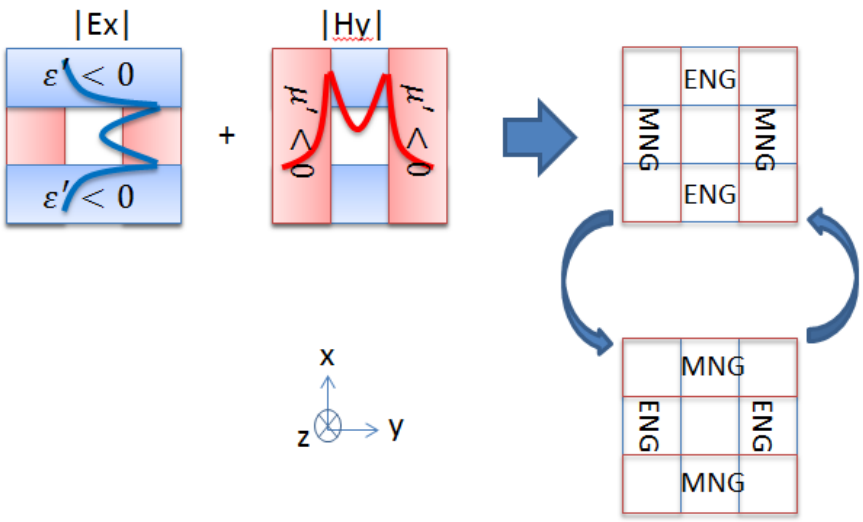

Figure 4.5. Concepts of guiding EM waves with ENG and MNG materials

Assuming that ENG and MNG materials (respectively indicated as blue and green, in Figure 4.6) described by a Drude model are set to be negative for frequencies below 5 THz, the waveguide is designed to have the ENG material stacked in the $\hat{x}$ direction and the MNG material in the $\hat{y}$ direction. At 1 THz, only a plane incident wave polarized in (E_x,H_y) (instead of (E_y,H_x)) can be transmitted and guided within the waveguide, due to negative ε material in the $\hat{x}$ direction and negative μ material in the $\hat{y}$ direction. If the wave is operating at 9 THz, the wave will not be confined within the waveguide. Another interesting application is to create a tapered waveguide by tuning the material to have gradient properties, as shown in Figure 4.6 (c).

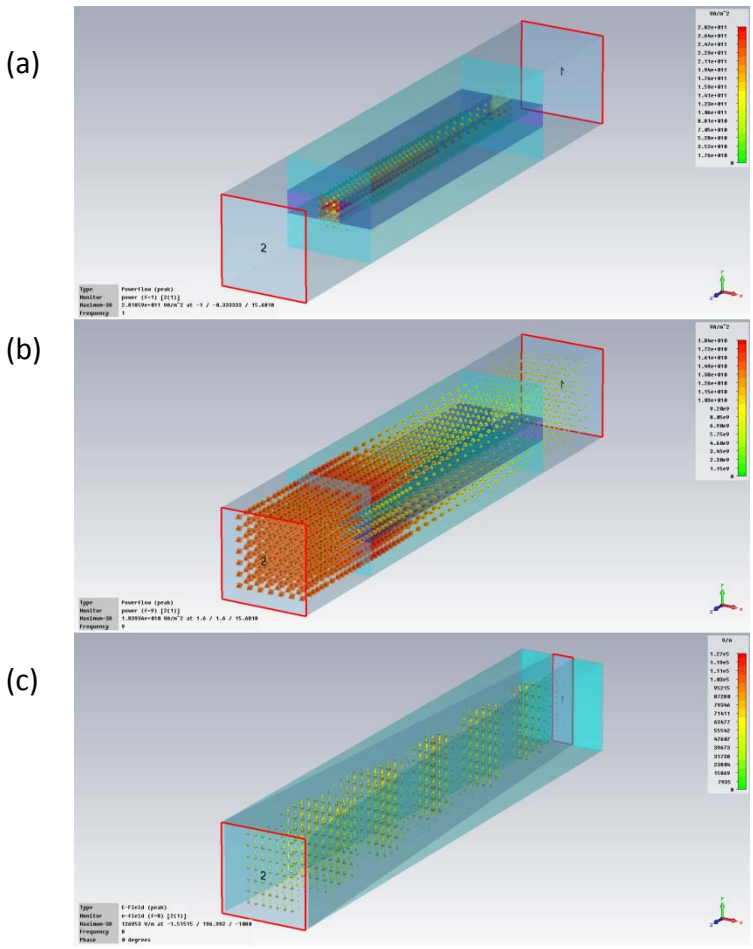

Figure 4.6. Simulation results of a reconfigurable waveguide. (a) Power flow plot for a (E_x,H_y) polarized wave at 1 THz, (b) Power flow plot for a (E_x,H_y) polarized wave at 9 THz, (c) E field plot of a taped waveguide for a (E_x,H_y) polarized wave at 1 THz.

4.2.1 *Mechanically Controlled Waveguide*

In order to change the material properties of the media surrounding the waveguide, mechanical tuning mechanisms were proposed to change the resonant frequency of the MMs deployed around the waveguide. For example, by stretching, squeezing, or heating the material, the conductive metallic pattern on the MM unit cell can be changed. Another way to change the metallic pattern is shown in Section 3.1, where reorienting the direction the whole unit cell or just the SRR or Rod components can shift the resonant

frequency higher or lower, also changing the material properties at the operating frequency from DNG to ENG or to MNG as desired.

4.2.2 *Electrically Controlled Waveguide*

The most promising tuning mechanisms proposed in this research is to change the material properties electrically by applying biasing voltages or external magnetic fields onto the MM cells as discussed in Section 3.2. For a typical DNG MM slab, the distributions of DNG, ENG, MNG and DPS can be illustrated as in Figure 1.4. By altering the resonant frequency, the distributions can be changed as desired. To have an ENG material, the frequency can be operated in area (1)-(4). To have a MNG material, the operating frequency can only be selected in area (3). In addition, if the transmitted signal is expected to be highly transmitted, the operating frequency should be selected in area (3-5). Otherwise, the wave can be highly reflected, if the frequency is selected in area (1). As a result, pattern-less waveguide structures are proposed based on the tunable active MM patterns in Figure 4.2 and can be controlled to allow different beam sizes of incident waves to be transmitted and different polarized waves to pass or follow different routes to certain destinations, as shown in Figure 4.7.

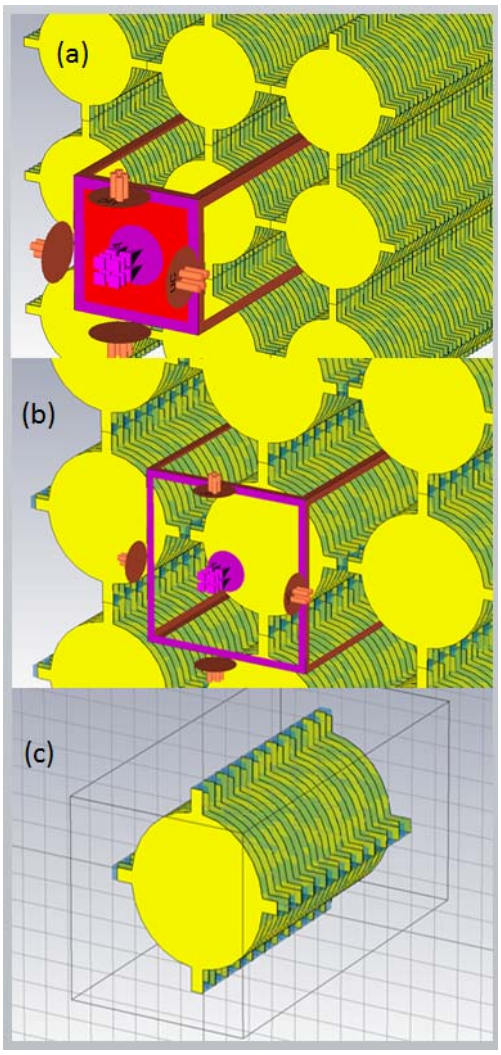

Figure 4.7. Pattern-less waveguide design with (a) all conductors connected and (b) conductors partially connected in the $\hat{x}$ and $\hat{y}$ directions, (c) a single unit element of the waveguide.

The simulated S-parameters of a 20-layered partially-connected fishnet MM slab are shown in Figure 4.8. A dramatic phase change can be found in the 1.17-1.27 THz range due to multiple resonant modes induced by strong coupling effects. Different wavelengths of backward travelling waves can be found in the same frequency band, as shown in Figure 4.9. It can be seen that for the lower frequencies in the negative refractive index band, more numbers of waves are inside the waveguide. For MM slabs with fewer layers, the strongest transmitted wave in the band can be found at resonant

"mode a", accompanying with its half wavelength equal to the slab thickness. For the 20-layered MM slab, the strongest transmitted wave in the band can be found at 1.251 THz. Since the substrate of the proposed pattern-less waveguide is made of PDLC and tuned by DC biasing voltages, we can apply different biasing voltages to different parts of the waveguide, creating pass/stop zones in the waveguide to output different beam sizes or create interference through phase differences.

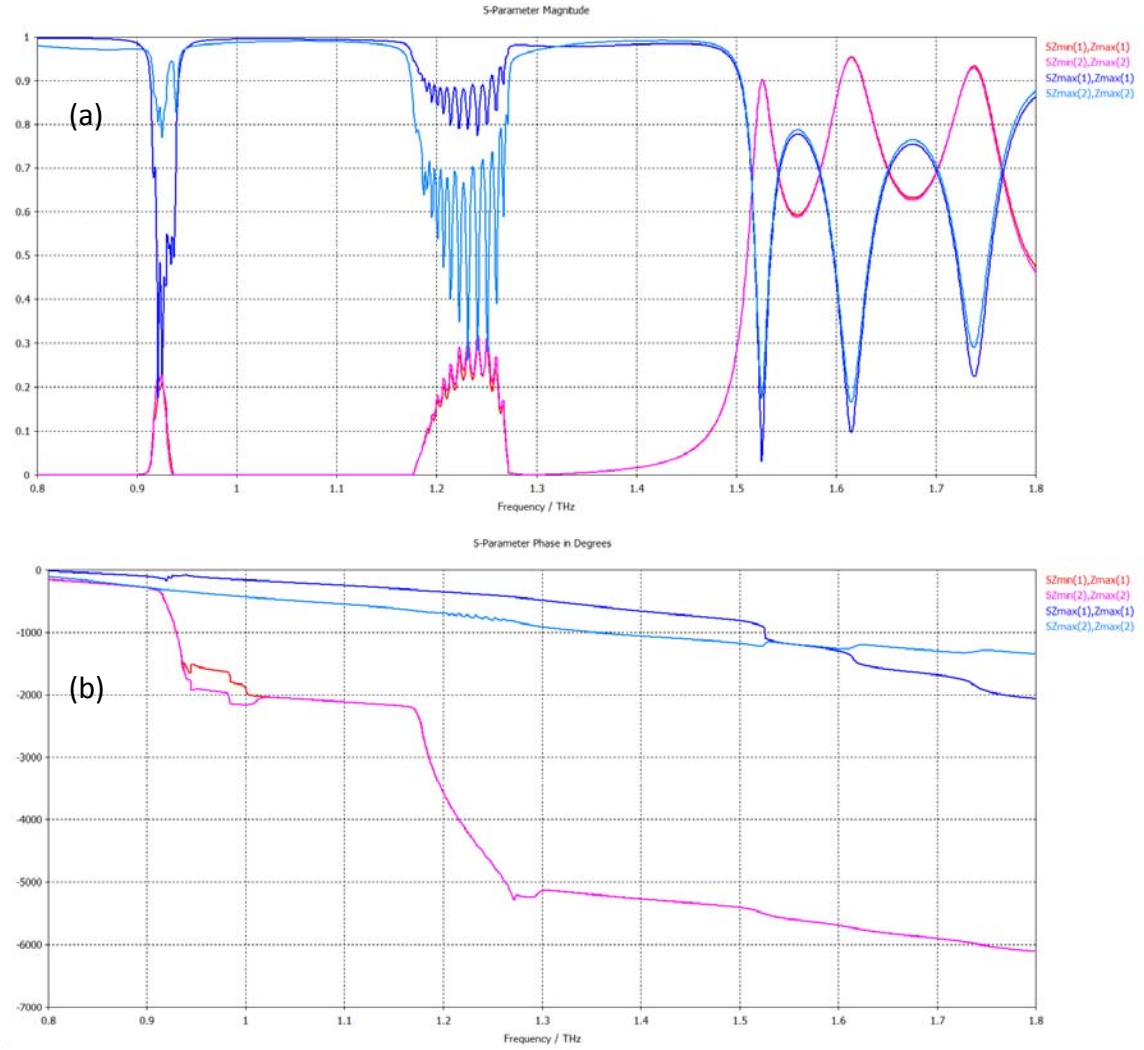

Figure 4.8. The S-parameter magnitudes (a) and phases (b) of a 20-layered dotnet MM slab comprised of the unit cell shown in Figure 4.2(c)

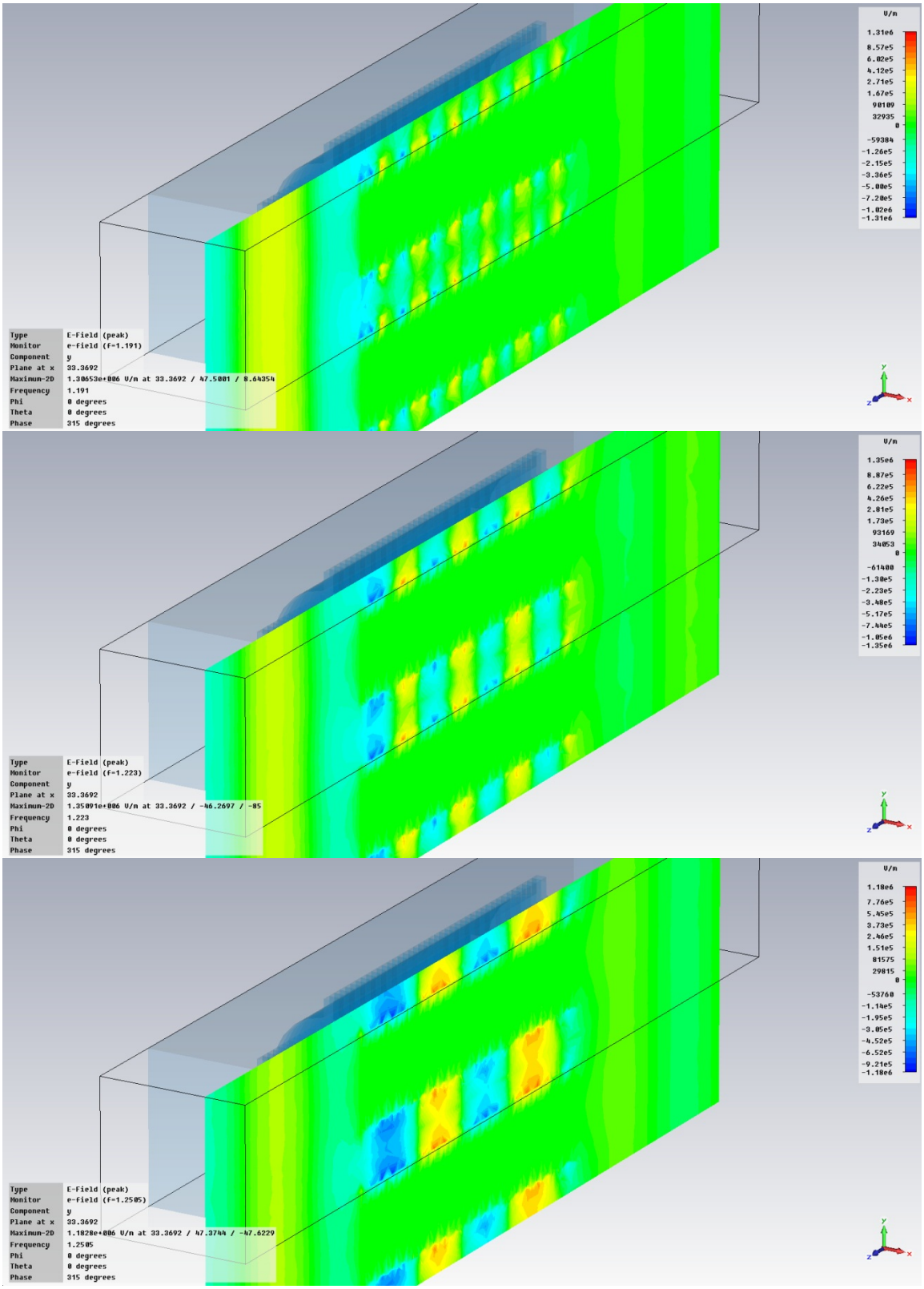

Figure 4.9. E field plot of the backward travelling wave at (a) 1.191 THz, (b) 1.223 THz and (c) 1.251 THz

To obtain sharper and clearer resonant peaks of S21, the metallic conductors of the 20-layered partially disconnected Dotnet MM slab was changed from gold to PEC. The S-parameters from the simulation results can be found in Figure 4.10. The resonant modes in the negative refractive index frequency band can be found at frequencies from 1.179 THz to 1.271 THz and maximum transmitted wave in the band can be found at 1.224 THz. In Table 4.1, it can be seen that different numbers of waves exist inside the waveguide at different resonant modes, and it can be used to verify the values of the retrieved refractive indices obtained by the proposed methods.

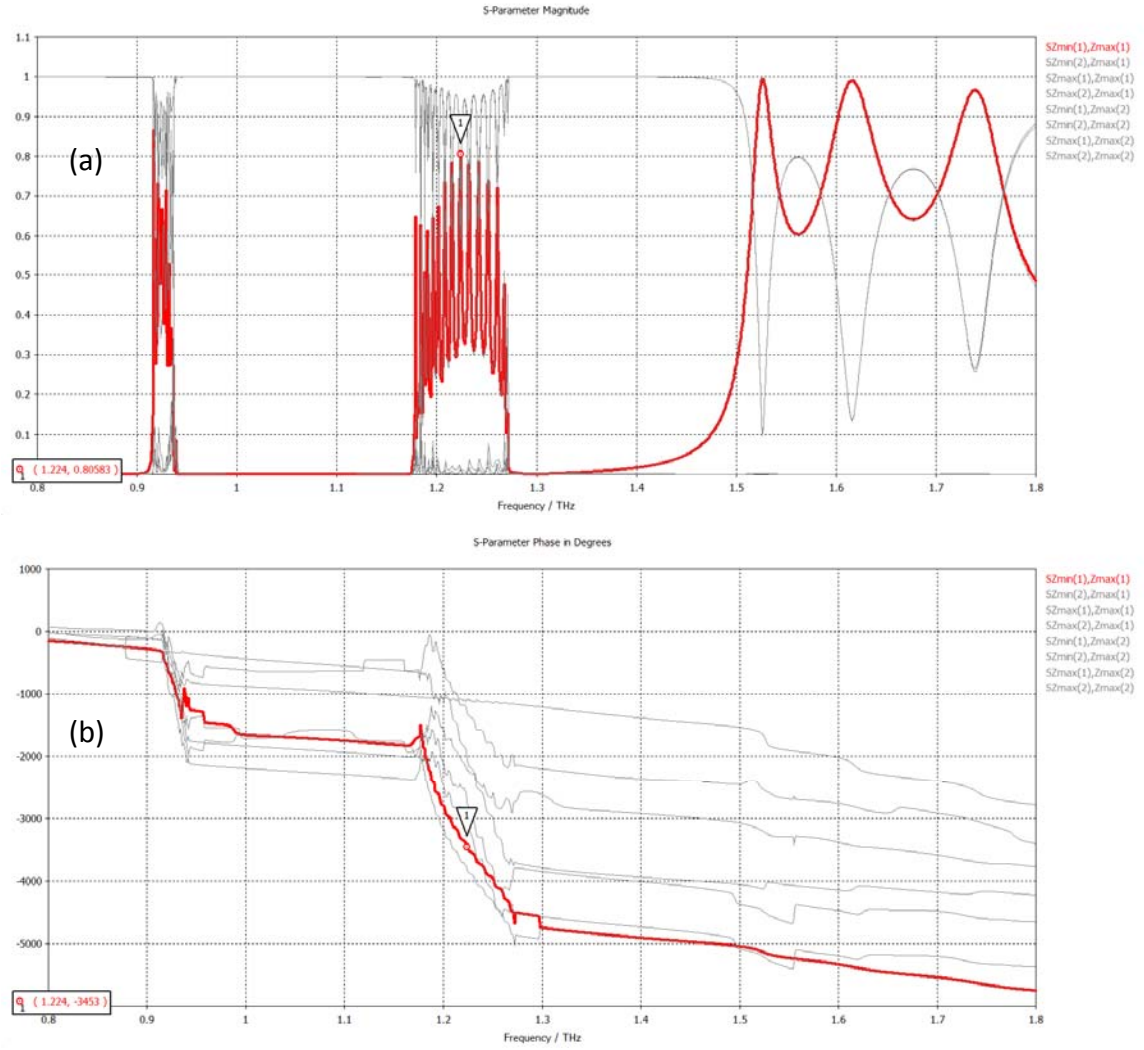

Figure 4.10. The magnitudes (a) and phases (b) of S-parameters of a 20-layered dotnet MM slab comprised of the unit cell shown in Figure 4.2(c)

Table 4.1 The E-field plots of 20-layered MM at different resonances.

Resonant Frequency (THz)	E-Field Plots	Resonant Frequency (THz)	E-Field Plots
1.271	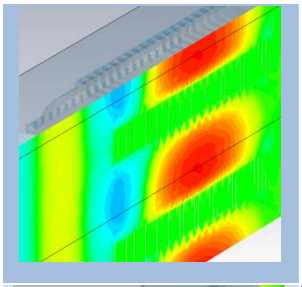	1.208	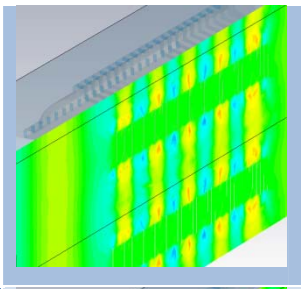
1.268	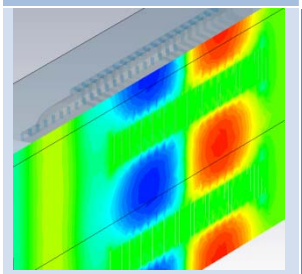	1.202	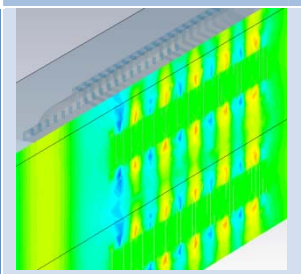
1.261	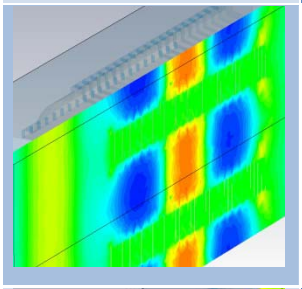	1.196	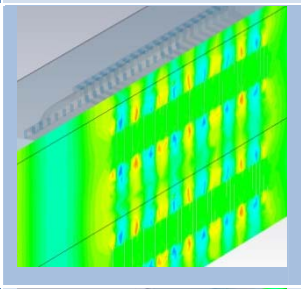
1.252	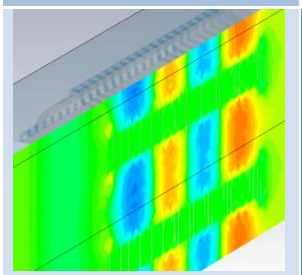	1.191	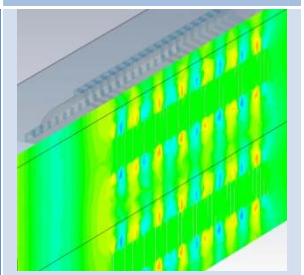
1.242	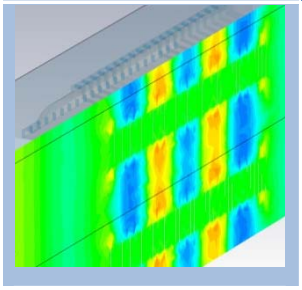	1.188	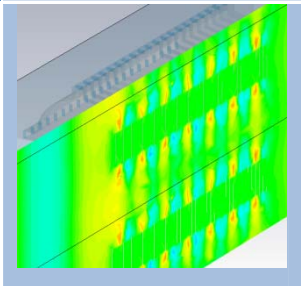

1.232	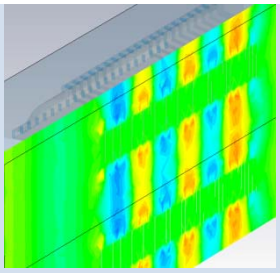	1.184	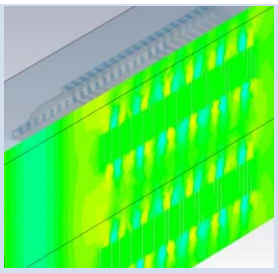
1.224	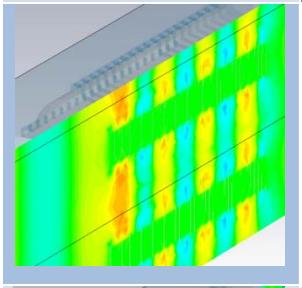	1.179	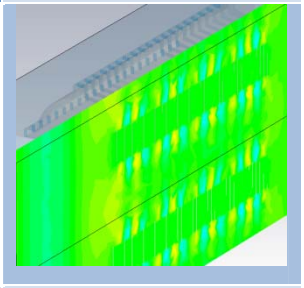
1.215	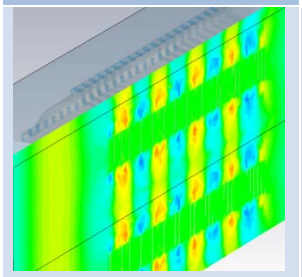		

Chapter 5. CONCLUSIONS AND FUTURE WORK

5.1 CONCLUSIONS

Current THz range optical components typically perform EM beam steering in free space, leading to large, diffraction-limited components. This paper introduces a novel, metamaterials-based approach to THz beam steering that vastly reduces component size and surpasses the Abbe Diffraction limit. After providing the background, motivation, and related research in chapter 1, chapter 2 introduces improved robust methods to fully retrieve effective material properties and constitutive parameters of metamaterials at all frequencies of interest, even in strongly anti-resonant zones. The major improvement of the proposed full retrieval methods provide is the retrieval of the negative imaginary components of refractive index. In addition, several patch algorithms for fixing discontinuities in the retrieved refractive indices of strongly-coupled multilayered metamaterials are proposed. These algorithms correct for the effects of induced extra resonant modes, improving the accuracy of the constitutive parameter full retrieval methods.

Several different tuning mechanisms for active metamaterials (AMM) were investigated in Chapter 3, including changing the gap widths of metallic conductors, in-plane rotation of the metallic pattern, mechanically shifting the entire MM layer in the direction of wave propagation, and electrically tuning the dielectric properties by applying DC biasing voltages, varying external magnetic fields, or changing the temperature. If a tunable MM is designed to be tuned electrically and mechanically, the tuning range can be increased while retaining the possibility of fine tuning. In chapter 4, two novel approaches to manipulate EM waves in sub-wavelength dimensions were proposed, simulated and discussed.

To sum up, improved retrieval methods along with three different patch algorithms for extracting continuous material properties and constitutive parameters in single and multilayered metamaterials were proposed in this thesis and successfully performed. Furthermore, a new kind of flexible, tunable active metamaterial was invented with the unique capability to change the material properties of each individual unit cell of a MM slab. Based on the proposed tunable active metamaterials, multifunctional and reconfigurable devices, such as a pattern-less waveguide and a multifunctional flat lens optical bench, have been designed and simulated.

5.2 FUTURE WORK

5.2.1 *Improvements of Retrieval Methods*

The retrieved effective material properties and constitutive parameters by the proposed methods in Chapter 2 are based on implicit assumptions of metamaterial homogenization and effective media theory inspired by natural material Drude/Lorentz models. Thus, only the effective scalar material properties and constitutive parameters are retrieved. For the future, the proposed methods should be extended to retrieve the tensor form of material properties and constitutive parameters, as shown in (5.1).

$$\varepsilon_{eff} = \begin{bmatrix} \varepsilon_{xx} & \varepsilon_{xy} & \varepsilon_{xz} \\ \varepsilon_{yx} & \varepsilon_{yy} & \varepsilon_{yz} \\ \varepsilon_{zx} & \varepsilon_{zy} & \varepsilon_{zz} \end{bmatrix}$$
$$\mu_{eff} = \begin{bmatrix} \mu_{xx} & \mu_{xy} & \mu_{xz} \\ \mu_{yx} & \mu_{yy} & \mu_{yz} \\ \mu_{zx} & \mu_{zy} & \mu_{zz} \end{bmatrix}. \tag{5.1}$$

Furthermore, with the consideration of the magneto-electric coupling effect [88] in bi-isotropic media in (5.2), the elements in the tensor form of constitutive parameters may be retrieved with all positive imaginary parts of values that strictly follow the physical rules. It is worth noting that the magneto-electric coupling effect in bi-isotropic media is caused by the chirality κ and Tellegen/reciprocity χ , and κ and χ are also in tensor forms.

$$D = \varepsilon E + \xi H = \varepsilon E + (\chi - i\kappa)\sqrt{\varepsilon\mu}H$$
$$B = \mu H + \zeta E = \mu H + (\chi + i\kappa)\sqrt{\varepsilon\mu}H \ . \quad (5.2)$$

5.2.2 *Fabrication Considerations*

First, the material properties of the raw materials adopted in the metamaterial and device designs have to be determined in the THz band. For example, the material properties of PDLC have not yet been reported for the THz range. Obtaining those material properties will require the transmission and reflection coefficients of PDLC slab measured from THz time domain spectroscopy (TDS), which will be provided by the Hong Kong City U. research group.

After the characterization of the necessary material properties of raw materials adopted in the designs, simulations of the proposed devices based on the exact material properties can be finalized for the implementations of the proposed devices.

As PDLC is a polymer-based material embedded with dispersive liquid crystal droplets, the fabrication process can dramatically affect the final refractive index. Studies on the parameters of fabrication processes, such as the exposure time for the UV curing process, the intensity of UV light, and the incident direction of UV light, must be investigated.

The deposition of noble metals on a freestanding structure such as PDLC is another important issue to investigate. The top-down approach for metamaterial fabrication has to be studied and performed using MEMS and/or nanofabrication procedures, such as focused ion beam lithography, E-beam lithography, soft lithography, etc.

Finally, a study on overcoming the challenges of making multilayered metamaterial structures must be conducted, with attention given to the lead wire layout and electrodes necessary for pixel-by-pixel control of EM waves in active tunable metamaterials.

BIBLIOGRAPHY

[1] P. W. Gwyn, "Filling the THz gap—high power sources and applications," *Reports on Progress in Physics,* vol. 69, p. 301, 2006.

[2] H. Quast and T. Loffler, "3D-terahertz-tomography for material inspection and security," in *Infrared, Millimeter, and Terahertz Waves, 2009. IRMMW-THz 2009. 34th International Conference on*, 2009, pp. 1-2.

[3] R. M. Woodward, V. P. Wallace, D. D. Arnone, E. H. Linfield, and M. Pepper, "Terahertz Pulsed Imaging of Skin Cancer in the Time and Frequency Domain," *Journal of Biological Physics,* vol. 29, pp. 257-259, 2003.

[4] B. S. Williams, "Terahertz quantum-cascade lasers," *Nat Photon,* vol. 1, pp. 517-525, 2007.

[5] M. Usami and et al., "Development of a THz spectroscopic imaging system," *Physics in Medicine and Biology,* vol. 47, p. 3749, 2002.

[6] P. H. Siegel, "Terahertz Technology in Biology and Medicine," *IEEE Transactions on Microwave Theory and Techniques,* vol. 52, p. 2438, 2004.

[7] K. Kawase, Y. Ogawa, Y. Watanabe, and H. Inoue, "Non-destructive terahertz imaging of illicit drugs using spectral fingerprints," *Opt. Express,* vol. 11, pp. 2549-2554, 2003.

[8] L. Ho, M. Pepper, and P. Taday, "Terahertz spectroscopy: Signatures and fingerprints," *Nat Photon,* vol. 2, pp. 541-543, 2008.

[9] A. J. Fitzgerald and et al., "An introduction to medical imaging with coherent terahertz frequency radiation," *Physics in Medicine and Biology,* vol. 47, p. R67, 2002.

[10] R. Wilk, I. Pupeza, R. Cernat, and M. Koch, "Highly Accurate THz Time-Domain Spectroscopy of Multilayer Structures," *Selected Topics in Quantum Electronics, IEEE Journal of,* vol. 14, pp. 392-398, 2008.

[11] N. Vieweg, C. Jansen, M. K. Shakfa, M. Scheller, N. Krumbholz, R. Wilk, M. Mikulics, and M. Koch, "Molecular properties of liquid crystals in the terahertz frequency range," *Opt. Express,* vol. 18, pp. 6097-6107, 2010.

[12] T.-R. Tsai, C.-Y. Chen, C.-L. Pan, R.-P. Pan, and X.-C. Zhang, "Terahertz time-domain spectroscopy studies of theoretical constants of the nematic liquid crystal 5CB," *Appl. Opt,* vol. 42, pp. 2372–2375, 2003.

[13] T. Loffler and et al., "Visualization and classification in biomedical terahertz pulsed imaging," *Physics in Medicine and Biology,* vol. 47, p. 3847, 2002.

[14] X. C. Zhang, "Terahertz wave imaging: horizons and hurdles," *Physics in Medicine and Biology,* vol. 47, pp. 3667-3677, 2002.

[15] R. Piesiewicz, C. Jansen, D. Mittleman, T. Kleine-Ostmann, M. Koch, and T. Kurner, "Scattering Analysis for the Modeling of THz Communication Systems," *Antennas and Propagation, IEEE Transactions on,* vol. 55, pp. 3002-3009, 2007.

[16] R. Klaus, "Table-top sources of ultrashort THz pulses," *Reports on Progress in Physics,* vol. 70, p. 1597, 2007.

[17] G. Wuestefeld, J. Feikes, M. von Hartrott, M. Ries, P. Schmid, A. Hoehl, R. Klein, R. Mueller, and G. Ulm, "Metrology Light Source: The first electron storage ring optimized

for generating coherent THz radiation," *Physical Review Special Topics-Accelerators and Beams,* vol. 14, p. 030705, Mar 22 2011.

[18] N. Oda, M. Sano, H. Yoneyama, T. Sasaki, S. Kurashina, I. Hosako, N. Sekine, K. Fukunaga, Y. Ogawa, S. Komatsubara, T. Sudoh, T. Irie, H. Atake, and Y. Ikeda, "Development of bolometer-type uncooled THz-QVGA sensor and camera," in *Infrared, Millimeter, and Terahertz Waves, 2009. IRMMW-THz 2009. 34th International Conference on*, 2009, pp. 1-2.

[19] R. A. Shelby, D. R. Smith, and S. Schultz, "Experimental Verification of a Negative Index of Refraction," *Science,* vol. 292, pp. 77-79, April 6, 2001.

[20] D. R. Smith, W. J. Padilla, D. C. Vier, S. C. Nemat-Nasser, and S. Schultz, "Composite Medium with Simultaneously Negative Permeability and Permittivity," *Physical Review Letters,* vol. 84, pp. 4184-4187, 2000.

[21] V. G. Veselago, "THE ELECTRODYNAMICS OF SUBSTANCES WITH SIMULTANEOUSLY NEGATIVE VALUES OF epsilon AND mu," *SOVIET PHYSICS USPEKHI,* vol. 92, pp. 517-526, 1967.

[22] S. A. Ramakrishna and T. M. Grzegorczyk, *Physics and applications of negative refractive index materials*. Bellingham, Wash.; Boca Raton; London: SPIE Press ; CRC Press, 2009.

[23] J. B. Pendry, A. J. Holden, W. J. Stewart, and I. Youngs, "Extremely Low Frequency Plasmons in Metallic Mesostructures," *Physical Review Letters,* vol. 76, pp. 4773-4776, 1996.

[24] J. B. Pendry and A. J. Holden, "Magnetism from conductors and enhanced nonlinear phenomena," *IEEE Transactions on Microwave Theory & Techniques,* vol. 47, 1999.

[25] S. Linden, C. Enkrich, M. Wegener, J. Zhou, T. Koschny, and C. M. Soukoulis, "Magnetic Response of Metamaterials at 100 Terahertz," *Science,* vol. 306, pp. 1351-1353, November 19, 2004 2004.

[26] L. Sungjoon, C. Caloz, and T. Itoh, "Metamaterial-based electronically controlled transmission-line structure as a novel leaky-wave antenna with tunable radiation angle and beamwidth," *Microwave Theory and Techniques, IEEE Transactions on,* vol. 52, pp. 2678-2690, 2004.

[27] R. W. Ziolkowski and A. Erentok, "Metamaterial-based efficient electrically small antennas," *Antennas and Propagation, IEEE Transactions on,* vol. 54, pp. 2113-2130, 2006.

[28] F. Qureshi, M. A. Antoniades, and G. V. Eleftheriades, "A compact and low-profile metamaterial ring antenna with vertical polarization," *Antennas and Wireless Propagation Letters, IEEE,* vol. 4, pp. 333-336, 2005.

[29] D. R. Smith, J. B. Pendry, and M. C. K. Wiltshire, "Metamaterials and Negative Refractive Index," *Science,* vol. 305, pp. 788-792, August 6, 2004 2004.

[30] R. Islam and G. V. Eleftheriades, "Phase-agile branch-line couplers using metamaterial lines," *Microwave and Wireless Components Letters, IEEE,* vol. 14, pp. 340-342, 2004.

[31] R. Islam, F. Elek, and G. V. Eleftheriades, "Coupled-line metamaterial coupler having co-directional phase but contra-directional power flow," *Electronics Letters,* vol. 40, pp. 315-317, 2004.

[32] M. A. Antoniades and G. V. Eleftheriades, "A broadband Wilkinson balun using microstrip metamaterial lines," *Antennas and Wireless Propagation Letters, IEEE,* vol. 4, pp. 209-212, 2005.

[33] T. Chao-Hsiung and C. Chih-Lin, "A Broadband Quadrature Power Splitter Using Metamaterial Transmission Line," *Microwave and Wireless Components Letters, IEEE,* vol. 18, pp. 25-27, 2008.

[34] J. McVay, N. Engheta, and A. Hoorfar, "High impedance metamaterial surfaces using Hilbert-curve inclusions," *Microwave and Wireless Components Letters, IEEE,* vol. 14, pp. 130-132, 2004.

[35] L. Lei, C. Caloz, and T. Itoh, "Dominant mode leaky-wave antenna with backfire-to-endfire scanning capability," *Electronics Letters,* vol. 38, pp. 1414-1416, 2002.

[36] A. Lai, T. Itoh, and C. Caloz, "Composite right/left-handed transmission line metamaterials," *Microwave Magazine, IEEE,* vol. 5, pp. 34-50, 2004.

[37] A. Grbic and G. V. Eleftheriades, "Subwavelength focusing using a negative-refractive-index transmission line lens," *Antennas and Wireless Propagation Letters, IEEE,* vol. 2, pp. 186-189, 2003.

[38] J. B. Pendry, "Negative Refraction Makes a Perfect Lens," *Physical Review Letters,* vol. 85, pp. 3966-3969, 2000.

[39] N. Fang, H. Lee, C. Sun, and X. Zhang, "Sub-Diffraction-Limited Optical Imaging with a Silver Superlens," *Science,* vol. 308, 2005.

[40] J. Valentine, J. Li, T. Zentgraf, G. Bartal, and X. Zhang, "An optical cloak made of dielectrics," *Nature materials,* vol. 8, pp. 568-71, 2009.

[41] K. S. Packard, "The Origin of Waveguides: A Case of Multiple Rediscovery," *Microwave Theory and Techniques, IEEE Transactions on,* vol. 32, pp. 961-969, 1984.

[42] R. M. Barrett, "Microwave Printed Circuits - A Historical Survey," *Microwave Theory and Techniques, IRE Transactions on,* vol. 3, pp. 1-9, 1955.

[43] D. M. Pozar, *Microwave engineering*. Hoboken, NJ: J. Wiley, 2005.

[44] M. Nagel, A. Marchewka, and H. Kurz, "Low-index discontinuity terahertz waveguides," *Opt. Express,* vol. 14, pp. 9944-9954, 2006.

[45] R. Nagarajan, S. Levy, and J. E. Bowers, "Millimeter wave narrowband optical fiber links using external cavity semiconductor lasers," *Lightwave Technology, Journal of,* vol. 12, pp. 127-136, 1994.

[46] D. Chen and H. Chen, "A novel low-loss Terahertz waveguide: Polymer tube," *Opt. Express,* vol. 18, pp. 3762-3767, 2010.

[47] S. H. Nam, A. J. Taylor, and A. Efimov, "Subwavelength hybrid terahertz waveguides," *Opt. Express,* vol. 17, pp. 22890-22897, 2009.

[48] L. Sz-Chin Steven, K. Brian, and H. Yiping, "Tunable two-dimensional liquid gradient refractive index (L-GRIN) lens for variable light focusing," *Lab on a Chip - Miniaturisation for Chemistry & Biology,* vol. 10, 2010.

[49] T. C. Kraan, T. van Bommel, and R. A. M. Hikmet, "Modeling liquid-crystal gradient-index lenses," *J. Opt. Soc. Am. A,* vol. 24, pp. 3467-3477, 2007.

[50] Y. G. Marinov, G. B. Hadjichristov, and A. G. Petrov, "Gradient microscale PDLC single layers for light control," *J. Optoelectron. Adv. Mat. Journal of Optoelectronics and Advanced Materials,* vol. 11, pp. 1186-1189, 2009.

[51] Y. G. Marinov, G. B. Hadjichristov, and A. G. Petrov, "Single-layered PDLC films for electrically variable laser light reflection application," *Optics and Lasers in Engineering,* vol. 48, pp. 1161-1165, 2010.

[52] X. Chen, T. M. Grzegorczyk, B.-I. Wu, J. Pacheco, and J. A. Kong, "Robust method to retrieve the constitutive effective parameters of metamaterials," *Physical Review E,* vol. 70, p. 016608, 2004.

[53] T. M. G. X. Chen, and J. A. Kong, "Optimization approach to the retrieval of the constitutive parameters of slab of general bianisotropic medium," *Progress in Electromagnetics Research-PIER,* vol. 60, 2006.

[54] D. R. Smith, S. Schultz, P. Markoš, and C. M. Soukoulis, "Determination of effective permittivity and permeability of metamaterials from reflection and transmission coefficients," *Physical Review B,* vol. 65, p. 195104, 2002.

[55] J. B. Pendry, "Negative Refraction Makes a Perfect Lens," *Physical Review Letters,* vol. 85, p. 3966, 2000.

[56] H. Y. Chen, X. Y. Hou, and L. J. Deng, "A Novel Microwave Absorbing Structure Using FSS Metamaterial," in *Progress In Electromagnetics Research Symposium Proceedings*, Moscow, Russia, 2009, p. 1195.

[57] M. C. K. Wiltshire, "Bending Light the Wrong Way," *Science,* vol. 292, pp. 60-61, April 6, 2001.

[58] R. W. Ziolkowski, "Design, fabrication, and testing of double negative metamaterials," *Antennas and Propagation, IEEE Transactions on,* vol. 51, pp. 1516-1529, 2003.

[59] R. W. Ziolkowski and N. Engheta, "Metamaterial special issue introduction," *Antennas and Propagation, IEEE Transactions on,* vol. 51, pp. 2546-2549, 2003.

[60] A. M. Nicolson and G. F. Ross, "Measurement of the Intrinsic Properties of Materials by Time-Domain Techniques," *Instrumentation and Measurement, IEEE Transactions on,* vol. 19, pp. 377-382, 1970.

[61] P. Markos and C. Soukoulis, "Transmission properties and effective electromagnetic parameters of double negative metamaterials," *Opt. Express,* vol. 11, pp. 649-661, 2003.

[62] M. W. Born, E., "Principles of optics: electromagnetic theory of propagation, interference and diffraction of light," 1964.

[63] D. A. Frickey, "Conversions between S, Z, Y, H, ABCD, and T parameters which are valid for complex source and load impedances," *Microwave Theory and Techniques, IEEE Transactions on,* vol. 42, pp. 205-211, 1994.

[64] R. B. Marks, D. F. Williams, and D. A. Frickey, "Comments on "Conversions between S, Z, Y, h, ABCD, and T parameters which are valid for complex source and load impedances" [and reply]," *Microwave Theory and Techniques, IEEE Transactions on,* vol. 43, pp. 914-915, 1995.

[65] T. Koschny, P. Markoscaron, D. R. Smith, and C. M. Soukoulis, "Resonant and antiresonant frequency dependence of the effective parameters of metamaterials," *Physical Review E,* vol. 68, p. 065602, 2003.

[66] P. A. Belov, S. A. Tretyakov, and A. J. Viitanen, "Nonreciprocal microwave band-gap structures," *Physical Review E,* vol. 66, p. 016608, 2002.

[67] C. R. Simovski, P. A. Belov, and H. Sailing, "Backward wave region and negative material parameters of a structure formed by lattices of wires and split-ring resonators," *Antennas and Propagation, IEEE Transactions on,* vol. 51, pp. 2582-2591, 2003.

[68] R. Storn and K. Price, "Differential Evolution A Simple and Efficient Heuristic for Global Optimization over Continuous Spaces," *J. of Global Optimization,* vol. 11, pp. 341-359, 1997.

[69] N. Liu, L. Fu, S. Kaiser, H. Schweizer, and H. Giessen, "Plasmonic Building Blocks for Magnetic Molecules in Three-Dimensional Optical Metamaterials," *Advanced Materials,* vol. 20, pp. 3859-3865, 2008.

[70] R. F. Hoskins, *Generalised functions*. Chichester; New York [etc.]: Ellis Horwood Limited ; John Wiley & Sons, 1979.

[71] S. Zhang, W. Fan, K. J. Malloy, S. R. Brueck, N. C. Panoiu, and R. M. Osgood, "Near-infrared double negative metamaterials," *Opt. Express,* vol. 13, pp. 4922-4930, 2005.

[72] J. Valentine, Z. Shuang, T. Zentgraf, and Z. Xiang, "Development of Bulk Optical Negative Index Fishnet Metamaterials: Achieving a Low-Loss and Broadband Response Through Coupling," *Proceedings of the IEEE,* vol. 99, pp. 1682-1690, 2011.

[73] M. Lapine, D. Powell, M. Gorkunov, I. Shadrivov, R. Marques, and Y. Kivshar, "Structural tunability in metamaterials," *Applied Physics Letters,* vol. 95, pp. 084105-3, 2009.

[74] E. Ekmekci, A. C. Strikwerda, K. Fan, G. Keiser, X. Zhang, G. Turhan-Sayan, and R. D. Averitt, "Frequency tunable terahertz metamaterials using broadside coupled split-ring resonators," *Physical Review B,* vol. 83, p. 193103, 2011.

[75] H. Tao, A. Strikwerda, K. Fan, W. Padilla, X. Zhang, and R. Averitt, "MEMS Based Structurally Tunable Metamaterials at Terahertz Frequencies," *Journal of Infrared, Millimeter and Terahertz Waves,* vol. 32, pp. 580-595, 2011.

[76] D. H. Werner, D.-H. Kwon, I.-C. Khoo, A. V. Kildishev, and V. M. Shalaev, "Liquid crystal clad near-infrared metamaterials with tunable negative-zero-positive refractive indices," *Opt. Express,* vol. 15, pp. 3342-3347, 2007.

[77] A. Minovich, D. N. Neshev, D. A. Powell, I. V. Shadrivov, and Y. S. Kivshar, "Tunable fishnet metamaterials infiltrated by liquid crystals," *Applied Physics Letters,* vol. 96, pp. 193103-3, 2010.

[78] F. Zhang, W. Zhang, Q. Zhao, J. Sun, K. Qiu, J. Zhou, and D. Lippens, "Electrically controllable fishnet metamaterial based on nematic liquid crystal," *Opt. Express,* vol. 19, pp. 1563-1568, 2011.

[79] Q. Zhao, L. Kang, B. Du, B. Li, J. Zhou, H. Tang, X. Liang, and B. Zhang, "Electrically tunable negative permeability metamaterials based on nematic liquid crystals," *Applied Physics Letters,* vol. 90, pp. 011112-3, 2007.

[80] I. Gil, J. Bonache, J. Garcia-Garcia, and F. Martin, "Tunable metamaterial transmission lines based on varactor-loaded split-ring resonators," *Microwave Theory and Techniques, IEEE Transactions on,* vol. 54, pp. 2665-2674, 2006.

[81] A. Velez, J. Bonache, and F. Martin, "Varactor-Loaded Complementary Split Ring Resonators (VLCSRR) and Their Application to Tunable Metamaterial Transmission Lines," *Microwave and Wireless Components Letters, IEEE,* vol. 18, pp. 28-30, 2008.

[82] F. Zhang, Q. Zhao, L. Kang, D. P. Gaillot, X. Zhao, J. Zhou, and D. Lippens, "Magnetic control of negative permeability metamaterials based on liquid crystals," *Applied Physics Letters,* vol. 92, pp. 193104-3, 2008.

[83] F. Zhang, L. Kang, Q. Zhao, J. Zhou, X. Zhao, and D. Lippens, "Magnetically tunable left handed metamaterials by liquid crystal orientation," *Opt. Express,* vol. 17, pp. 4360-4366, 2009.

[84] S. M. Mansfield and G. S. Kino, "Solid immersion microscope," *Applied Physics Letters,* vol. 57, pp. 2615-2616, 1990.

[85] B. D. Terris, H. J. Mamin, D. Rugar, W. R. Studenmund, and G. S. Kino, "Near-field optical data storage using a solid immersion lens," *Applied Physics Letters,* vol. 65, pp. 388-390, 1994.

[86] Q. Wu, G. D. Feke, R. D. Grober, and L. P. Ghislain, "Realization of numerical aperture 2.0 using a gallium phosphide solid immersion lens," *Applied Physics Letters,* vol. 75, pp. 4064-4066, 1999.

[87] H. Chen, C. T. Chan, and P. Sheng, "Transformation optics and metamaterials," *Nat Mater,* vol. 9, pp. 387-396, 2010.

[88] T. G. Mackay and A. Lakhtakia, *Electromagnetic anisotropy and bianisotropy : a field guide*. New Jersey, NJ [u.a.]: World Scientific, 2010.

APPENDIX

The following images demonstrate the possible 3D shapes of biasing voltages created by two voltage distribution functions, F(x) and F(y), of the top and bottom electrodes in the proposed tunable active metamaterials. The top electrodes are all connected in $\hat{y}$ direction and disconnected in $\hat{x}$ direction, while the bottom electrodes are all connected in $\hat{x}$ direction and disconnected in $\hat{y}$ direction.

1D Flat wedge surface (varying in X-axis): F(x) = 10, F(y) = 0

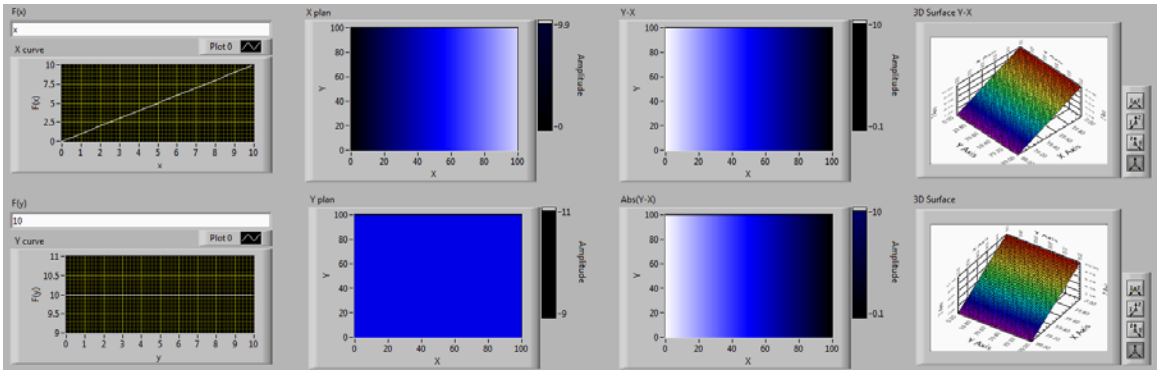

1D Flat wedge surface (varying in Y-axis): F(x) = 0, F(y) = -y

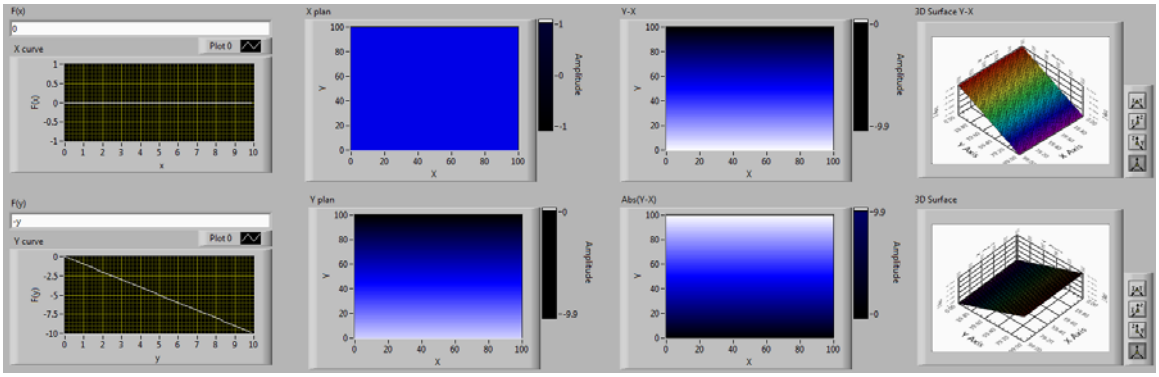

1D Flat wedge surface slope 45: F(x) = x-10, F(y) = y

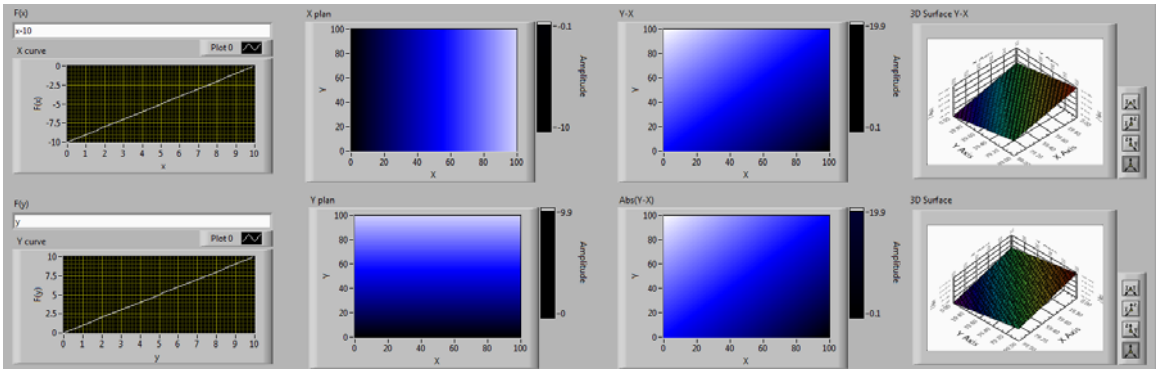

1D Beam Splitter (varying in X-axis): F(x) = 5-abs(x-5), F(y) = 0

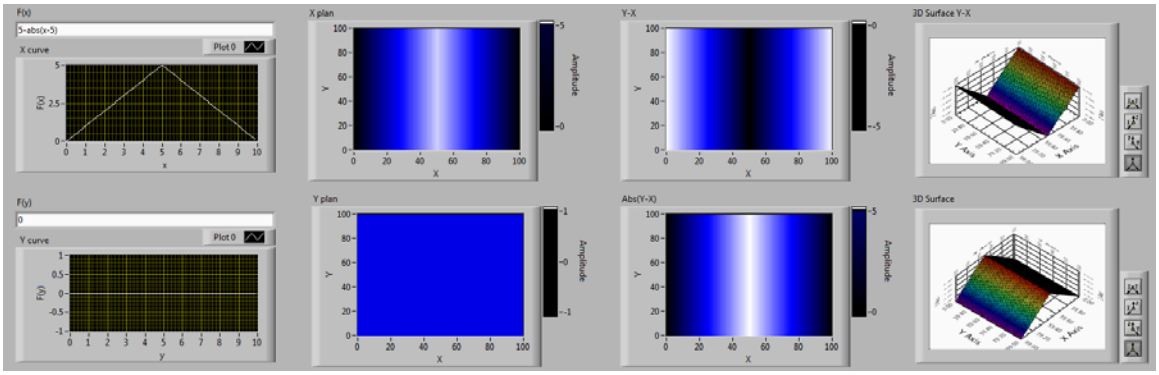

1D Beam Splitter (varying in Y-axis): F(x) = 0, F(y) = 5-abs(Y-5)

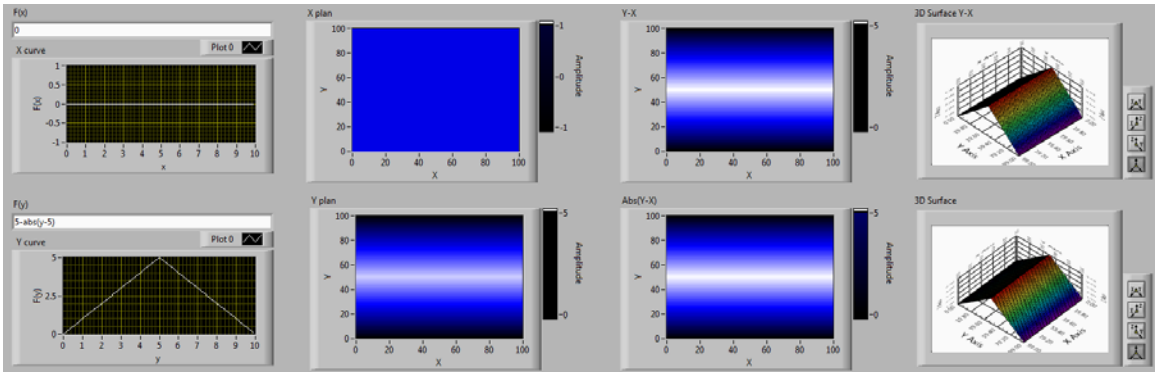

1D convex (varying in X-axis): F(x) = 10*cos(3.14*x/10+3.14/2), F(y) = 10

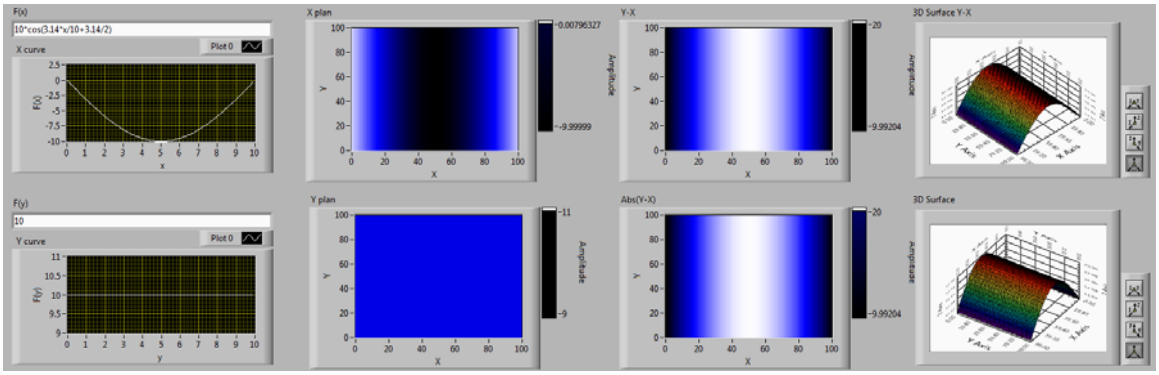

1D convex (varying in Y-axis): F(x) = 10, F(y) = 10*cos(3.14*y/10+3.14/2)

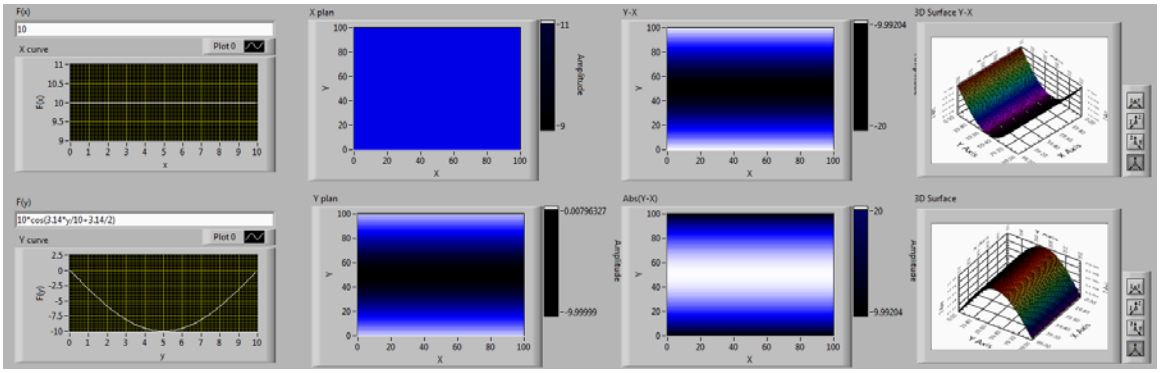

1D concave(varying in X-axis) : F(x) = 10*sin(3.14*x/10), F(y) = 10

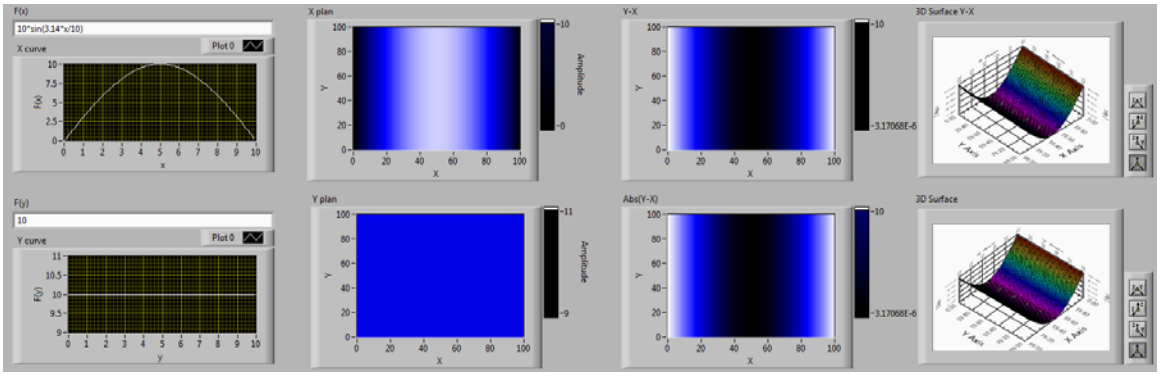

1D concave(varying in Y-axis) : F(x) = 0, F(y) = 10-10*sin(3.14*y/10)

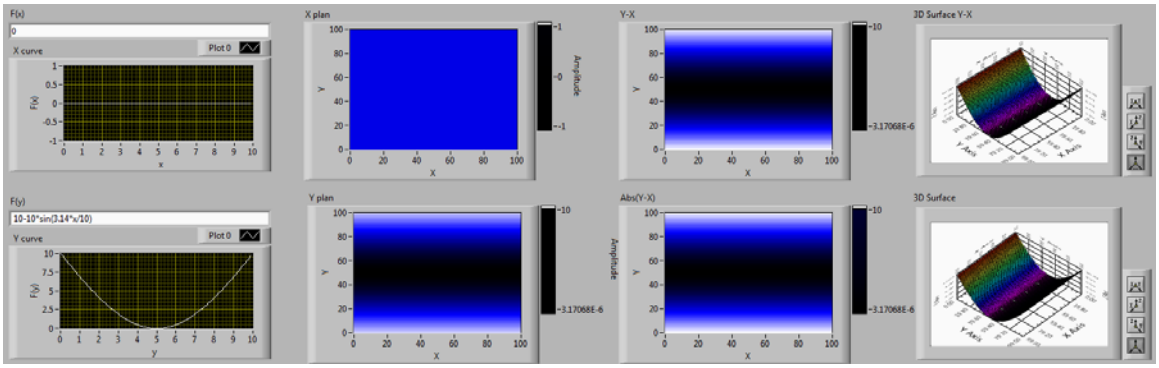

2D convex : F(x) = 10*sin(3.14*x/10), F(y) = 10*cos(3.14*y/10+3.14/2)

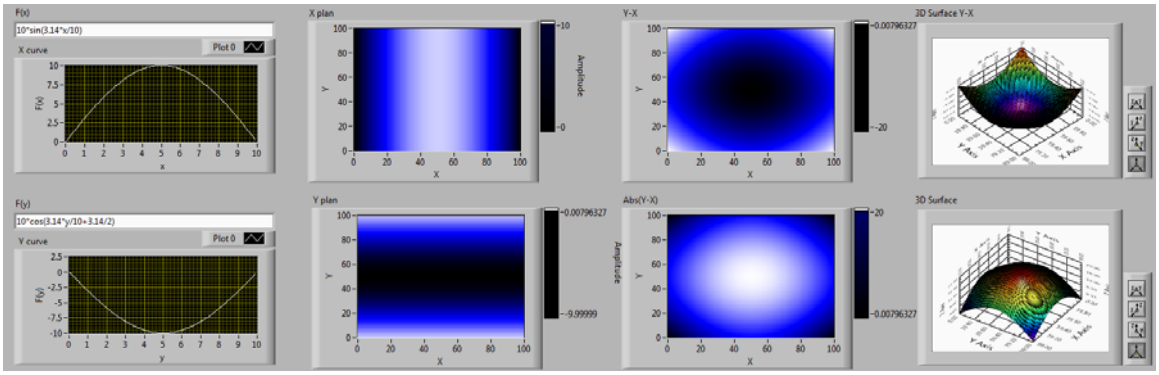

2D concave: F(x) = 10*sin(3.14*x/10)-10, F(y) = 10*cos(3.14*y/10+3.14/2)+10

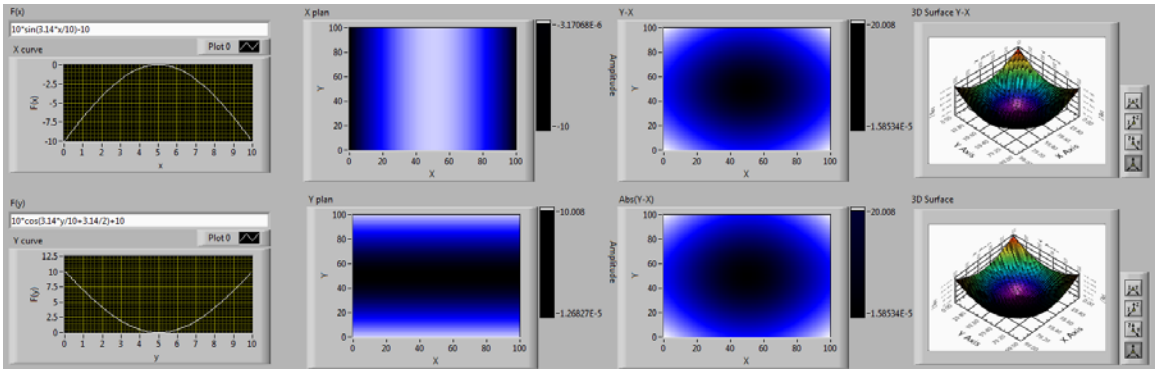

2D DarkCrossX: F(x) = 10*cos(3.14*y/10+3.14/2), F(y) = 10*cos(3.14*y/10+3.14/2)

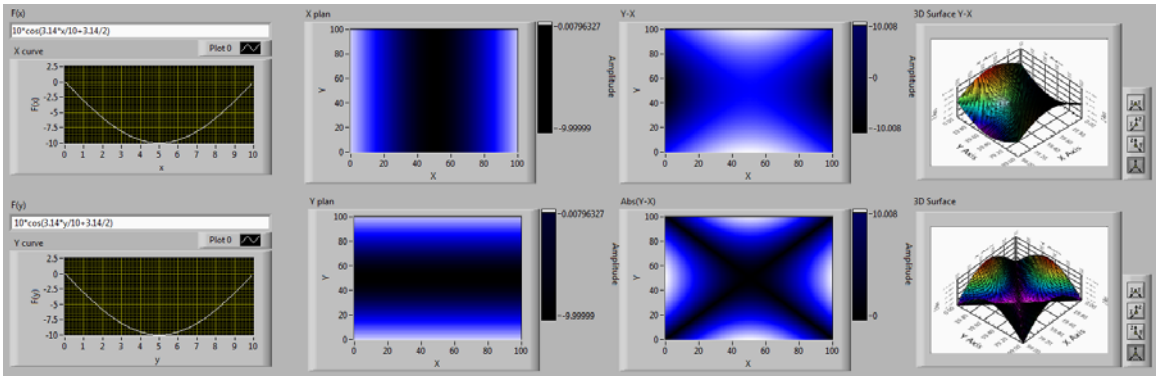

2D humps: F(x) = sin(3*x)+10*sin(1*x), F(y) = sin(3*y)+10*sin(1*y)

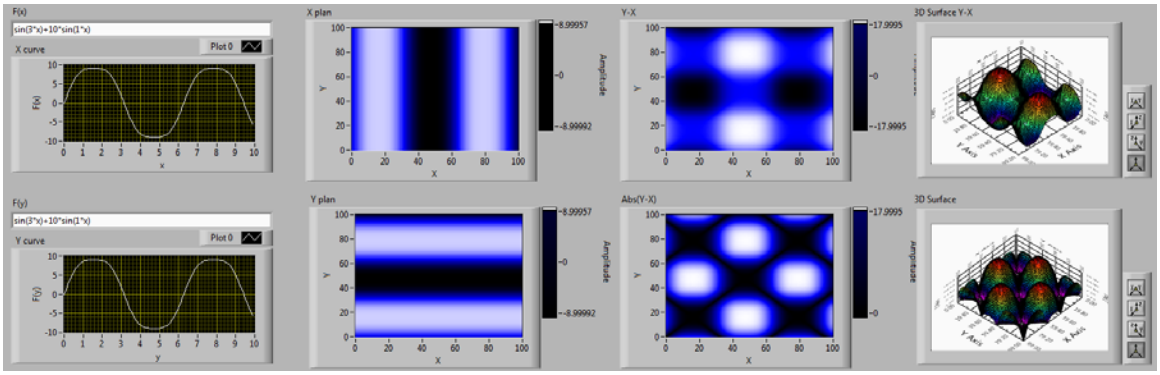

2D humps: F(x) = sin(2*x), F(y) = sin(2*y)

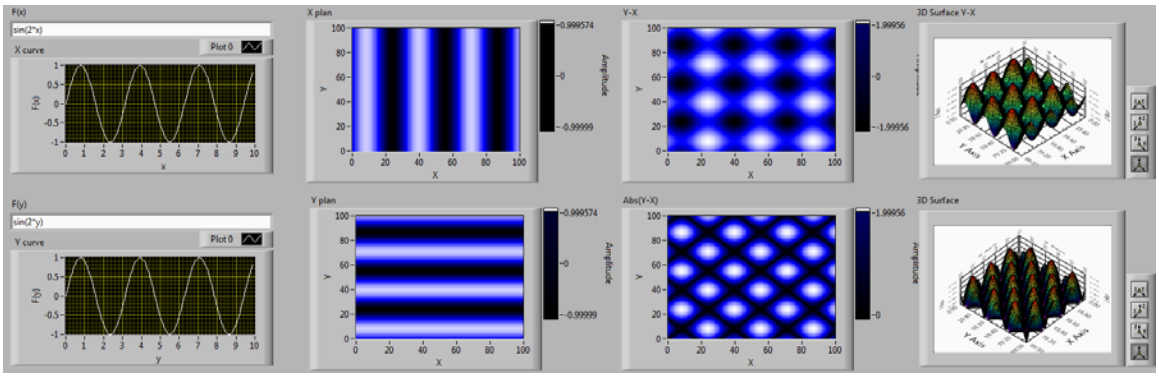

1D flatter sin: F(x) = sin(3*x/2)+10*sin(1*x/2) +10, F(y) = sin(3*y)+10*sin(y)

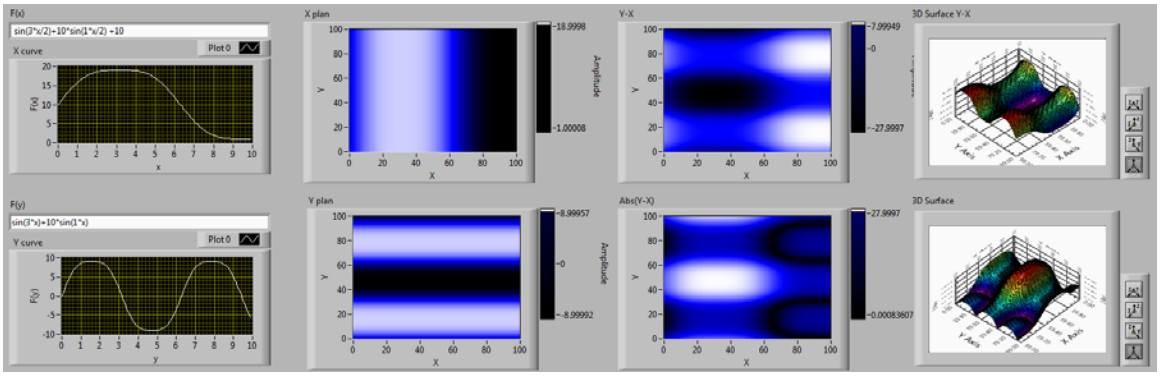

3D periodic ridges: F(x) = sin(3*x/2)+10*sin(1*x/2) +10, F(y) = sin(5*y)

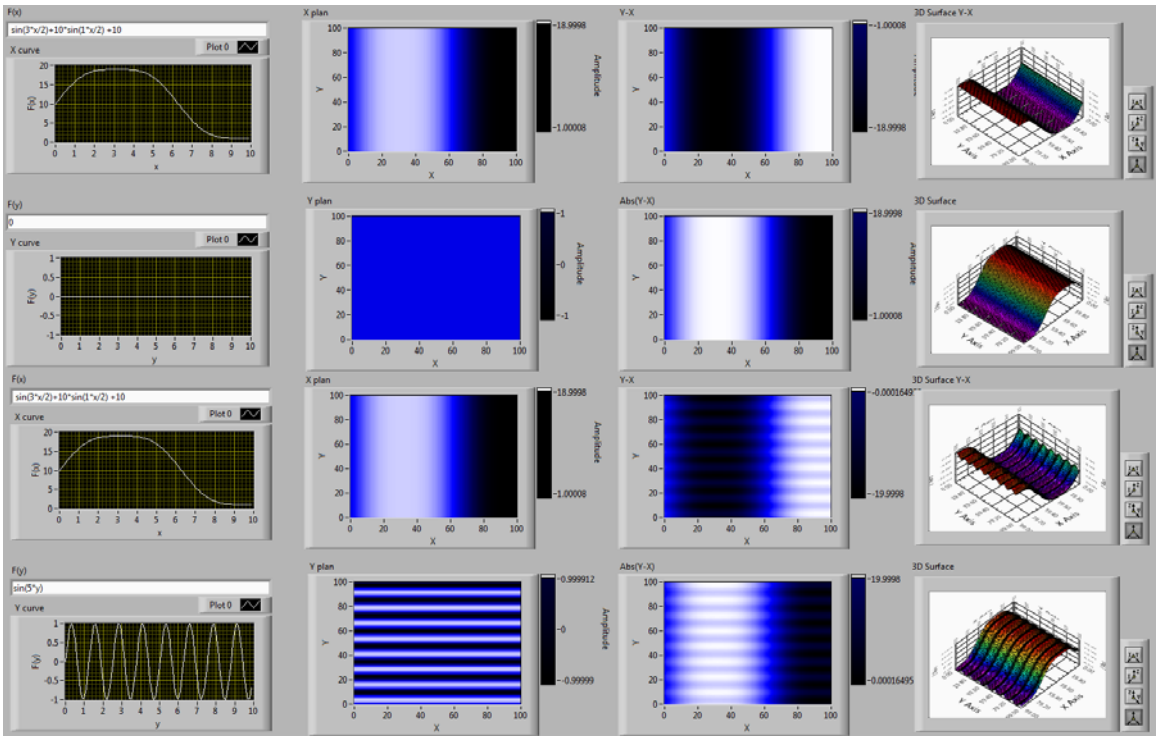

2D parabolic concave: F(x) = -(x-5)^2 , F(y) = (y-5)^2

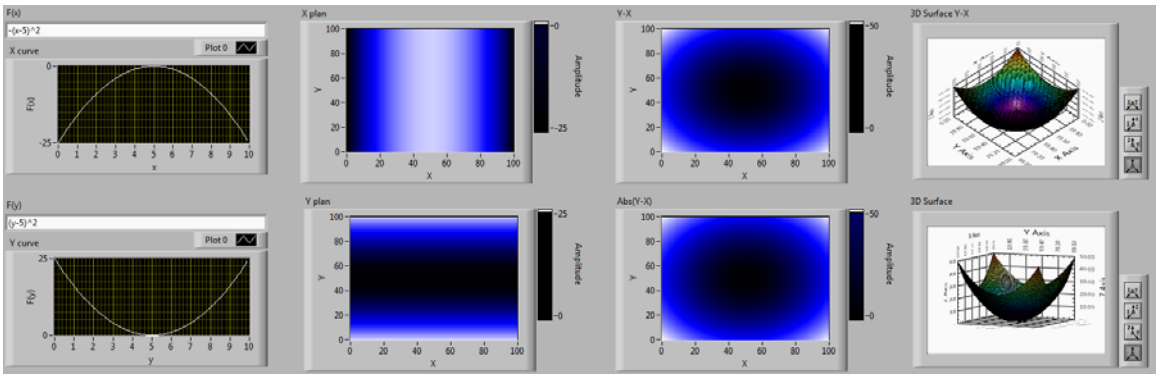

VITA

Feng-Ju Hsieh received a Bachelor of Science degree in Mechanical Engineering from the National Taiwan University (NTU), Taipei, Taiwan in 1998 and earned a Master of Science degree in Mechanical Engineering from the National Cheng Kung University (NCKU), Tainan, Taiwan in 2000.

After his graduate study in humanoid robot research, he joined the Industrial Technology Research Institute (ITRI) of Taiwan as a research associate and project manager involving in developing robotics, nondestructive testing (NDT) automation and ultrasonic biomedical devices from 2000 to 2006.

Later, he decided to go for higher degree in the United States, and he earned a Doctor of Philosophy degree from the University of Washington (UW), Seattle in Spring, 2012. In his graduate studies at UW, he broadened his research area to include robotics, medical devices, fiber optical sensors, optical coherence tomography, reconfigurable antennas, and applied electromagnetics. He also sharpened his teaching skills by serving as an instructor in ENGR100 class for two years, and a teaching assistant in many other classes.

His current research interests focus on polymer-based flexible metamaterials in terahertz frequencies by MEMS/Nano-fabrication technologies and relevant biomedical applications.

Mr. Hsieh is also a student member of the Society for Industrial and Applied Mathematics (SIAM) and the American Society of Mechanical Engineers (ASME). During his studies in Seattle, he has devoted himself to serving others and involve in many activities voluntarily as a board member of the NCKU Alumni Association in the Pacific Northwest.